論文 / 著書情報
Article / Book Information

題目(和文)	二種類の距離検知範囲および視野角を有する車載ミリ波レーダ用単一マイクロストリップアンテナ給電型レンズホーンアンテナの研究
Title(English)	A Study of Lens Horn Antenna Fed by Single Microstrip Antenna for Automotive Millimeter-wave Radar with Dual-Range Sensing and Dual Field-of-View
著者(和文)	栗山哲
Author(English)	Akira Kuriyama
出典(和文)	学位:博士(工学), 学位授与機関:東京工業大学, 報告番号:甲第11601号, 授与年月日:2020年9月25日, 学位の種別:課程博士, 審査員:廣川 二郎,阪口 啓,西方 敦博,青柳 貴洋,TRAN GIA KHANH
Citation(English)	Degree:Doctor (Engineering), Conferring organization: Tokyo Institute of Technology, Report number:甲第11601号, Conferred date:2020/9/25, Degree Type:Course doctor, Examiner:,,,,
学位種別(和文)	博士論文
Type(English)	Doctoral Thesis

Doctoral Dissertation

A Study of Lens Horn Antenna Fed by Single Microstrip Antenna for Automotive Millimeter-wave Radar with Dual-Range Sensing and Dual Field-of-View

August 2020

Presented by Akira Kuriyama
Supervised by Prof. Jiro Hirokawa

Department of Electrical and Electronic Engineering,
Tokyo Institute of Technology, Tokyo, Japan

Contents

Abbreviations

ABS:	Anti-lock Braking System
ADAS:	Advanced Driver Assistant System
AD:	Autonomous Driving
AEBS:	Automatic Emergency Braking System
ANT:	Antenna
CAN:	Controller Area Network
CMOS:	Complementary Metal Oxide Semiconductor
DBF:	Digital Beamforming
DDT:	Dynamic Driving Task
DeMOD:	De-modulator
DOA:	Direction of Arrival
EIRP:	Equivalent Isotropically Radiated Power
ESC:	Electronic Stability Control
EU:	European Union
FMCW:	Frequency Modulated Continuous Wave
FOV:	Field-of-View
HBT:	Hetero-junction Bipolar Transistor
HDPE:	High Density Polyethylene
HPBW:	Half Power Bandwidth
IF:	Intermediate Frequency
JP:	Japan
LiDAR:	Light Detection and Ranging
LRR:	Long-Range Radar
LTCC:	Low Temperature Co-fired Ceramics
MEMS:	Micro-Electro-Mechanical Systems
MRR:	Middle-Range Radar
MOD:	Modulator
MIMO:	Multi-Input Multi-Output
MMIC:	Monolithic Microwave Integrated Circuit
MSA:	Microstrip Antenna
MUSIC:	Multiple Signal Classification
NA:	North America
NCAP:	New Car Assessment Programme
NHTSA:	National Highway Traffic Safety Administration
OEDR:	Object and Event Detection and Response
ODD:	Operational Design Domain
PA:	Power Amplifier

PML:	Perfectly Matched Layer
PPS:	Poly-Phenylene Sulfide
PTFE:	Poly Tetra Fluoro Ethylene
RCS:	Radar Cross Section
RF:	Radio Frequency
Rx:	Receiver
SAE:	Society of Automotive Engineers
SDGs:	Sustainable Development Goals
SIP:	Cross-ministerial Strategic Innovation Promotion Program
SRR:	Short-Range Radar
TCXO:	Temperature-Compensated Crystal Oscillator
Tx:	Transmitter
UNECE:	United Nations Economic Commission for Europe
UWB:	Ultra Wide Band
VCO:	Voltage-Controlled Oscillator
WHO:	World Health Organization

Chapter 1

Objective and Background

1.1 Introduction

Advanced driver-assistance systems (ADAS) and autonomous driving [i] (AD) systems are promising technology of preventing traffic accidents, reducing the environmental load, and achieving a sustainable society. In Japan, sales of vehicles with ADAS such as collision mitigation functions have been launched since early 2000. Moreover, the installation of the automatic emergency braking system (AEBS) will be mandated for the new vehicles in Japan from 2021 [1.3], and it is presumed that the ADAS market will grow acceleratingly. Contrary to the ADAS, acceleration of research and development of technologies for the AD system has faded slightly because of accidents in experiments on public road and delay of development of the law. However, the AD system still attracts attention as a mobility technology in next generation. According to the above reasons, the market for the ADAS and AD systems has continued to grow.

Figure 1.1 shows a trend in the number of new vehicles produced in the world by 2030, and the production of vehicles equipped with the ADAS and AD systems [1.4]. The automotive market with the ADAS and AD systems is expected to drastically grow until 2020, and then gradually expand. In the market, a market of AD systems with level 3 or more is expected to start to rise from around 2025. As a result, it is predicted that approximately half of the new vehicles produced in one year will be equipped with the ADAS or AD systems after 2020.

In the background of this growth market, sensing technologies for the ADAS and AD systems have been actively investigated, because vehicles with the ADAS and

---

[i] In this dissertation, the term “autonomous” is used as a general expression because millimeter-wave radars which are targeted in this dissertation are necessary regardless of whether the vehicles are controlled by in-vehicle system or remote one. On the other hand, “automated” is used in explanations which require technically accurate expressions [1.1] such as a definition for levels of driving automation announced by SAE (Society of Automotive Engineers) [1.2].

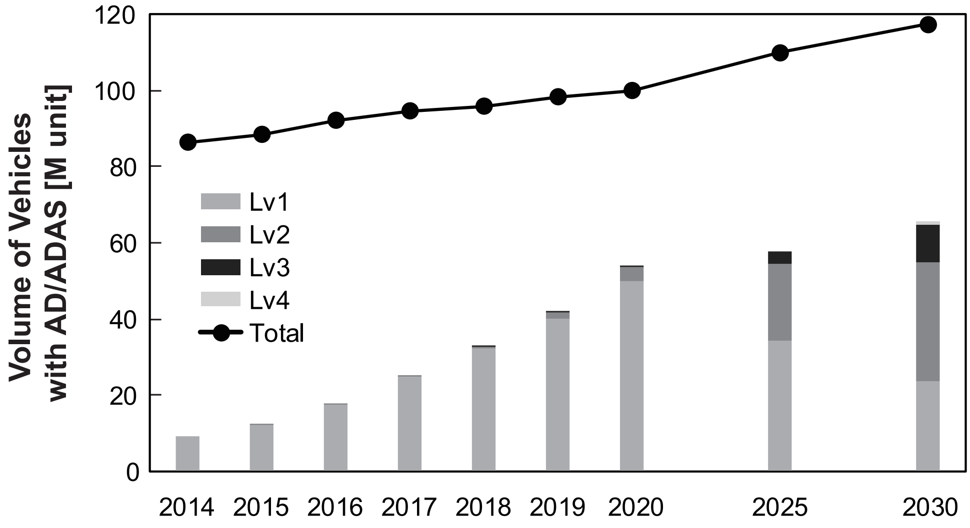

Fig. 1.1. Trend in number of new vehicles with ADAD and AD systems produced in the world.

AD systems require various sensors to detect objects around the ego vehicle. Cameras, millimeter-wave radars, LiDARs (Light Detection and Rangings), and sonars are commonly used in the ADAS and AD systems. In such sensors, millimeter wave radar is a key sensor due to their robust sensitivity under harsh weather conditions such as rain, fog, and bright sunlight. A lot of technologies have been investigated on millimeter-wave radars and improvement of antenna is an effective way to improve both detection performance and size of the radars.

In this dissertation, I report the results of the investigation about newly proposed structures of antennas and front-end modules for automotive millimeter-wave radars using the 77-GHz band, especially focusing on a high performance, downsizing, productivity, and cost reduction. First, social issues expected to be solved by the ADAS and AD systems, regulations on the ADAS and AD systems, position of millimeter-wave radars in the systems, and an operation principle of millimeter-wave radars focused on this study are explained in Chapter 1 in order to clarify that this study relates to solve social issues. Next, previous works on antennas and peripheral technologies for millimeter-wave applications and their issues are described and discussed in Chapter 2. Then, new structures for antennas and front-end modules are proposed and discussed in Chapters 3 to 5. In the chapters, the measurement results of fabricated antennas and versatility of the proposed technologies are also presented and discussed. Finally, the key points of this study and future works are summarized in Chapter 6.

1.2 Social issues expected to be solved by ADAS and AD systems

The ADAS and AD systems are expected to be a technology that solves social issues. In this section, I explain the issues by consulting SDGs (Sustainable Development Goals) as the most common challenges shared in the world, which were adopted at the United Nations General Assembly held in September 2015. The SDGs consist of 17 international goals and 169 targets which should be achieved by 2030 [1.5]. The ADAS and AD systems mainly relate to the goal 3 “Ensure healthy lives and promote well-being for all ages” and goal 11 “Make Cities and human settlements Inclusive, safe, resilient and sustainable”. The targets in each goal are described as follows:

Target 3.6. By 2020, halve the number of global deaths and injuries from road traffic accidents.

Target 11.2. 2030, provide access to safe, affordable, accessible and sustainable transport systems for all, improving road safety, notably by expanding public transport, with special attention to the needs of those in vulnerable situations, women, children, persons with disabilities and older persons.

Target 11.a. Support positive economic, social and environmental links between urban, peri-urban and rural areas by strengthening national and regional development planning.

1.2.1 Reduction of traffic accidents and fatalities

The number of fatalities by traffic accidents in the world was 1,350,000 people in 2018 and the number has been increasing, according to a report by the World Health Organization [1.6]. Contrary to the trend in the world, the number 3532 of fatalities caused by traffic accidents in Japan in 2018, which has been decreasing by 162 people over the previous year and was the lowest in the statistics since 1948, according to a report by the National Police Agency [1.7]. Fig. 1.2 shows the number of traffic accidents, injuries, and fatalities in Japan since 1950. The circles, triangular, and squares indicate the number of accidents, injuries, and fatalities, respectively. The arrows show the time when the seatbelt, airbag, crushable body structure, ABS (Anti-lock Braking System), and ESC (Electronic Stability Control) began to be mandated or installed, and the time when regulations drunken driving were tighten. As announced by the National Police Agency, the decrease in the number of fatalities caused by traffic accidents was an achievement of patrolling and announcement for safety driving. In

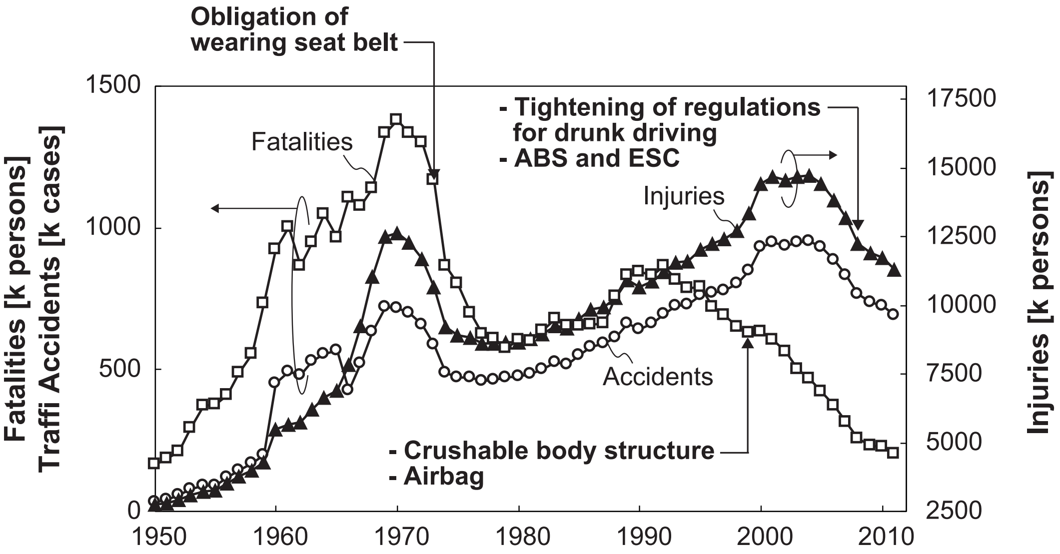

Fig. 1.2. Number of traffic accidents, injuries, and fatality in Japan.

addition to the effects of such soft measures, there is also the effect of the hard measures described above. According to SUBARU's announcement, the collision rate and pedestrian accident rate of vehicles equipped with the AEBS using a stereo camera "EyeSight" have declined by 84% and 49%, respectively [1.8]. Therefore, further technologies on the ADAS and AD systems are expected to reduce the number of traffic accidents and fatalities.

1.2.2 Providing transport systems for all

Public transportation in rural areas has continued to decline, according to the announcement from the Ministry of Land, Infrastructure, Transport and Tourism [1.3].

- In the 19 years between 2000 and 2018, 41 routes nationwide and 895.3 km of railroad were abolished, and the abolition route length are increasing.
- In 2017, 73 of the 96 regional railroad operators had a deficit in the management balance.
- In the six years from 2010 to 2015, about 7509 km of the general route bus line was abolished, and its capability of transportation was reduced by 35% (6.5 billion people in 1990 to 4.2 billion people in 2016).

In order to compensate the decrease of public transportation in such a rural area by a low-cost mobility service that does not hang labor costs, demonstration experiments cooperated by private sectors, such as autonomous driving bus, robot taxi, and autonomous driving cart, have been done in various region in Japan [1.9]. Moreover, the

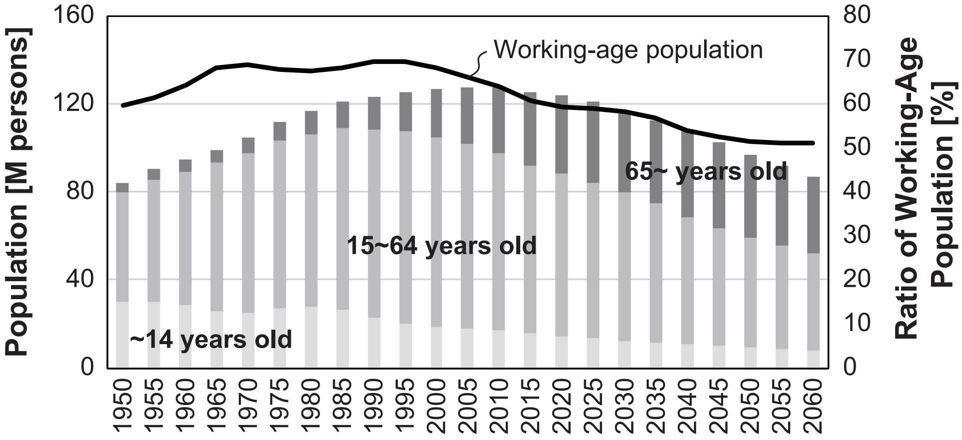

Fig. 1.3. Population composition and working-age population in Japan.

demonstration experiments of the autonomous driving bus have also been advanced in various places. For example, autonomous driving buses are being carried out in the Vienna suburbs of Austria [1.10] and Singapore [1.11].

1.2.3 Measures to decline in working-age population

The aging population and the decline in working-age population are major social issues in developed countries. Fig 1.3 shows the domestic population composition and the working-age population (15 to 64 years old) since 1950, which were announced by the Ministry of Internal Affairs and Communications in 2018 [1.12]. The ratio of the working-age production in Japan will decrease after 2000 and will drop to about 50% in 2060. Moreover, a lack of labor is serious in an occupation of driving. The transition of the active opening rate since 1995 announced by the Ministry of Health, Labor and Welfare is shown in Fig. 1.4 [1.13]. The active opening rate for both whole occupations and the occupation of driving have been increased after 2009, meaning a lack of labor. In particular, the active opening rate of whole occupations and the occupation of driving are 2.98 and 1.45 in 2018, respectively, which means that the lack of labor in the occupation of driving is serious situation.

ADAS and AD technologies have been attracting attention as a technology to defuse this situation, and demonstration experiments have been underway for an AD that assumes long-distance transport trucks on highways. Truck platooning is a candidate of the technology where multiple trucks are drove with a short distance and subsequent trucks follow the preceding trucks. This function leads to improvement of a working environment by reducing driving load, for example, the drivers for the subsequent trucks is not required or can be resting on highways. The improvement of the working environment is expected to increase in the number of people who would

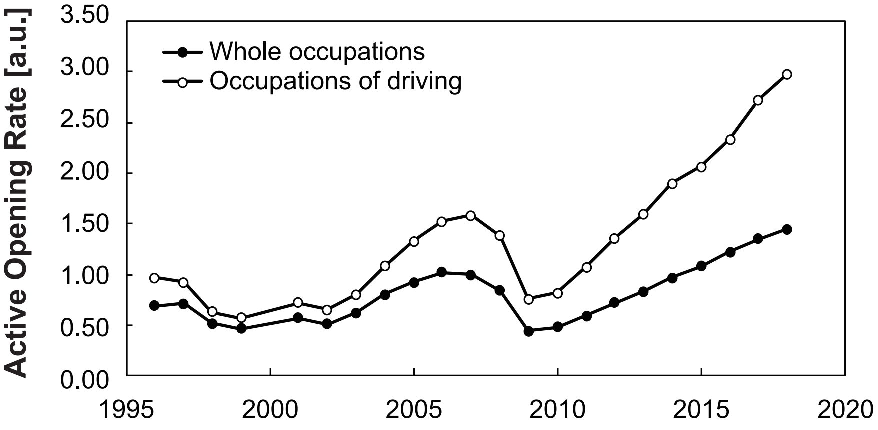

Fig. 1.4. Active opening rate for whole occupations and occupation of driving.

like to be engaged in this occupation.

In the United States of America, the PATH program in the UC Berkeley Institute has been developing the truck platooning technology since the 1990s [1.14]. In Europe, the truck platooning named “KONVOI ” had been investigated by the Ministry of Transport, Aachen University of Technology, and their partners during 2005 to 2009 [1.15]. In 2016, demonstration experiments were conducted on public roads at the European Truck Platooning Challenge [1.16]. In Japan, a demonstration experiment of the truck platooning is being carried out by SIP (Cross-ministerial Strategic Innovation Promotion program) of the Strategic Innovation Creation program of the Cabinet Office. A demonstration experiment using four trucks was done on the Shin-Tomei Expressway in 2019. In the experiment, a millimeter-wave radar was equipped to the front of the trailing truck to detect the gap between the trucks.

As described above, researches and developments for the practical use of the AD technology are being promoted all over the world to solve the social issue on lack of labors in the occupation of driving.

1.2.4 Reduction of environmental impact

In addition, the ADAS and AD technologies have been also expected to improve energy utilization efficiency by the congestion mitigation and fuel efficiency improvement. The improvement of energy utilization meets the direction of the target 7.3 “By 2030, double the global rate of improvement in energy efficiency” in the goal 7 “Ensure access to affordable, reliable, sustainable and modern energy for all” in the SDGs. The truck platooning described in the previous section can improve fuel efficiency (in four platoons with gap of 4.7 m, the average fuel consumption of 4 trucks is reduced by 18% [1.15]) as well as reduce the load of the drivers. The fuel consumption is improved because the resistance by the wind of the subsequent truck is reduced by narrowing the gap between the trucks.

According to the above discussions in Sections 1.2.1 to 1.2.4, the ADAS and AD systems are being developed to solve social issues such as reduction of traffic accidents, providing transport system in rural areas, measures to a decline in the working-age population, and reduction of environmental impact. To develop new technologies for the ADAS and AD systems in various countries, it is necessary to standardize their functions. In the next section, I will explain standardization and regulatory trends for the ADAS and AD systems.

1.3 Standardization and regulatory trends for ADAS and AD systems

There are regulations and assessments for vehicles with the ADAS and AD systems. First, standardized definition for levels of driving automation is explained in this section, which is commonly used as a classification standard of the ADAS and AD systems. Next, procedures and organizations to create regulations on the systems and example of the regulations are described. Finally, assessments are introduced.

1.3.1 Definition for levels of driving automation

A definition for levels of driving automation is generally used in this field, which is defined by the Society of Automotive Definition by Engineers (SAE) where the National Highway Traffic Safety Administration (NHTSA) bases. The definition is composed of six stages of levels from 0 to 5 as listed in Table 1.1 [1.2].

DDT (Dynamic Driving Task) means the operation task of a vehicle (such as steering, acceleration, and braking) and OEDR (Object and event Detection and Response) indicates detection of obstacles and correspondence to events (such as a signal turned red). At level 0, the driver is responsible for the task to continue the driving such as external monitoring and response. Driver assistance functions such as a blind spot warning (informing the driver about the presence of a vehicle approaching from the adjacent lane behind during the lane change operation) and lane departure warning correspond to the level 0. The system which performs either one of the operations of the longitudinal or lateral direction corresponds to level 1 and one which performs both operations corresponds to level 2. For example, a system which performs only acceleration and braking is categorized in the level 1. A system which performs only steering is also categorized in the level 1. Contrary to the above systems, a system performs all operations of the acceleration, braking, steering is defined as the level 2.

Table 1.1. Definition for levels of driving automation defined by SAE.

Level	Name	Narrative definition	DDT		ODD	Example features
			Sustained vehicle motion control	OEDR		
0	No Driving Automation	The performance by the driver of the entire DDT, even when enhanced by active safety systems.	Driver	Driver	N.A	- Automatic emergency breaking - Blind spot warning - Lane departure warning
1	Driver Assistance	The sustained and ODD-specific execution by a driving automation system of either the lateral or the longitudinal vehicle motion control subtask of the DDT (but not both simultaneously) with the expectation that the driver performs the remainder of the DDT.	Driver and System	Driver	Limited	- Lane centering OR - Adaptive cruise control
2	Partial Driving Automation	The sustained and ODD-specific execution by a driving automation system of both the lateral and longitudinal vehicle motion control subtasks of the DDT with the expectation that the driver completes the OEDR subtask and supervises the driving automation system.	System	Driver	Limited	- Lane centering AND - Adaptive cruise control at same time
3	Conditional Driving Automation	The sustained and ODD-specific performance by an automated driving system of the entire DDT with the expectation that the DDT fallback-ready user is receptive to automated driving system issued requests to intervene, as well as to DDT performance-relevant system failures in other vehicle systems, and will respond appropriately.	System	System	Limited	Traffic jam chauffeur
4	High Driving Automation	The sustained and ODD-specific performance by an automated driving system of the entire DDT and DDT fallback without any expectation that a user will respond to a request to intervene.	System	System	Limited	- Local driverless taxi - Pedals / steering wheel may or may not be installed
5	Full Driving Automation	The sustained and unconditional (i.e., not ODD-specific) performance by an automated driving system of the entire DDT and DDT fallback without any expectation that a user will respond to a request to intervene.	System	System	Unlimited	Same as level 4, but feature can drive everywhere in all conditions

However, the operation of the vehicle to continue driving and the external monitoring are responsible to drivers, therefore, the level 2 or lower is categorized as the ADAS.

The AD system generally corresponds to systems with level 3 or higher functions. A major difference between the level 3 or higher and the level 2 or lower is that systems have responsibility to the OEDR for the level 3 or higher whereas driver has responsibility to that for the level 2 or lower. However, even in the level 3, the driver is required “fallback-ready” which means that diver has to response to a request for delegation of operation from the system and operate the vehicle. For example, following cases are assumed: when the system cannot continue designed operation because sensor performance degrades significantly due to environmental conditions or when the system is broken. According to the above definition, the AD system of the autonomous driving bus demonstrated in Singapore described in Section 1.2.2 is categorized in the level 3, since it requires the emergency response staff. Moreover, the ODD (Operational Design Domain) where the AD system is available is limited in the level 3. For example, a traffic jam assistance which can be used on highways and in low speed range is classified as the level 3.

Contrary to the level 3, the word “driver” disappears from the definition and is described as “user” in level 4 or higher. The definition indicates that passengers are not expected to operate the vehicle while the system operates that. Moreover, it is allowed the case that all passengers do not have driver’s license. In the level 4 or higher, vehicles without brake pedal, accelerator pedal, and steering wheel are also assumed. However, the ODD is still limited in the level 4. An AD system which can perform anytime and anywhere is categorized in level 5. Since the experiments on the truck platooning described in Section 1.2.3 were carried out in a limited area such as highways, the AD system for them corresponds to the level 4.

1.3.2 Regulations on ADAS and AD systems

Next, I describe the laws and regulations on the ADAS and AD systems. The safety standards for the AD system in Japan assumed to be the level 3 and 4 are stipulated by the amended Road Traffic Vehicle Act, which was established in May 2019. Since the AD system is being developed globally, international coordination, such as harmonization of vehicle standards and mutual recognition of certifications, is required. For example, by establishing a system to legislate and mutually authenticate the same automobile standards in country A and country B, if vehicles that passed certification in country A are exported to country B, the acquisition of a new certification to the vehicles in the country B will not be required. Thus, the international coordination can reduce distribution costs and shorten distribution periods.

The activities of the international cooperation on automobiles are conducted at the

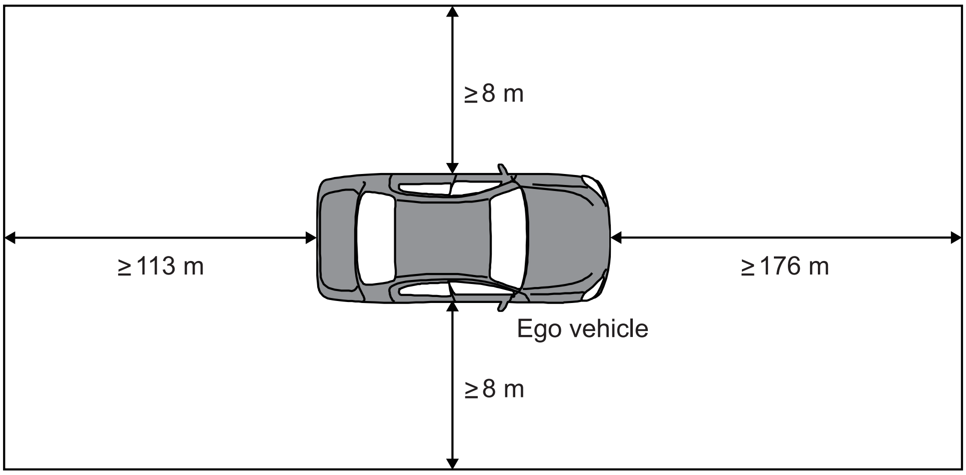

Fig. 1.5. Example of required sensor detection area for AD system discussed in UNECE.

UNECE (United Nations Economic Commission) [1.18], and the standards are being examined by a working party WP. 29 in the UNECE. For example, for the AEBS, the basic plan was agreed upon in WP. 29 in June 2019 and was issued as an international standard in January 2020. Under the agreement of this basic plan, the mandate of the AEBS for new vehicles in Japan will be enforced in 2021.

A required sensor detection area for AD is shown in Fig. 1.5 as an example of the requirements for an AD system discussed in the UNECE [1.19]. The required detection ranges from an ego vehicle are 176 m or more in forward direction, 8 m or more in lateral direction, and 113 m or more in backward direction. The detection range of the front is a braking distance required to stop the ego vehicle behind a stopped vehicle under a condition that an ego vehicle's speed is 130 km/h and deceleration is 3.7 m/s^2. The lateral sensing distance is the distance required for detecting vehicles or other objects such as motor bicycles in adjacent lanes. The detection range of the rear is defined by assuming following scenario: a vehicle with the speed of 130 km/h which is approaching from the rear side in the adjacent lane can travel without collision and with reasonable deceleration when the ego vehicle with the speed of 60 km/h changes lanes from current lane to the adjacent lane. The UNECE defines requirements for the AD system and performance standards such as braking distances and those are legislated in each country.

1.3.3 Assessments for ADAS and AD systems

In parallel with the legislation described in the previous section, assessments that evaluate safety of automobiles have also begun to be common. New Car Assessment Programme (NCAP) has been launched in the North America since 1979 and introduced

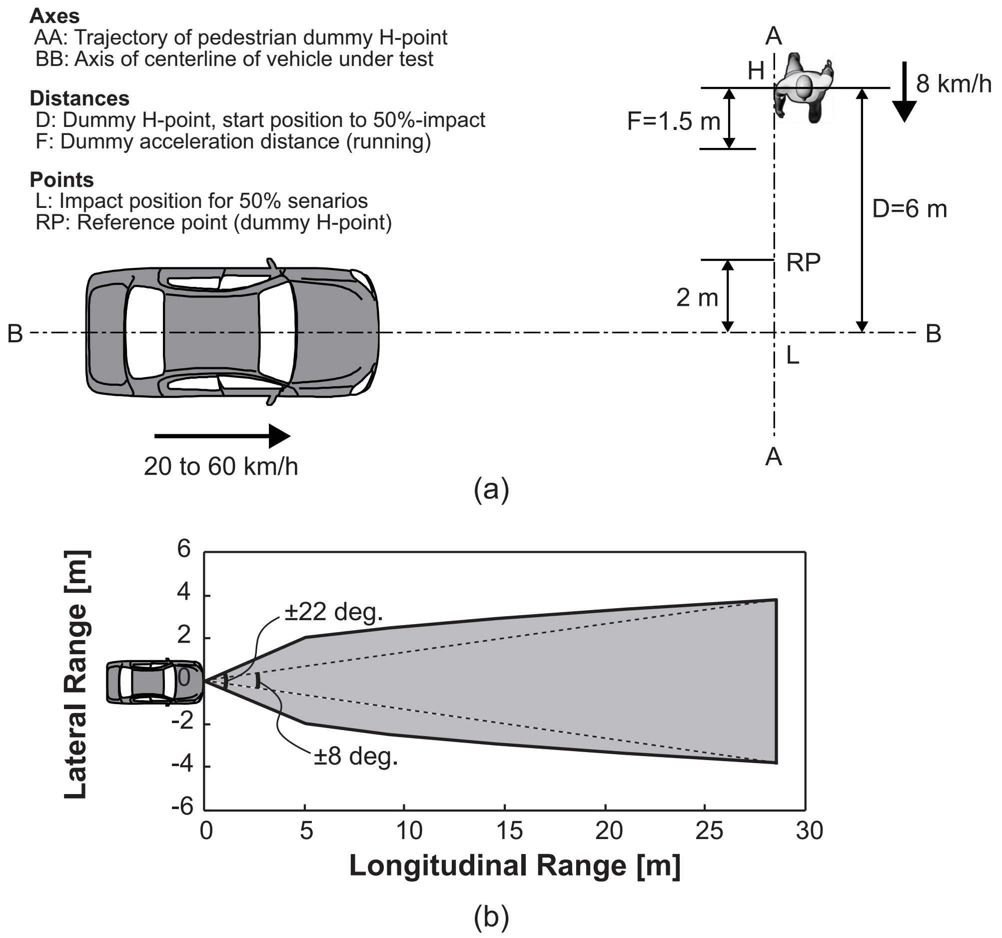

Fig. 1.6. (a) Test protocol for AEBS to avoid collision with adult pedestrian running across the road and (b) required sensing area.

in Europe [1.20], Japan [1.21], Asia [1.22], and other countries around the world. In the NCAP, safe performance of a new vehicle is evaluated by the number of stars up to five based on test results of defined protocols. The international standards prescribed by the UNECE are legal and must be complied with in all new vehicles. Contrary to the standards, the NCAP is an evaluation criterion for safety and is not obliged to do so, but it is used as an authoritative result for the promotion of safety to end users in order to improve sales volume. In fact, the NCAP evaluation results are posted on the home page of each NCAP institution and are used for the selling point of car manufacturers.

As an example, Fig. 1.6(a) shows a test protocol for an AEBS to avoid collision with an adult pedestrian running across the road defined in the Euro NCAP. In the test protocol, the speed of an ego vehicle is changed from 20 to 60 km/h and that of the pedestrian is 8 km/h. The condition “impact position for 50%” means that the ego vehicle and pedestrian collide at the front-center of the ego vehicle if the AEBS is not enough to avoid the collision. Fig. 1.6(b) shows the required sensing area in order to support the test protocol shown in Fig. 1.6(a), where a sensor is equipped at the front-center of the ego vehicle. As shown in the figure, sensors equipped for a forward sensing are required a wide field-of-view (FOV) of about ±22 degrees in a short range of about 5 m whereas those are required a narrow FOV of about ±8 degrees in a middle range of about 28 m. Thus, a sensing system which has such wide FOV is required to support the NCAP. (The FOV and detection range depend on the equipped position of the sensors in the ego vehicle, a delay time between detecting a pedestrian and starting braking, and delay of braking due to the weight of the ego vehicle.)

The test protocols of the Euro NCAP had been limited in use-cases when the ego vehicle drives on the street until 2018. However, the ODD will be expanded to junctions from 2020. Moreover, the test conditions will be expanded from daytime to night in the future. Therefore, further technologies on the ADAS and AD systems will be needed to meet requirements of the NCAP.

1.4 Sensor configurations and part of radars in ADAS and AD systems

To comply with laws and regulations and to obtain a high score in such a test protocol defined in the NCAP, vehicles should be equipped with various sensors. In this section, I explain a sensor configuration for vehicles with the ADAS or AD systems based on characteristics of each sensor. I also describe purpose to apply millimeter-wave radars to the vehicles.

Cameras [1.23], millimeter-wave radars [1.24], LiDARs [1.25], and sonars [1.26] are generally used for the ADAS and AD systems. Table 1.2 shows the comparison of the detection characteristics and price of each sensor. The characteristics and prices are evaluated relatively among sensors in each item, basing on the following four stages; Excellent, Good, Fair, and Poor. Here, since the results are based only a relative evaluation between sensors, a sensor can be used to the ADAS and AD systems if its performance is sufficient for functional requirements of the systems. Therefore, the evaluation results do not indicate the applicability of the sensors to the ADAS and AD systems.

A camera commonly has a long detection range and high spatial resolution while it has a fair detection range accuracy (detection range accuracy decreases as the distance to a target increases) due to its principle of operation. On the contrary, a millimeter-wave radar which is commercially available has a long detection range and high detection range accuracy while it has a fair spatial resolution due to its principle of

Table 1.2. Comparison of the detection characteristics and price of sensors.

	Camera Monocular / Stereo	Radar	Lidar	Sonar
Detection Range	Good	Excellent	Fair	Poor
Detection Range Accuracy	Fair / Good	Excellent	Excellent	Poor
Velocity Detection Accuracy	Fair / Good	Excellent	Good	Poor
Spatial Resolution	Good	Fair	Good	Poor
Classification	Excellent	Poor	Good	Poor
Ego-vehicle Velocity	Good (Whole speed range)	Good (Whole speed range)	Good (Whole speed range)	Fair (Low speed)
Environment Condition	Fair (weak to rain, snow, fog, back-light etc.)	Good	Poor (weak to rain, snow, fog, back-light etc.)	Fair (weak to wind)
Time Zone	Poor (at night)	Good	Good	Good
Price	Good / Fair	Good	Poor	Excellent

operation. Moreover, the camera can identify whether the detected object is a person, car, bicycle, and so on; however, the detection performance degrades under harsh weather conditions (such as heavy rain, snow, and fog) and depends on the brightness of the environment (such as darkness and backlight). Contrary to the camera, the radar commonly has a poor classification performance; however, the detection performance does not degrade due to such environments of the ego vehicle.

A LiDAR generally has a high detection range accuracy, high spatial resolution, and good classification performance (the performances mainly depend on the number of layers in the LiDAR). The detection performance does not degrade in a dark; however, it degrades in the condition of rain and snow. A sonar has a short detection range and poor spatial resolution. The detection performance degrades due to the wind, therefore, the sonar can be applied when the speed of the ego vehicle is slow. However, the price of the sonar is much smaller than other sensors, therefore, it is commonly used for a parking support system.

As described above, since the sensors have advantages and disadvantages, it is significant to improve the performance of peripheral sensing of the ego vehicle by combining the sensors with a complementary relationship in the ADAS and AD systems.

Fig. 1.7 shows an example of a sensor configuration in a vehicle with the ADAS or AD systems. The right direction is the front direction of the ego vehicle in the figure. The peripheral sensors consist of a long-range radar (LRR), meddle-range radars (MRRs), front camera, multi-view cameras, electronic mirrors, LiDAR, and sonars.

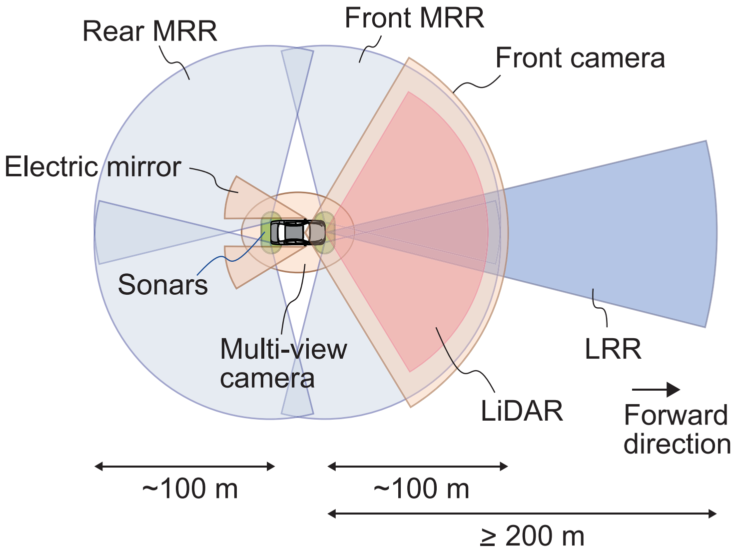

Fig. 1.7. Example of sensor configuration in vehicle with ADAS or AD systems.

Here, LRRs and MRRs commonly have detection range of about 200 and 100 m, respectively. The sensor configuration and its detection range and angle are optimized by functions required from the regulations of the UNECE, levels of driving automation defined by the SAE, test protocols of the NCAP, and safety performances in practical use. Therefore, the front camera only, front MRR only, or LRR only configurations are also conceivable in order to realize the function of ACC (Automatic Cruise Control) and AEBS at the level 1, since the functions requires sensing capability only in the front direction of the ego vehicle. However, since the system has responsibility for peripheral monitoring and correspondence in the level 3 or higher as described in Section 1.3.1, a redundant system is required, in which important areas to operate the ADAS or AD systems are detected by multiple sensors. In the sensor configuration shown in Fig. 1.7, the front sensing system has quadruple system with the front camera, LRR, MRRs, and LiDAR, and the front-side sensing system has triple system with the front camera, MRRs, and LiDAR.

As shown in Fig. 1.7, millimeter-wave radars are often used in combination with cameras because of their complementary performance on detection range accuracy, special resolution, classification performance, and robustness against the environmental conditions. In particular, since the ADAS and AD systems are required to work at any time and in any environmental conditions, the millimeter-wave radar is a key sensor for the systems. For example, in snowy roads where lane markers and road edge are unclear, a technique for detecting the position of the snow pole installed at the roadside by using a millimeter-wave radar has been studied in order to recognize a drivable area [1.27].

According to the above discussions in Sections 1.3 to 1.4, the required area of peripheral sensing is determined by requirements of needed function to comply with laws and regulations and to obtain a high score in such a test protocol defined in the NCAP. Commonly used sensors include cameras, millimeter-wave radars, LiDARs, and sonars. Although millimeter-wave radars have poor object classification performance, they have robust sensitivity under conditions such as rain, snow, fog, and bright sunlight in which camera performance is degraded. Thereby, millimeter-wave radar sensing is necessary to achieve robust sensing for the ADAS and AD systems. In the next section, I will outline a regulation, operation principle, and configuration of millimeter-wave radars.

1.5 Automotive millimeter-wave radars

In this section, first, I explain lows and regulations on millimeter-waves radars for automotive applications. Next, a principle of operation and configuration of millimeter-waves radars are described as a background of this study. Finally, a dual-range dual-FOV radar is introduced, which is focused on this dissertation.

1.5.1 Regulation on millimeter-wave radars

Since millimeter-wave radars use radio waves, they have to meet the frequency band and emitted power prescribed by the Radio Act in each country. Table 1.3 summarizes the frequency bands and applications used in the current millimeter-wave radars for automotive applications [1.12]. The frequency band of 24-GHz, 76-GHz, and 79-GHz are commonly used at the timing of writing.

The 24-GHz band was used by an ultra wide-band (UWB) radar that could use up to the 26-GHz band and that was commercialized in Japan in 2010. However, the 24-GHz UWB (21.65 to 26.65 GHz) was abolished in 2013 in Europe. Currently only the 24-GHz narrowband (24.05 to 24.25 GHz) is available [1.12]. Moreover, an equivalent isotropically radiated power (EIRP) from a transmitter (Tx) antenna of a radar is limited to a low value of -41.3 dBm/MHz. Thus, radars with the 24-GHz band are used for sensing applications around the ego vehicle, which do not require a high spatial resolution and detection performance for objects with a low radar cross section (RCS) such as pedestrians.

The 77-GHz band was assigned to automotive applications in Japan in 1999. Since the limitation of the EIRP has a large value of 50 dBm (average), the band is used as LRRs or MRRs, where LRRs have the long detection range (200 m or more) and narrow FOV and MRRs have the detection range of about 100 m and wide FOV up to

Table 1.3. Regulated frequency band and radiated power for millimeter-wave radars and their uses.

Band	Frequency [GHz]		EIRP		Use
24 GHz	EU	24.0~24.25	EU	-41.3 dBm/MHz	Short and middle-range radar to detect mainly vehicle within about 30 m in front and rear of ego vehicle.
	NA	23.12~29.0	NA	-61.3 dBm/MHz (23.6~24 GHz) -41.3 dBm/MHz (other)	
	JP	24.05~24.25	JP	-41.3 dBm/MHz	
77 GHz	76.0~77.0		EU	Average 50 dBm Peak 55 dBm	- Middle-range radar to detect objects (vehicle, pedestrian, cyclist etc.) within about 100 m around ego vehicle. - Long-range radar to detect objects more than 200 m ahead.
			NA	Average 50 dBm at 3 m Peak 50 dBm at 3 m	
	76.0~77.0 500 MHz in normal modulation		JP	10 dBm at feed point Antenna gain: Max. 40 dB	
79 GHz	77.0~81.0		EU	Average -3dBm/MHz Peak 55 dBm	Short and middle-range radar to detect small objects with high resolution within about 100 m around ego vehicle.
			NA	Average 50 dBm Peak 50 dBm	
			JP	10 dBm at feed point	

150 degrees [1.28]. The spatial resolution (especially range resolution) of radars with the 77-GHz band is higher than that of radars with 24-GHz band because the former radars can use wider frequency bandwidth. Therefore, the radars with the 77-GHz band can be applied to detect smaller objects than vehicles, such as pedestrians.

It should be noted that an input power at the feed point of antenna is limited to 10 dBm or less in Japan, whereas the 77-GHz band is allowed to have the EIRP of 50 dBm in Europe and North America.

While the 77-GHz band is allowed to use frequency bandwidth 500 MHz in Japan, the 79-GHz band can use a bandwidth of 4 GHz. Therefore, it is possible to improve the range resolution compared with the 77-GHz band [1.29]. For example, vehicles and pedestrians can be detected by separating even in places where the vehicle and pedestrians crowded such as a parking area. Thus, MRRs with the 24-GHz and 77-GHz band will be replaced by those with 79-GHz band in the future.

In addition, the 60-GHz band has also been assigned in 1995 to a vehicle application in Japan, which is not listed in Table 1.3. However, the 60-GHz band is not currently used as the radars for the peripheral sensing because of following two reasons: the band is not assigned to radars for peripheral sensing in Europe and North America, and the band has a problem that a detection of targets at long distance is difficult due to the attenuation of electric-wave by the air (oxygen molecules). However, the 60-GHz band has advantage that the electric-wave with 60-GHz band has less influence on other wireless devices due to the large attenuation by the air. Thus, the band is expected to use as a passenger monitoring sensor in the cabin of the ego vehicle by taking advantage of the feature [1.30], such as “Child Presence Detection” which is a test protocol in the Euro NCAP that will be implemented from 2022.

In this study, millimeter-wave radars using the 77-GHz band is focused because the targeted dual-range dual-FOV radars should have long-range detection as detailed in Section 1.5.4.

1.5.2 Operation principle of millimeter-wave radars

This section outlines an operation principle of millimeter-wave radars for automotive applications, regarding a range, velocity, and angular detections.

First, I explain an operation principle to detect range and velocity of a target. The millimeter-wave radars mainly use the frequency modulated continuous wave (FMCW) [1.31], fast chirp [1.32], or 2-frequency CW [1.31] as a modulation method for transmitting waves. In this section, the FMCW is applied as an example.

Fig. 1.8 shows (a) a circuit configuration, and (b) transmitted and received waveforms of an FMCW millimeter-wave radar. As shown in Fig. 1.8, a transmission antenna radiates an electric-wave with the center frequency f_0 and modulation bandwidth $2\Delta f$, and a receiver (Rx) antenna receives a reflected wave from a target at the distance L. The center frequency of the received signal becomes $f_0 + f_d$ by the Doppler shift corresponding to the target speed v. Here, f_d is called the Doppler frequency. The received signal is down-converted to a signal with a kHz order frequency by multiplying the received signal and partial of the transmitted signal in a mixer. The down-converted signal is called a beat signal because the signal has periodicity and its shape is rectangular as shown in the lower side of Fig. 1.8(b).

In the upper side of Fig. 1.8(b), the solid and dashed lines are the waveform of the transmitted and received signals, respectively. In the figure, T is a modulation period of the transmitted signal and c is the speed of light. The waveform of the received signal shifts $\frac{2L}{c}$ in the time direction compared with that of the transmitted signal. The waveform of the received signal also shifts f_d in the frequency direction by the Doppler shift. The frequencies of the beat signal f_{B1} and f_{B2} shown in the lower side of Fig. 1.8(b) are represented by the following equations.

$$f_{B1} = \frac{4f_0L}{cT} - f_d \tag{1.1}$$

$$f_{B2} = \frac{4f_0L}{cT} + f_d \tag{1.2}$$

The Doppler frequency f_d is described by the following equation.

$$f_d = -\frac{2f_0v}{c} \tag{1.3}$$

Therefore, the distance L and speed v of the target are obtained from the equations

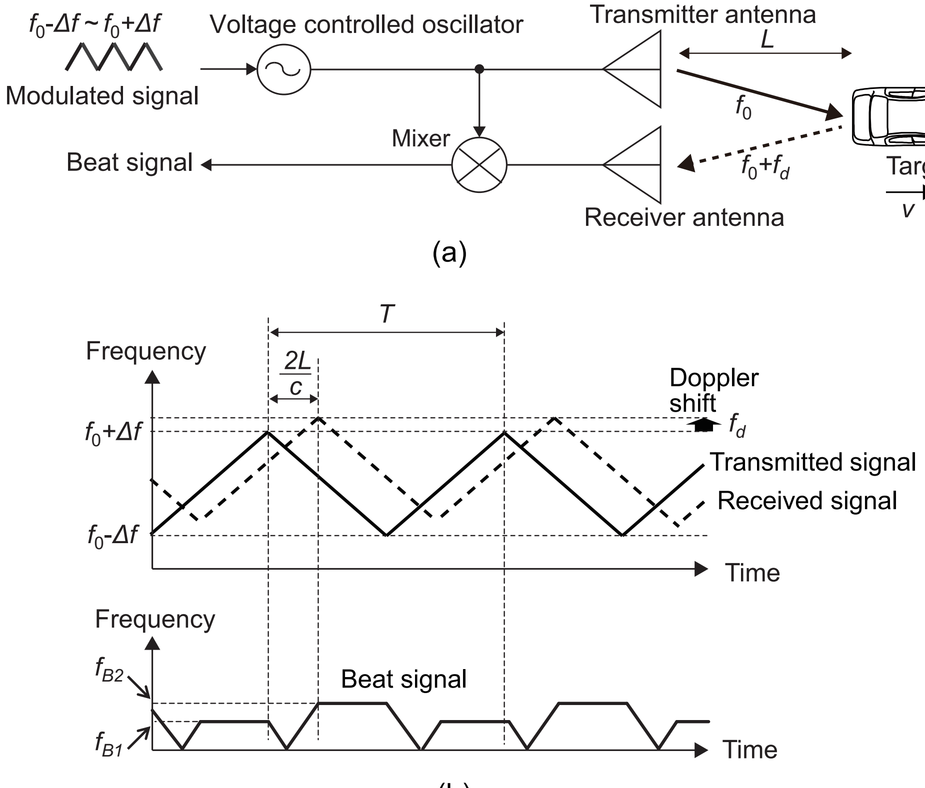

(a)

(b)

Fig. 1.8. Operation principle of millimeter-wave radar to detect range and velocity of target.

(1.1) to (1.3) and are expressed as follows:

$$L = \frac{cT}{8f_0}\left(f_{B1} + f_{B2}\right) \tag{1.4}$$

$$v = \frac{c}{4f_0}\left(f_{B1} - f_{B2}\right) \tag{1.5}$$

These equations indicate that the distance and speed of the target can be provided by measuring the voltages corresponding to the frequencies f_{B1} and f_{B1} of the beat signal.

Maximum detection range $L_{\max}$ is represented by the following Fisher's equation [1.31]. Here, P_t is a power at the feed point of the Tx antenna, G_t and G_r are antenna gains of the Tx and Rx antennas, respectively, $P_{r\min}$ is a minimum receivable power, σ is an RCS of the target, and λ_0 is the wavelength in the free space.

$$L_{\max} = \left[\frac{P_t G_t G_r \lambda_0^2 \sigma}{(4\pi)^3 P_{r\min}}\right]^{\frac{1}{4}} \tag{1.6}$$

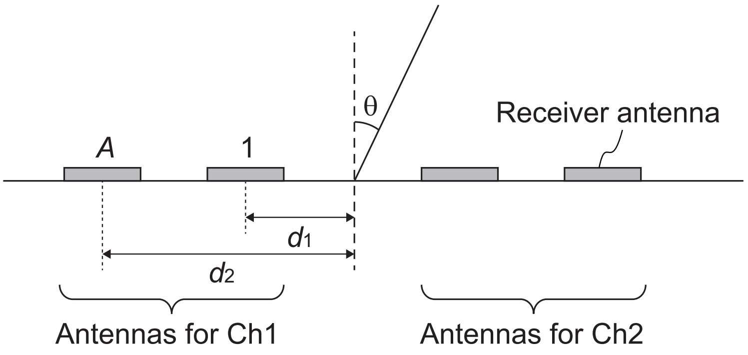

Fig. 1.9. DOA estimation by using phase-shifted monopulse method.

Next, I describe a method for direction of arrival (DOA) estimation as an angular detection of millimeter-wave radars. The phase-shifted monopulse method [1.33] and MUSIC (multiple signal classification) [1.34] are commonly used to the DOA estimation. Here, I explain the DOA estimation by using the phase-shifted monopulse method, which was applied in this study. In the phase-shifted monopulse method, the DOA estimation is done by comparing the phase difference of the received signals of Rx antennas. An arrangement of the Rx antennas is illustrated in Fig. 1.9.

Here, two channels Ch1 and Ch2 are arranged symmetrically with the central axis indicated by the dashed line in the figure, and each channel is composed of two antennas. The voltage amplitudes of the received signal in the Rx antennas are 1 and A when the phase of the received signal in the Rx antennas are the same in each channel. d_1 and d_2 are distances between the Rx antennas and the central axis, and θ is an arrival angle of the received signal. Since the received signal power P_1 of Ch1 is described

$$P_1 = A\exp\left(j2\pi d_2\lambda_0\sin\theta\right) + \exp\left(j2\pi d_1\lambda_0\sin\theta\right), \tag{1.7}$$

the phase angle ϕ_1 of the received signal of Ch1 is provided by the following equation:

$$\tan\phi_1 = \frac{A\sin\alpha + \sin\beta}{A\cos\alpha + \cos\beta}, \tag{1.8}$$

where α and β are defined by the following equations:

$$\alpha = 2\pi d_2\lambda_0\sin\theta, \;\; \beta = 2\pi d_1\lambda_0\sin\theta \tag{1.9}$$

Similarly to the Ch1, the received signal power P_2 of Ch2 is obtained by the following equation:

$$\tan\phi_2 = -\frac{A\sin\alpha + \sin\beta}{A\cos\alpha + \cos\beta} \tag{1.10}$$

Therefore, the phase difference between received signals in Ch1 and Ch2 is described as follow:

$$\phi_2 - \phi_1 = -2\tan^{-1}\frac{A\sin\alpha + \sin\beta}{A\cos\alpha + \cos\beta} \tag{1.11}$$

The DOA estimation can be done by measuring the phase difference between received signals ($\phi_2 - \phi_1$) and calculating θ by using the equations (1.9) and (1.11).

1.5.3 Configuration of millimeter-wave radars

I explain a general configuration of a millimeter-wave radar using the 77-GHz band in this section. Fig. 1.10 shows a circuit block diagram and hardware configuration of the millimeter-wave radar. The millimeter-wave radar consists of a front-end module and back-end circuit. The front-end module mainly consists of a Tx and Rx antennas and a transceiver circuit implemented in monolithic microwave integrated circuits (MMICs) [1.35–1.37], which work in the 77-GHz band. The modulation and demodulation circuits for generating the modulation signal and beat signal described in Section 1.8 are also integrated on the front-end module. A VCO (Voltage Controlled Oscillator) which generates transmission frequency (f_0) is also mounted on the front-end module. The back-end circuit mainly consists of a signal processor, voltage source, and CAN (Controller Area Network) adapter, which are operated at frequencies below MHz.

In this study, the front-end module was focused considering a high performance, downsizing, productivity, and cost reduction.

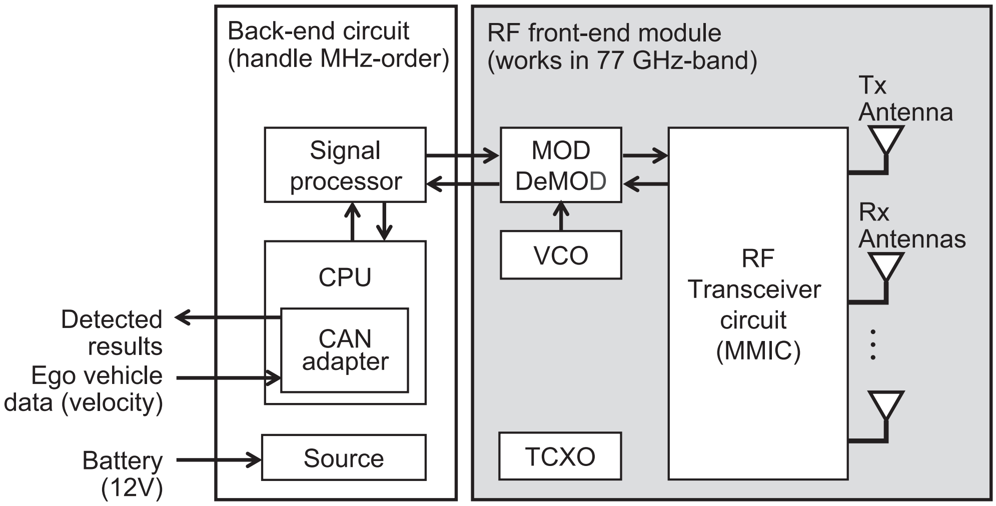

Fig. 1.10. Configuration of millimeter-wave radar using 77-GHz band.

1.5.4 Dual-range dual-FOV radars

Millimeter-wave radars for automotive applications are commonly categorized on the basis of their detection range: LRR, MRR, and short-range radar (SRR) as described in Section 1.4 [1.28]. LRR is usually used to detect obstacles at distances over 200 m in front of the ego vehicle for applications such as pre-crash warning and adaptive cruise control. MRR is usually used to detect objects around the ego vehicle within about a 100-meter range, so MRR requires a wider FOV than LRR. For example, the FOV of more than ±22 degrees is required to meet the protocol in the Euro NCAP illustrated in Fig. 1.6(a). SRR is used to detect objects around the ego vehicle to cover blind spots in the MRR coverage so as to provide a radar cocoon around the ego vehicle. Each type of radar is commonly produced separately; now, however, a new type of radar that covers both the LRR and MRR detection areas [1.38] using the 77-GHz band is needed to obtain more redundant sensing in front of the ego vehicle.

Fig. 1.11 shows an example of the detection area required for a dual-range dual-FOV radar: an azimuth beamwidth of $\pm 7.5 \sim 10$ or more degrees in LRR-mode (long-range detection with narrow FOV), one of ±35 or more degrees in MRR-mode (middle-range detection with wide FOV), and an elevation beamwidth of $5 \sim 7$ or less degrees in both modes.

A radiation pattern needed to attain the target gains for the Tx antennas for LRR- and MRR-modes is shown in Fig. 1.12. The target gains in this study are 21 dBi at boresight for LRR-mode and 15 dBi or more within azimuth angles of ±35 degrees for MRR-mode to obtain the detection areas shown in Fig. 1.11. The antenna gain at azimuth angles of ±35 degrees needed to achieve a detection range of 100 m was derived from the gain at boresight needed to achieve a detection range of 200 m by using the Fisher's equation (1.6). The detection range in MRR-mode is half that in LRR-mode, so the difference in antenna gain between at azimuth angles of ±35 degrees for MRR-mode and at boresight in LRR-mode should be 6 dB or less, when common Rx antennas are used for both modes. Switching between the narrow-beamwidth and the wide-beamwidth antenna was assumed to be done in accordance with the mode.

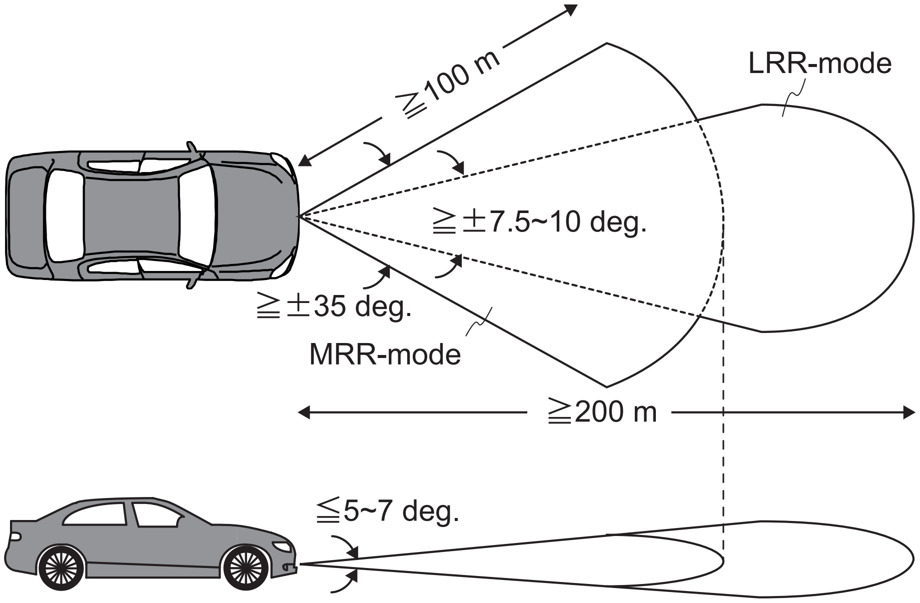

Fig. 1.11. Example of required detection area for front-facing dual-range dual-FOV radar on vehicle equipped with ADAS or AD systems: azimuth FOV (top) and elevation FOV (bottom).

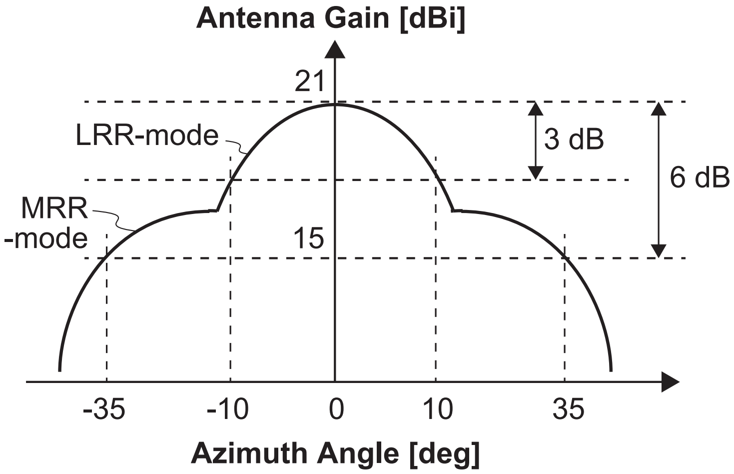

Fig. 1.12. Radiation pattern for Tx antenna needed to achieve detection area for dual-range dual-FOV radar shown in Fig. 1.11.

1.6 Summary

The key points of this chapter are as follows:

- ADAS and AD systems are expected to solve social issues such as reduction of traffic accidents, providing transport system in rural areas, measures to a decline in the working-age population, and reduction of environmental impact, which meet the targets defined in the SDGs.
- Standardization and regulatory legislation for the ADAS and AD systems on a global scale are being promoted. Laws and regulations are discussed in the UNECE, and assessment criteria are defined in the NCAP in each region.
- A required area of peripheral sensing is determined by requirements of needed function to comply with laws and regulations and to obtain a high score in such assessment criteria defined in the NCAP.
- While millimeter-wave radars have poor object classification performance, they have robust sensitivity under conditions such as rain, snow, fog, and bright sunlight in which performance of cameras or LiDARs is degraded. Thus, the radars are necessary to achieve robust sensing for the ADAS and AD systems.
- A dual-range dual FOV radar which has both narrow FOV at a long-range detection and wide FOV at a middle-range detection is newly required to obtain more redundant sensing in front of the ego vehicle, which uses the 77-GHz band.

References

[1.1] S. P. Wood, J. Chang, T. Healy, and J. Wood, “The potential regulatory challenges of increasingly autonomous motor vehicles,” *52nd Santa Clara Law Review*, vol. 52, no. 4, pp. 1423–1502, Dec. 2012.

[1.2] “SAE J3016$^{\text{TM}}$ Surface Vehicle Recommended Practice,” Society of Automotive Engineers International, Jun. 2018.

[1.3] Ministry of Land, Infrastructure, Transport and Tourism
https://www.mlit.go.jp/index.html

[1.4] “Possibilities and Market Prospects of Autonomous Driving System 2015 – Development Trend of Tire1 and Car Makers,” Yano Research Institute Ltd., Jun. 2015. (in Japanese)

[1.5] “JAPAN SDGs Action Platform,” Ministry of Foreign Affairs of Japan, https://www.mofa.go.jp/mofaj/gaiko/oda/sdgs/index.html

[1.6] “Road traffic injuries,” WHO Fact Sheet, Dec. 2018.

[1.7] National Police Agency
https://www.npa.go.jp/index.html

[1.8] SUBARU Corporation
https://www.subaru.jp/safety/total/pre-crush.html

[1.9] Cabinet Office
https://www.kantei.go.jp/

[1.10] Wiener Linien
https://www.wienerlinien.at/auto-bus-seestadt

[1.11] “International consortium to start preparation to launch autonomous shuttle bus trial with NParks,” News Release of Willers, May 2019.

[1.12] Ministry of Internal Affairs and Communications
http://www.soumu.go.jp/

[1.13] Ministry of Health, Labor and Welfare
https://www.mhlw.go.jp/index.html

[1.14] D. N. Godbole and J. Lygeros, “Longitudinal Control of the Lead Car of a Platoon,” *IEEE Trans. Vehicular Tech.*, vol. 43, no. 4, pp. 1125–1135, Nov. 1994.

[1.15] S. Tsugawa, S. Jeschke, and S. E. Shladovers, “A Review of Truck Platooning Projects for Energy Savings,” *IEEE Trans. Intelligent Vehicles*, vol. 1, no. 1, pp. 68–77, Mar. 2016.

[1.16] S. Ellwanger and E. Wohlfarth, “Truck platooning application,” in *Proc. of the 9th IEEE Intelligent Vehicles Symp.*, pp. 966–971, Jun. 2017.

[1.17] New Energy and Industrial Technology Development Organization
http://www.nedo.go.jp/

[1.18] UNECE WP.29
https://www.unece.org/trans/main/wp29/introduction.html

[1.19] “Safety Distance and Object Classifications for ACSF,” Information Document ASCF-04-05, Federal Ministry of Transport and Digital Infrastructure, Nov. 2015.

[1.20] Euro NCAP
https://www.euroncap.com/en

[1.21] National Agency for Automotive Safety & Victims’ Aid
http://www.nasva.go.jp/mamoru/

[1.22] ASEAN NCAP
http://www.aseancap.org/v2/

[1.23] H. Weigel, P. Lindner, and G. Wanielik, “Vehicle Tracking with Lane Assignment by Camera and Lidar Sensor Fusion,” in *Proc. of IEEE Intelligent Vehicles Symp.*, pp. 513–520, Jun. 2009.

[1.24] M. E. Russell, A. Crain, A. Curran, R. A. Campbell, C. A. Drubin, and W. F. Miccioli, “Millimeter-Wave Radar Sensor for Automotive Intelligent Cruise Control (ICC),” in *IEEE MTT-S Int. Microw. Symp. Dig.*, pp. 1257–1260, Jun. 1997.

[1.25] T. Ogawa, H. Sakai, Y. Suzuki, K. Takagi, and K. Morikawa, “Pedestrian Detection and Tracking using in-vehicle Lidar for Automotive Application,” in *Proc. of IEEE Intelligent Vehicles Symp.*, pp. 734–739, Jun. 2011.

[1.26] W.-J. Park, B.-S. Kim, D.-E. Seo, D.-S. Kim, and K.-H. Lee, “Parking Space Detection Using Ultrasonic Sensor in Parking Assistance System,” in *Proc. of IEEE Intelligent Vehicles Symp.*, pp. 1039–1044, Jun. 2008.

[1.27] A. Kajiwara, “Lane Environment Monitoring and Self-Localization Using 79 GHz Radar,” in *Proc. of the Microwave Workshop & Exhibition 2018*, pp. 301–304, Nov. 2018.

[1.28] J. Hasch, E. Topak, R. Schnabel, T. Zwick, R. Weigel, and C. Waldschmidt, “Millimeter-Wave Technology for Automotive Radar Sensors in the 77 GHz Frequency Band,” *IEEE Trans. Microw. Theory and Tech.*, vol. 60, no. 3, pp. 845–860, Jan. 2012.

[1.29] K. Ohguchi, M. Shono, and M. Kishida, “79 GHz Band Ultra-Wideband Automotive Radar,” *Fujitsu Ten Tech. J.*, no. 39, pp. 9–14, Mar. 2014.

[1.30] H.-R. Chuang, H.-C. Kuo, F.-L. Lin, T.-H. Huang, C.-S. Kuo, and Y.-W. Ou, "60-GHz Millimeter-Wave Life Detection System (MLDS) for Noncontact Human Vital-Signal Monitoring," *IEEE Sensors Journal*, vol. 12, no. 3, pp. 602–609, Mar. 2012.

[1.31] M. I. Skolnik, "Introduction to Radar Systems (3rd ed.)," McGraw-Hill Higher Education, 2001.

[1.32] S. Lutz, D. Ellenrieder, T. Walter, and R. Weigel, "On fast chirp Modulations and Compressed Sensing for Automotive Radar Applications," in *Proc. of the 15th International Radar Symposium*, pp. 1–6, Jun. 2014.

[1.33] M. I. Skolnik, "Introduction to Radar Systems Third Edition," McGraw-Hill, 2001.

[1.34] Y. Miyake, "Phased Array Technology for Automotive Radar Applications," in *Proc. of the Microwave Workshop & Exhibition 2018*, pp. 305–308, Nov. 2018.

[1.35] L. Maurer, G. Haider, and H. Knapp, "77 GHz SiGe Based Bipolar Transceivers for Automotive Radar Applications - An Industrial Perspective," in *Proc. of IEEE New Circuits and Systems Conf.*, pp. 257–260, Jun. 2011.

[1.36] T.-N. Luo, C.-H. E. Wu, and Y.-J. E. Chen, "A 77-GHz CMOS Automotive Radar Transceiver With Anti-Interference Function," *IEEE Trans. Circuits and Systems*, vol. 60, no. 12, pp. 3247–3255, Dec. 2013.

[1.37] N. H. Huynh, T. Saverio, M. Wojnowski, G. Haubner, S. Pahlke, J. Schmitt, H. Mayr, J. Würtele, U. Rueddenklau, I. Nasr, and J. S. Bal, "eWLB Package for Millimeter Wave Application," in *Proc. of the 2015 European Microelectronics Packaging Conf.*, pp. 1–5, Sep. 2015.

[1.38] S.-H. Jeong, H.-Y. Yu, J.-E. Lee, J.-N. Oh, and K.-H. Lee, "A Multi-Beam and Multi-Range Radar with FMCW and Digital Beam Forming for Automotive Applications," *Progress in Electromagnetics Research*, vol. 124, pp. 285–299, Jan. 2012.

Chapter 2

Issues on Antennas for Automotive Millimeter-wave Radars

2.1 Introduction

Issues on millimeter-wave radars for automotive applications, especially on dual-range dual-FOV radars, and those on a front-end module and antennas in the dual-range dual-FOV radars are explained in this chapter. First, the issues on the dual-range dual-FOV radars are introduced and broke down to technical issues on components which consist of a front-end module for the radars in Section 2.2. Next, a preferable structure, technologies for integration structure of the front-end module, and the technical issues are explained and in Section 2.3. Then, technologies on antennas, peripheral elements, and architectures of the radars in previous works and their problems to realize the dual-range dual-FOV radars are described and discussed in Sections 2.4 and 2.5. The issues of the front-end module, antennas, and peripheral technologies are summarized in Section 2.6. Finally, an approach and outline of this dissertation are described in Section 2.7.

2.2 Issues on dual-range dual-FOV radars, front-end modules, and antennas

A front-facing dual-range dual-FOV radar equipped on vehicles with the ADAS or AD systems requires to detect objects at distance over 200 m in front of the vehicles and also requires a wide FOV of ±35 degrees or more in MRR-mode as described in Section 1.5.4. The above targets are not only vehicles and trucks which have a large RCS but also pedestrians and falling objects on the road which have lower RCS than vehicles. Moreover, the dual-range dual-FOV radar is typically installed behind

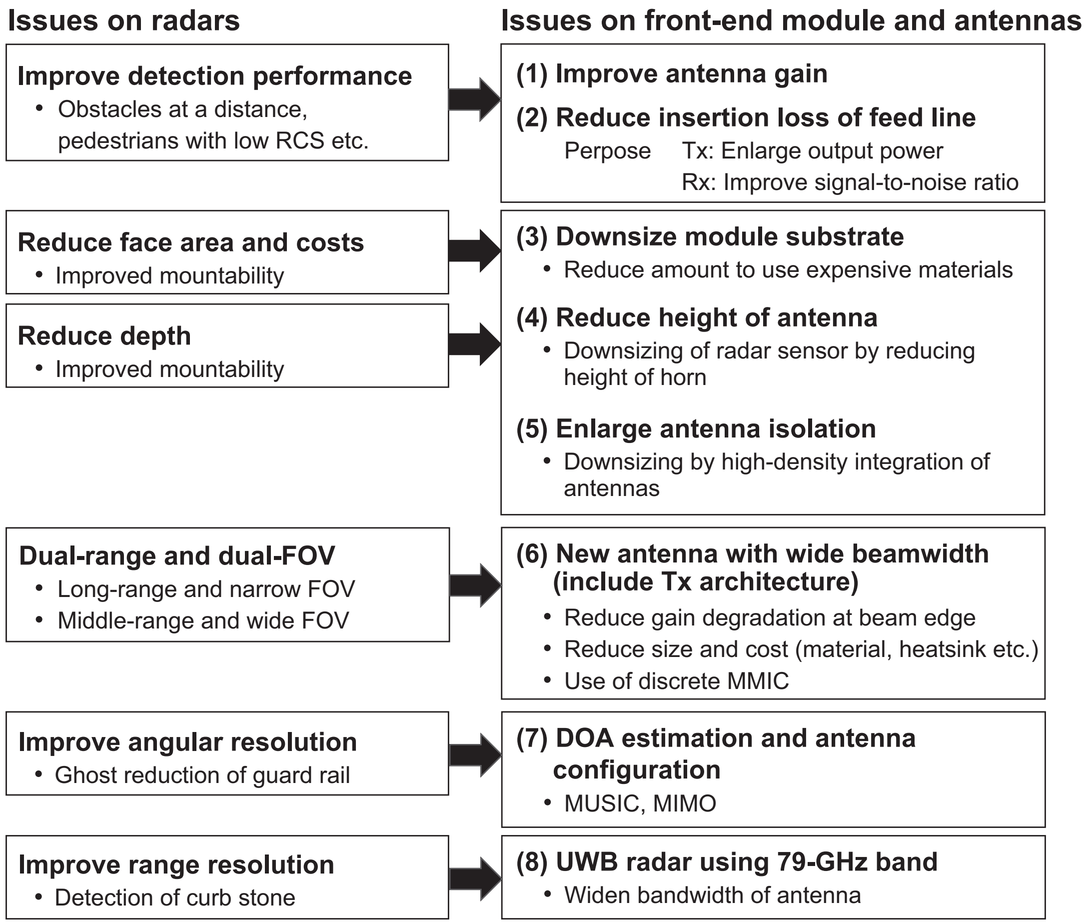

Fig. 2.1. Issues on dual-range dual-FOV radar, front-end module, and antennas.

the front bumper, the front grill, or an emblem on the front grill so as not to disturb the vehicle design. Therefore, a small housing especially with a small face area are required for the dual-range dual-FOV radar. In addition to the small face, a small depth is also required to install the dual-range dual-FOV radar to compact cars. Another consideration is the cost of materials and fabrication, which is an important issue in mass production.

To meet these requirements, it is important to achieve a high antenna gain, low feed-line loss, and high antenna isolation, while downsizing a front-end module composed of antennas and MMICs. Moreover, it is also important to provide a wide beamwidth in a middle-range detection by using the same antenna structure for a long-range detection. Furthermore, higher spatial resolution is expected to the dual-range dual-FOV radar in order to reduce a ghost caused by the reflected signal from guard rails as a multipath signal [2.1] and recognize a drivable area by detecting curb stones [2.2]. The issues on the front-end module and antennas are detailed by using Fig. 2.1.

The left side and right side of Fig. 2.1 show the issues on the dual-range dual-FOV radar and those of the front-end module and antennas in the radar, respectively. To improve detection performance of the radar, it is important to improve an antenna gain because an input power of the Tx antenna is limited to 10 dBm or less as described in Table 1.3. Reduction of insertion loss of feed lines for the antennas is also required to reduce an output power from the Tx MMIC because it is limited due to characteristics of semi-conductor devices (such as break-down voltage) and heat dissipation structure. Regarding Rx, reduction of insertion loss of feed lines for the antennas is also necessary to extend a detection range of the radar, since the minimum receivable power $P_{r\min}$ in the equation (1.6) becomes small as the insertion loss is reduced.

Downsizing of a substrate of the front-end module is required to reduce the face area and costs of the radar because the face area of the current radars for automotive applications mainly depends on the size of the front-end module substrate. In addition, reducing the size of the front-end module substrate and applying a mono-layer substrate with a low dielectric loss tangent ($\tan\delta$) are effective ways to reduce material cost because the substrate requires expensive materials and a special method of production for millimeter-wave applications. Reduction of the height of the antennas is also needed to reduce the depth of the radar. However, reduction of the depth of the radar is less important than the face area since the dual-range dual-FOV radar is usually installed in areas behind the bumper or emblems on the front grill, which have a depth of several centimeters.

To reduce the face area, a high antenna isolation is also required because the face area can be reduced by integrating the Tx and Rx antennas without a gap between output-apertures of the antennas. Since, in the phase-shifted monopulse method, the DOA estimation is done by comparing the phase difference of the received signals of Rx antennas as described in Section 1.5.2, a high isolation between the Rx antennas is required. However, the isolation degrades as shortening the gap of the output-apertures of the Rx antennas.

The dual-range dual-FOV radar requires the wide FOV in the middle-range detection, therefore, new techniques to widen beamwidth of the Tx antenna or new technique to sweep the beam of the antennas are required. To widen the beamwidth, it is necessary to reduce an antenna gain degradation at a large azimuth angle compared with boresight or beam-nose. Reductions of antenna substrate size and cost are also required. In addition, it is important to realize the radar with the antennas by using commercially available MMICs, considering mass production. Moreover, a combinability of the antennas is necessary where the antennas for MRR-mode (middle-range detection and wide FOV) should have the same structure with those of LRR-mode (long-range detection and narrow FOV) considering integration of the antennas into the radar.

In order to improve a spatial resolution of the radar, new technologies for the DOA estimation, such as MUSIC and MIMO (Multi Input Multi Output) [2.3], and using the 79-GHz band are required.

In this study, I focused on the issues (1) to (6) shown in Fig. 2.1 which relate to technologies for the structure or configuration of the front-end module and antennas. In the next three sections, I will introduce technologies reported in previous works and discuss their problems. First, I describe structures of front-end modules and propose a preferable structure. Next, technologies and issues on antennas and peripheral elements in previous works to improve an antenna gain and isolation are explained. Then, technologies and issues to widen FOV are introduced. Finally, the key points of the technologies and issues are summarized.

2.3 Structures of front-end modules and their issues

First, a preferable structure of a front-end module for a dual-range dual-FOV radar is discussed in this section, considering following two aspects: reduction of an insertion loss of feed line and reduction of material cost.

Two structures for integrating the antenna and MMICs in a millimeter-wave radar are illustrated in Fig. 2.2. In the conventional structure (hereafter structure (a)), the antenna and MMICs are mounted on opposite sides of the substrate [2.4] and are connected with quasi-coaxial in the substrates and coaxial or waveguides in the base plate. In the structure with a mono-layer substrate with a low $\tan\delta$ and a low-cost FR-4 substrate (hereafter structure (b)), which was recently developed, the antenna and MMICs are integrated on the same surface [1.28] and are connected with a microstrip line. Structure (a) has a benefit of independent modification and a wide selection of materials for the antennas and radio frequency (RF) circuits because they are integrated on different substrates. In addition, using structure (a) reduces the size of the front-end module substrate because the MMICs are mounted on opposite sides of the antennas. However, structure (a) requires a transitions between microstrip line and the quasi-coaxial whose insertion loss is 2 dB [2.4] adding to transmission lines such as a microstrip line in order to connect the MMICs and antennas. A transition between a microstrip line and waveguide with an insertion loss of 0.4 dB was also reported [2.5] in order to connect microstrip lines integrated on the opposite surfaces each other by using a waveguide instead of the quasi-coaxial. Structure (a) requires two transitions integrated on each surface, therefore, total insertion loss of the transition becomes 4 or 0.8 dB by using the quasi-coaxial or waveguide, respectively. Contrary to structure (a), the MMICs and antennas can be connected by only using the microstrip line in structure (b) because the MMICs and antennas are integrated on the same surface of

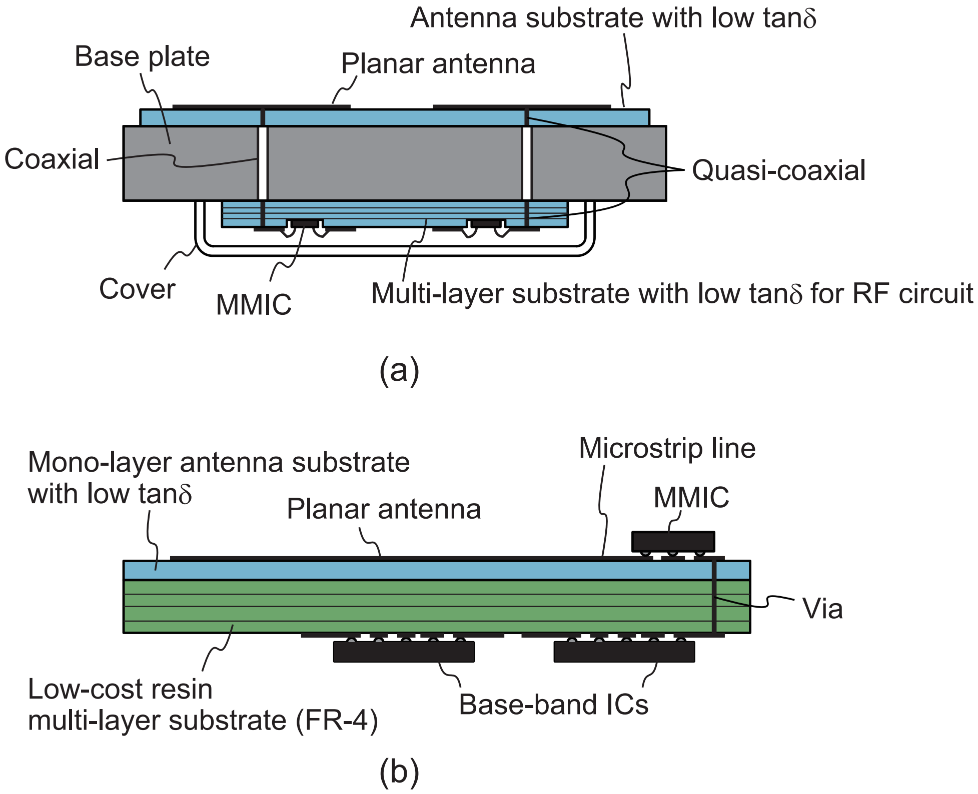

Fig. 2.2. Integration of antenna and MMICs for automotive radars: (a) conventional structure; (b) structure with mono-layer front-end module substrate and low-cost resin substrate.

the substrate. Therefore, the insertion loss of the feed line can be reduced by using structure (b). In addition, structure (b) has higher robustness against production deviations such as frequency shift due to an etching error of the metallic patterns in the substrate because degradation of the insertion loss caused by the etching error for the microstrip line is smaller than the transitions.

Moreover, applying a mono-layer substrate with a low $\tan\delta$ is effective way to reduce costs of the front-end module because a substrate with a low $\tan\delta$ has higher material and manufacturing costs than common resin substrates such as FR-4 substrates. However, structure (a) requires multi-layer substrate with the low $\tan\delta$ for RF circuit substrate to reduce the insertion loss of the quasi-coaxial or post-wall waveguides. The amount of material to build up multi-layer substrate increases as increasing the number of layers. Therefore, the material cost of structure (a) becomes higher than that of structure (b) even if the mounting areas of each structure are the same. Furthermore, structure (b) can integrate back-end circuits which mainly consist of signal processors and power supplies on the bottom side of the FR-4 substrate, whereas additional substrate is required in structure (a). Therefore, structure (b) can reduce total costs of the substrates for the front-end module and back-end circuits in the dual-range dual-FOV radar.

In short, structure (b) is better than structure (a) with respect to the insertion loss, robustness against production deviations, and material cost. However, the antenna substrate in structure (b) is larger than that in structure (a). Thus, an antenna structure based on structure (b) with small antenna substrate is required, while keeping a high antenna gain.

2.4 Antennas, peripheral technologies, and their issues

Next, previous works on antennas and peripheral technologies for millimeter-wave applications and their issues are described and discussed in this section. First, I describe antenna technologies to improve an antenna gain and peripheral technologies about feeding elements. Next, technologies to achieve a high antenna isolation are explained.

2.4.1 Array antennas fed by post-wall waveguides

Various antenna structures have been investigated for radars in automotive applications. Structures with post-wall waveguides as their feed elements provide a high antenna gain due to the reduced insertion loss of the feed elements [2.6–2.8], where slot, patch array, or cavity resonator are used as their radiation elements. Main performances of the reported antennas are listed in Table 2.1.

A pair-slot array antenna with a post-wall waveguide for automotive applications was reported [2.6], which consisted of four sub-arrays in which 19 pair-slot were fed by using the post-wall waveguide integrated in an antenna substrate. PTFE (Poly Tetra Fluoro Ethylene) was used as the material of the substrate. The measured insertion loss of the post-wall waveguide was 0.20 dB/cm. The antenna had an antenna gain of 24.4 dBi and aperture efficiency of 67% at 76.5 GHz where the aperture size was 55 × 9.2 mm.

A microstrip patch array antenna with a post-wall waveguide as a feed line using a low temperature co-fired ceramics (LTCC) substrate was reported [2.7]. The measured results of the antenna showed that an antenna gain was 13 dBi and a half-power beamwidth (HPBW) was 7 degrees or less in E-plane at 77 to 81 GHz. The antenna consisted of 12 layers of ceramic tapes and had the size of 28.3 × 1.2 mm.

Bauer et al. [2.8] presented a planar array antenna for LRRs, which used a ceramic-filled cavity resonator and a post-wall waveguide in an LTCC. The antenna provided an antenna gain of 13.2 dBi, efficiency of 65%, and HPBWs of 13 and 100 degrees in E- and H-planes, respectively, at 79 GHz. The fabricated antenna was fed by using

Table 2.1. Main performances of array antennas fed by post-wall waveguides in previous works.

Item		[2.6]	[2.7]	[2.8]
Radiation element		Pair-slot array	Microstrip patch array	Cavity resonator
Frequency band		77 GHz	79 GHz	79 GHz
Antenna gain		24.4 dBi	13 dBi	13.2 dBi
Aperture efficiency		67%	N.A.	65%
HPBW	E-plane	N.A.	$\leq 7^\circ$	13°
	H-plane	N.A.	N.A.	100°
Aperture size		55 × 9.2 mm	28.3 × 1.2 mm	N.A.
Antenna substrate size		55 × 9.2 mm	28.3 × 1.2 mm	N.A.
Substrate material		PTFE	LTCC	LTCC
Results		Measurement	Measurement	Measurement

WR-12 waveguide from the backside of the substrate.

However, the above antennas cannot be applied to a front-end module with a mono-layer substrate but can be adapted to that in which the antenna and MMICs are integrated on opposite sides of the substrate due to their feed structures. A transition to connect a microstrip line and post-wall waveguide was reported [2.9], which can be used a configuration that has the MMICs and antennas on the same surface of the front-end module substrate. However, the transition requires at least two layers in the substrate which consist of a material with a low $\tan\delta$. Thus, the transition can not be applied to structure (b) with the mono-layer substrate.

According to the above discussion, the above antenna structures using post-wall waveguides as their feed elements cannot be applied to a front-end module with the mono-layer substrate, although the antennas have a high antenna gain and aperture efficiency. Thereby, an antenna structure is required, which can be realized by using the mono-layer substrate as well as can provide a high antenna gain.

2.4.2 Microstrip array antennas

Antenna structures with a mono-layer substrate which consisted of a low $\tan\delta$ have been reported. A series-fed microstrip patch array antenna [2.10–2.12] and comb-line antenna [2.13–2.15] are commonly used in current radars for automotive applications. Main performances of the reported antennas are listed in Table 2.2.

A series-fed microstrip patch array antenna for automotive LRRs was reported

Table 2.2. Main performances of microstrip array antennas in previous works.

Item		[2.12]	[2.13]		
Antenna type		Series-fed	Series-fed		Comb-line
Frequency band		77 GHz	77 GHz		77 GHz
Antenna gain		22.3 dBi	$\sim$20 dBi	$\sim$30 dBi	22.5 dBi
Aperture efficiency		19.4%	$\sim$40%	$\sim$30%	53%
HPBW	H-plane	10°	N.A.		4.0°
	E-plane	5.6°	N.A.		26.3°
Aperture size		47 × 19 mm	N.A.		58.5 × 7 mm
Antenna substrate size		47 × 19 mm	N.A.		58.5 × 7 mm
Substrate	e_r	3.2	N.A.		2.2
	$\tan\delta$	0.004	N.A.		0.001
Results		Measurement	Estimation	Estimation	Measurement

[2.12], which consisted of 8 sub-arrays where each sub-array had 20 radiation elements. Rogers RO3003 was applied to the antenna substrate whose dielectric constant e_r and $\tan\delta$ were 3.2 and 0.004, respectively. The fabricated antenna had an antenna gain of 22.3 dBi, aperture efficiency of 19.4%, and HPBWs of 5.6 and 10 degrees in E- and H-planes, respectively, at 76.5 GHz. The aperture size of the antenna was 47 × 19 mm. Iizuka et al. estimated an available aperture efficiency of the series-fed microstrip patch array antennas [2.13] that the efficiencies of about 40% and 30% would be obtained when the targeted antenna gains were around 20 and 30 dBi, respectively, using the 77-GHz band. The efficiency regrades as the targeted antenna gain increases due to increasing of insertion losses of transmission lines, bend, and dividers.

A comb-line antenna for automotive radars using a substrate with a dielectric constant of 2.2 and $\tan\delta$ of 0.001 was reported [2.13], which consisted of two linear arrays with 37 radiating elements per one array. The antenna had an antenna gain of 22.5 dBi and aperture efficiency of 53% at 76.5 GHz. HPBWs were 4.0 and 26.3 degrees in H- and E-planes, respectively. The aperture size was 58.5 × 7 mm. The comb-line antenna provided a high antenna gain and aperture efficiency. However, the gain of the comb-line antenna is roughly in proportion to its aperture size, therefore, the area of the antenna substrate must be increased in order to increase the antenna gain to the level required. Moreover, an additional area to mount MMICs is required when the planar antennas are used in the front-end module structure (b) described in the previous section. Therefore, a new antenna structure is required to reduce the substrate area considering an integration of the antennas and MMICs.

Table 2.3. Main performances of antennas with dielectric lens in previous works.

Item		[2.16]	[2.17]	[2.18]
Antenna type		MSA array and cylindrical lens	Two MSAs and parabolic lens	Flat lens and horn
Feed element		Microstrip line	Microstrip line	Waveguide
Frequency band		77 GHz	77 GHz	71 to 76 GHz
Antenna gain		MSA array +1.5 dB	20.2 dBi	28.9 dBi
Aperture efficiency		N.A.	N.A.	60%
HPBW	H-plane	$\sim$20°	9°	N.A.
	E-plane	4.5°	N.A.	N.A.
Aperture size		40 × 89.7 mm	875 mm^2	42 × 42 mm
Antenna substrate size		40 × 89.7 mm	25 × 44.5 mm	—
Antenna height		N.A.	17.66 mm	37 mm
Substrate	e_r	N.A.	2.6	—
	$\tan\delta$	N.A.	N.A.	—
Lens material		N.A.	N.A.	N.A.
Results		Measurement	Measurement	Simulation

2.4.3 Antennas with dielectric lens

Antenna structures with microstrip antennas (MSAs) and dielectric lens that increase the gain compared with that of the series-fed microstrip patch array antenna have been reported [2.16, 2.17]. Other antenna structures with lens have also been investigated [2.18]. Main performances of the reported antennas are listed in Table 2.3.

Wenig et al. [2.16] presented an antenna for automotive radars with a cylindrical lens and microstrip patch array. The diameter and length of the lens were 40 mm and $23\lambda_0$ (corresponding to 89.7 mm at 76.5 GHz), respectively. The antenna provided 1.5 dB higher antenna gain than that the series-fed microstrip patch array antenna with two sub-arrays where each sub-array consisted of 16 radiation elements at 76.5 GHz. A -1.5 dB-beamwidth was 4.5 degrees in E-plane and that in H-plane was around 20 degrees (the value was not specified). The antenna could improve the antenna gain; however, substrate required an area at least the same size as the output-aperture area of the lens (40 × 89.7 mm) to arrange a Tx and Rx antennas. The large size of the antenna substrate is a problem of the antenna.

A dielectric lens antenna feeding with two MSAs for LRRs was reported [2.17]. The antenna had a peak antenna gain of 20.2 dBi and an HPBW of 9 degrees in H-plane in the 77-GHz band. Rogers RT/Duroid 5880 with a dielectric constant of 2.6 was used as the material of the antenna substrate and a dielectric material with the dielectric constant of 3 was used for the lens. The diameter and height of the lens were 35 and 17.66 mm, respectively, and the substrate size was 25 × 44.5 mm. Although the antenna has potential to reduce the size of antenna substrate because it consists of two MSAs, the antenna has following problems: 1) the antenna requires large antenna substrate to arrange a Tx and Rx antennas and 2) the radiation pattern will regrade if the lenses for the Tx and Rx antennas are overlapped in order to reduce the substrate size.

Another type of antenna with a pyramidal horn and flat lens was reported [2.18] for 71 to 76 GHz band. The lens consisted of two dimensional periodic unit cells of $\lambda/2$ periodicity and a phase correction of each unit cell were changed with respect to the position of the unit cell in the lens. The height of the horn was 37 mm. The antenna had a simulated gain of 28.9 dB and aperture efficiency of 60% at 72.5 GHz, where the output-aperture size of the horn was 42 × 42 mm. The aperture efficiency is higher than that of the comb-line antenna described in Section 2.4.2. However, the antenna requires an additional horn-to-microstrip transition in order for it to be applied to a mono-layer antenna substrate. Moreover, the structure of the lens is difficult to be applied to mass production of automotive radars due to its complicated structure.

The key points of the above three types of antennas described in Sections 2.4.1 to 2.4.3 are as follows: Structures with a slot or microstrip array antenna with a post-wall waveguide as their feed elements provide a high antenna gain due to the reduced insertion loss of the feed elements; however, they cannot be applied to structure (b).

Contrary to the above antennas with waveguide feedings, the series-fed microstrip patch array and comb-line antennas can be applied to structure (b). The comb-line antenna with a high antenna gain and high aperture efficiency. However, the antenna substrate becomes large due to the large aperture size of the antenna and an additional area to mount MMICs, therefore, the material cost is still high.

To attain a high antenna gain, antennas with dielectric lens have been reported. The antennas can also use structure (b); however, the antennas require a large antenna substate when the antennas are arranged for a Tx and Rx in radars. Moreover, the antenna with lens and horn provides a high antenna gain and aperture efficiency. However, the reported lens horn antenna can be applied to structure (a) because it was fed by a waveguide. Therefore, a transition between horn and microstrip line is necessary to apply the lens horn antenna to a front-end module with structure (b).

2.4.4 Horn-to-microstrip transition

To connect a lens horn antenna to a microstrip line, the author referred to the transitions between the horn and microstrip line. Several transitions between a rectangular waveguide and microstrip line have been reported, which applied a patch antenna type [2.5, 2.19], probe fed type [2.20], and slot coupled type [2.21] structures. However, these transitions connect the microstrip line to a rectangular waveguide integrated on the opposite side of the substrate each other.

Topak et al. [2.22] presented a transition in which the waveguide was mounted on the same side as the microstrip line by using a coplanar patch antenna. However, the transition requires a narrow gap of 60 μm between the feed line and ground pattern, so it is hard to apply this transition to low-cost LRRs given the possible occurrence of etching errors and transition misalignments during mass production.

Furthermore, designs for transitions with a high tolerance to problems such as misalignment of the horn and antenna substrate due to mechanical deviation during production have yet to be reported to the best of the author's knowledge. Misalignment in a structure in which a microstrip line and rectangular waveguide were integrated into opposite sides of the substrate has been investigated [2.5]. However, the optimum structure for the transition for the horn to attain a high tolerance to misalignment differs from that for a rectangular waveguide. Therefore, a new design method is also required.

2.4.5 Antenna isolation

An antenna isolation is important for reducing the sizes of a substrate and projected area of a front-end module while keeping the accuracy of DOA estimation in the phase-shifted monopulse method [1.33] described in Section 1.5.2. Here, the projected area is the area of the module seen from the boresight, which should be small to make the face of radars small. The required antenna isolations from Tx to Rx and from Rx to Rx are greater than 40 and 20 dB, respectively, for FMCW radars [2.23].

While a few technologies have been reported for Tx-Rx antenna isolation for microstrip array antennas in millimeter-wave applications [2.24, 2.25], the isolation of lens horn antennas has yet to be reported to the best of the author's knowledge. Therefore, investigation of lens horn antenna isolation is required to achieve high-density integration of antennas arranged side-by-side without gap for a front-end module with a small substrate and small projected area.

2.5 Technologies to widen FOV and their issues

Digital beamforming (DBF) is well-known as a technology to widen FOV and extend detection range of systems such as radars and communication systems, which were applied to Rx of the systems [2.26, 2.27]. However, it is hard to extend the detection range at the edge of the FOV by using only DBF if the number of Rx channels is limited in order to reduce costs (in particular, MMICs for Rx) of automotive radars using the 77-GHz band.

Fig. 2.3 shows an example of a comb-line antenna array for an Rx with four channels using Rogers RO3003 with a dielectric constant of 3.2 as an antenna substrate and the 77-GHz band. The length of radiation elements is about $\lambda_g/2$ where λ_g is a wavelength on the microstrip line ($\lambda_g \simeq \lambda_0/\sqrt{e_r}$), and the radiation elements are arranged with space of about $\lambda_g/2$. Since the distance between each channel is designed $\lambda_0/2$ to avoid grating lobes within an angle of ±90 degrees in xz-plane, one array of antenna is assigned to each channel. Therefore, an antenna gain of one channel becomes small, so that it is necessary to increase the number of Rx channels to provide a high antenna gain for Rx.

According to the discussion, a new technology to enlarge both FOV and antenna gain by improving Tx is required. In this section, previous works on technologies on Tx for millimeter-wave applications to widen FOV and their issues are introduced and discussed.

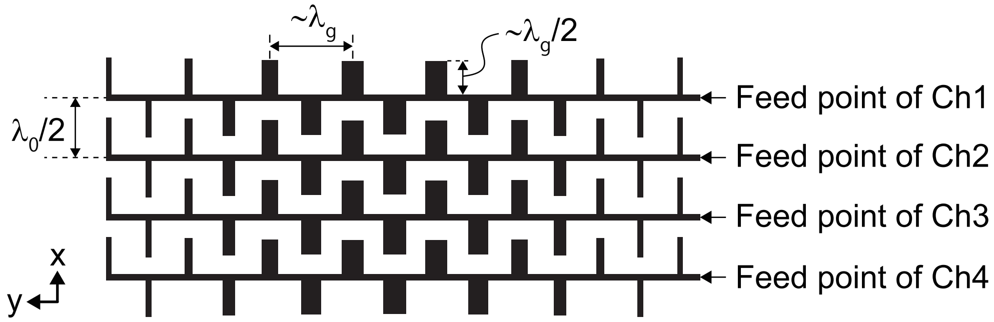

Fig. 2.3. Example of comb-line antenna array layout for Rx with four channels using 77-GHz band.

2.5.1 Transmitter antenna switching

A technology was reported [1.38] that combined DBF with a phased-array Rx and switching two Tx antennas for a long-range and short-range detections where the system was operated in the 24-GHz band. A series-fed microstrip patch array antenna was applied to the Tx antennas. The Tx antennas provide 18 dBi gain at boresight to achieve a detection range of 150 m for the narrow beam. As for the wide beam, an HPBW was ±40 degrees, and the gain at angles of ±40 degrees were 12 dBi to attain the detection range of 60 m. The result for an antenna gain reduction between boresight and azimuth angle of 40 degrees meets the specification of Tx antennas for dual-range dual-FOV radars shown in Fig. 1.12. However, the size of antenna substrate is problematic as described in Section 2.4.2 even if the antenna gain reduction between boresight and the angle of ±40 degrees is kept while enlarging antenna gain by 3 dB and using the 77-GHz band.

2.5.2 Beam scanning

Technologies to widen FOV by scanning a Tx beam by changing the position of radiation sources electrically or mechanically have been investigated [2.28–2.30] for automotive radars or wireless communications.

A technology was reported that sweeps the presented Tx beam by electrically switching among four Tx antennas composed of MSAs arranged in the direction which corresponds to azimuth below a dielectric lens with a parabolic shape for automotive LRRs [2.28]. However, the HPBW in the overlapping radiation patterns was ± several degrees in azimuth, and antenna gains at angles of ±35 degrees were not discussed.

Beam scanning technologies by using a flat lens based on a plate inhomogeneous Luneburg lens were reported for millimeter-wave communication and radar systems. Imbert et al. [2.29] reported simulation results for a beam steering capability in which an antenna gain reduction from boresight at a steering angle of ±35 degrees was -2.8 dB at 75 GHz by moving the position of a radiation source. The performance meets the specification of radiation pattern for MRR-mode of the dual-range dual-FOV radar shown in Fig. 1.12. Lafond et al. [2.30] presented an antenna which had a beam steering capability from -55 to 35 degrees at 62 GHz by switching several radiation sources. The antenna gain reduction at the edge of the scanning angle compared with the gain at boresight was not specified in the report. Although the technologies have a large steering angle with the antenna gain reduction of few dB, the plate inhomogeneous Luneburg lenses are hard to apply to mass production of automotive radars due to production costs.

2.5.3 Transmitter beamforming

Technologies for Tx beamforming to widen FOV have been reported, which used a hybrid beamformer with analog and digital phase shifters or an analog beamformer with analog phase shifters.

A hybrid beamforming technology using analog beamformers, digital beamformers, and phased array antenna with 16 elements was reported for millimeter-wave wireless communication systems [2.31]. The beamformers were integrated on 60-GHz CMOS (Complementary Metal Oxide Semiconductor). The technology had a beam steering angle of around -17 and around 25 degrees, where an HPBW of the beam was several degrees (the value was not specified). However, a gain reduction at the beam steering edge from boresight was not discussed in the report.

An analog beamforming using modulator has been reported for radars using the 77-GHz band. Wanger et al. [2.32] presented a 77-GHz phased-array radar Tx with IQ modulators integrated on an MMIC using SiGe HBT (Hetero-junction Bipolar Transistor) technology and with four array antennas. The IQ modulators acted as analog phase shifters by controlling their IF (Intermediate Frequency) input signals. However, a steered angle of the main beam was -5 degrees and the antenna gain degradation was not discussed. Since the antenna gain at the steering angle of -30 degrees was about 12 dB smaller than that at -5 degrees (corresponds to beam center) by consulting the reported result, the result does not meet the specification of radiation performance of the Tx antenna shown in Fig. 1.12.

Other technologies on analog phase shifters using MEMS (Micro Electro Mechanical Systems) have been reported in millimeter-wave applications, which have not discussed a radiation performance of Tx antennas. McFeetors et al. [2.33] reported an analog phase shifter which had phase shifts of 170°/dB at 40 GHz and 150°/dB at 30 GHz. Chicherin et al. [2.34] presented another analog phase shifter which provided differential analog phase shift from 0 to up to 240 degrees and had an insertion loss of 0.7 to 3.5 dB at 83.4 GHz. For example, in the ideal array antenna with three point radiation sources separated by half wave-length, a phase shift of about 34 degrees is required to tilt the direction of the beam by 35 degrees in azimuth. Thus, the analog phase shifter in the antenna array may have the insertion loss of about 1 dB at the 77-GHz band to provide a steering angle of ± 35 degrees. Because of the large insertion loss of the phase shifters, pre-amplifiers are required to insert between Tx MMICs and Tx antennas to keep a high EIRP. A power consumption of the Tx increases due to introducing the additional pre-amplifiers. Since an additional heat dissipation structure such as large heat sink is required in order to dissipate the heat generated by the Tx circuits, a large size of a radar housing become a problem in automotive applications.

Furthermore, a demonstration using analog beamforming for automotive radars using the 77-GHz band was done by the Metawave Corporation [2.35], which applied an analog phase shifter comprising a metamaterial. However, there is no production with respect to an analog phase shifter which is commercially available to the best of the author’s knowledge at the time of writing.

Table 2.4. Main performances of technologies to widen FOV in previous works.

Item	[1.38]	[2.28]	[2.29]
Technology	Tx Antenna switching and Rx DBF	Tx electrical switching	Tx mechanical scanning
Antenna type	MSA array	Parabolic lens	Luneburg lens
Radiation element	MSA	MSAs	Waveguide
Frequency band	24 GHz	77 GHz	75 GHz
Steering angle	±40°	± several degrees	±45°
Antenna gain reduction	-6 dB	N.A.	-2.8 dB at ±35°
Results	Measurement	Measurement	Simulation

Item	[2.30]	[2.31]	[2.32]
Technology	Tx electrical switching	Tx hybrid beamforming	Tx analog beamforming w/ IQ modulator
Antenna type	Luneburg lens	MSA array	MSA array
Radiation element	Waveguides	MSA	MSA
Frequency band	62 GHz	60 GHz	77 GHz
Steering angle	-55 to 35°	-17 to 25°	-5°
Antenna gain reduction	N.A.	N.A.	N.A.
Results	Measurement	Measurement	Measurement

In short, the Tx beamforming with modulators cannot attain both wide FOV and high antenna gain at the edge of the FOV where the required FOV of ±35 degrees and the antenna gain reduction of -3 dB at azimuth angle of ±35 degrees compared with the antenna gain at boresight. Contrary to the Tx beamforming with modulators, that with analog beam shifters which consist of a MEMS or metamaterial may be a candidate. However, an additional heat dissipation structure to cool the Tx circuits with pre-amplifiers and analog phase shifters is problematic in the size of the radar housings. Therefore, the Tx beamforming is hard to apply to current research and development on the dual-range dual-FOV radar.

Table 2.4 summarizes main performances of technologies to widen FOV in the previous works described in Sections 2.5.1 to 2.5.2. Technologies to widen FOV by improving Tx circuits and antennas such as Tx antenna switching, beam scanning with lens antennas, and Tx beamforming using beamformers have been reported. The technologies for Tx antenna switching [1.38] and beam scanning [2.29] have possibility to be a candidate of a Tx for dual-range dual-FOV radars. However, the above technologies still have the following issues: MSA arrays used in the Tx antenna switching require large antenna substrate which consists of a material with a low $\tan\delta$ to enlarge an antenna gain, and material costs become high as a result. Since the Luneburg lens used in the beam scanning have complicated structure, production costs will be an issue to apply it to automotive radars with low cost. Therefore, a new technology to wide FOV while keeping a high antenna gain at the edge of FOV for the dual-range dual-FOV radar is required. Moreover, it is also important to reduce the amount of expensive materials for the antennas such as a resin substrate with a low $\tan\delta$ and to apply simple structure of antennas for cost reduction.

2.6 Summary of issues on front-end module, antennas, and peripheral technologies

In this section, the discussions on previous works and their issues with respect to front-end modules, antennas, and peripheral technologies described in Sections 2.3 to 2.5 are summarized.

- A front-end structure which consists of mono-layer substrate with a low $\tan\delta$ to integrate antennas and MMICs on the same surface of the substrate is preferable for dual-range dual-FOV radars, considering reduction of an insertion loss of feed line and material cost. However, the structure requires a large front-end module substrate due to integrating the antennas and MMICs on the same surface of the substrate.

- Various antenna structures have been investigated for radars in automotive applications. Structures with post-wall waveguides as their feed elements and slot or patch arrays as their radiation elements provide a high antenna gain due to the reduced insertion loss of the feed elements. However, they cannot be applied to an antenna module with a mono-layer substrate described above.

- Several antenna structures with a mono-layer substrate with a low $\tan\delta$ have been reported. Although a comb-line antenna has a high aperture efficiency, it requires large substrate size because an antenna gain is roughly in proportion to the aperture size. Therefore, the material cost is still high.

- A lens horn antenna which consists of flat lens and pyramidal horn provides a high antenna efficiency. However, the antenna requires a horn-to-microstrip transition in order to connect the antenna and MMICs. However, such transition has yet to be reported to the best of the author's knowledge. Moreover, the cost of the flat lens is problematic.

- An antenna isolation is important for reducing the sizes of a substrate and projected area of a front-end module while keeping the accuracy of DOA estimation in the phase-shifted monopulse method. While a few technologies have been reported for Tx-Rx antenna coupling for microstrip array antennas in millimeter-wave radar applications, isolation of lens horn antennas has yet to be reported to the best of the author's knowledge, which are the base structure of the proposed antennas in this study.
- Technologies to widen FOV by improving Tx circuits and antennas have been reported, such as Tx antenna switching and beam scanning which satisfied a specification for FOV of the dual-range dual-FOV radars. However, material and production costs are problematic due to a large size of antenna substrate and additional heat dissipation structure and complicated structure of lenses.

Therefore, a new antenna structure is required, which has a small antenna substrate with a mono-layer substrate composed of a low $\tan\delta$ material and can be connected with MMICs by only using microstrip elements, in order to reduce an insertion loss of feed lines and material cost. In addition, the new antenna structure required to provide a high antenna gain, high isolation, and wide beamwidth to achieve the dual-range dual-FOV radar with a small face. Reduction of costs are also required in the newly proposed front-end modules and antennas.

2.7 Approach and outline of this study

In order to solve the above issues to provide the dual-range dual-FOV radar described in Sections 2.3 to 2.6, new antenna structures have been proposed, which consisted of horns, lenses, and horn-to-microstrip transitions [2.12, 2.36–2.40]. In this section, an approach to solve the issues and an outline of this dissertation are described.

2.7.1 Approach in this study

First, a single MSA was chose as a radiation element focusing on both connectivity of antennas to MMICs and downsizing of the antenna substrate which had a mono-layer substrate in order to reduce an insertion loss of feed line and material cost. In particular, I aimed to reduce the size of an antenna substrate smaller than that of whole output-aperture of antennas for Tx and Rx. Next, a lens horn antenna was applied to enlarge an antenna gain at boresight and to provide a flat beam whose beamwidth in

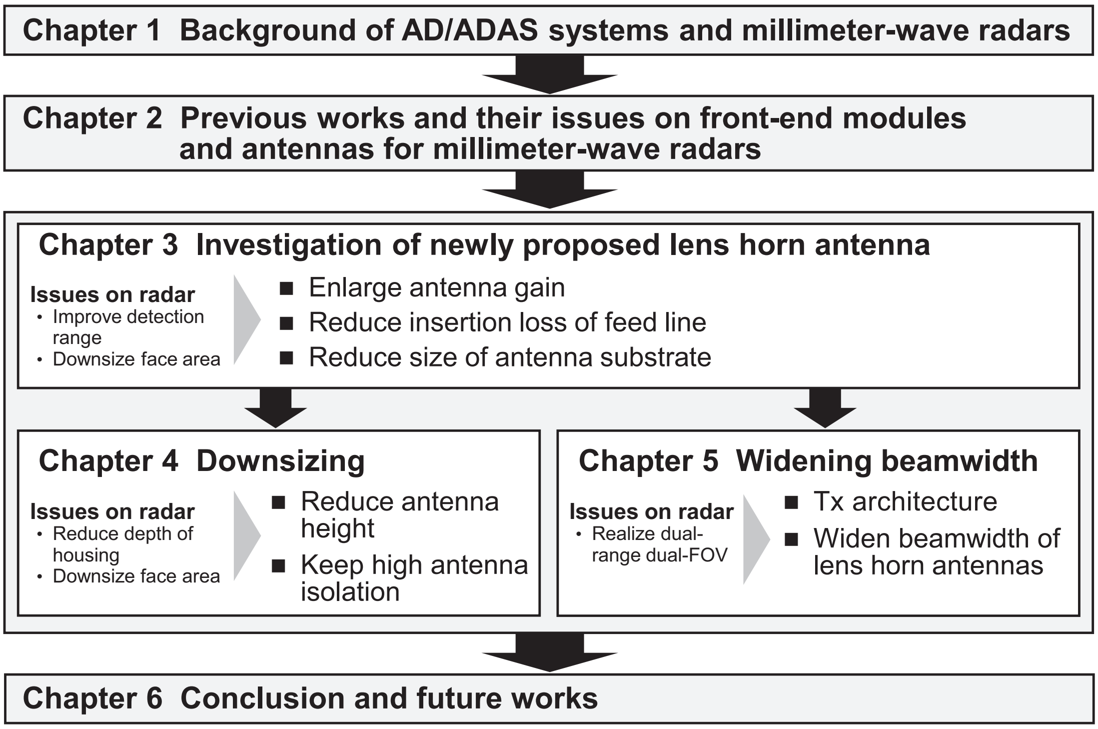

Fig. 2.4. Outline of this dissertation.

azimuth was much wider than that in elevation in order to realize the LRR-mode of the dual-range dual-FOV radar. Then, a technique to widen FOV was investigated for MRR-mode, which can be realized by using the same structure of the antenna for the LRR-mode considering an integration of the antennas on a front-end module.

Moreover, all technologies have been investigated under a policy that all the materials have been already used in current automotive millimeter-wave radars considering productivity and production costs. Furthermore, since the proposed technologies relate to passive elements of a front-end module such as antennas, it is significant that the technologies can be realized by using active devices such as MMICs which are commercially available at the time of writing in order to develop technologies considering mass production. Thus, I investigated a new configuration of the front-end module and architecture of a Tx circuit under a policy that the configuration and architecture could be attained by using such MMICs in this study.

2.7.2 Outline of this dissertation

Fig. 2.4 shows an outline of this dissertation with respect to the issues to be solved in order to achieve the dual-range dual-FOV radar. First, a new antenna structure with lens, horn, and single microstrip antenna is proposed and evaluated to provide a high antenna gain, small insertion loss of its feed line, and small antenna substrate for the

LRR-mode in Chapter 3 as a basic antenna structure proposed in this study. In particular, a design of the new antenna structure comprising a new horn-to-microstrip transition is proposed considering a robustness against deviation in mass production. Next, techniques to reduce the height of the proposed antenna and to increase an antenna isolation are proposed and discussed in order to provide a small face of LRRs in Chapter 4. A newly proposed configuration of a front-end module for a compact LRR is also proposed in Chapter 4 in order to demonstrate that the proposed antennas can attain smaller size of the front-end module substrate (antenna substrate) than the whole output-aperture of Tx and Rx antennas. Then, a new technology to widen beamwidth of antennas based on the lens horn antenna is proposed and evaluated in Chapter 5 in order to support both the LRR- and MRR-modes for a dual-range dual-FOV radar. A new architecture of a Tx circuit of the dual-range dual-FOV radar is also proposed in Chapter 5. Moreover, versatility of the proposed techniques on frequency bands are discussed in each chapter. Finally, the key points of this study and future works are summarized in Chapter 6.

References

[2.1] T. Visentin, J. Hasch, and T. Zwick, “Analysis of multipath and DOA detection using a fully polarimetric automotive radar,” *Int. Journal of Microw. and Wireless Tech.*, vol. 10, issu. 5-6, pp. 570–577, Jun. 2018.

[2.2] A. Ioffe, W. Doerr, H. Yan, D. H. Vu, and A. H. Arage, “RCS Characteristics of Street Curbs and the Applications in Automotive Radar Classification,” in *Proc. of the 13th European Radar Conf.*, pp. 241–244, Oct. 2016.

[2.3] I. Bilik, O. Bialer, S. Villeval, H. Sharifi, K. Kona, M. Pan, D. Persechini, M. Musni, and K. Geary, “Automotive MIMO Radar for Urban Environments,” *IEEE Radar Conf.*, pp. 1–6, May 2016.

[2.4] H. Nagaishi, H. Shinoda, H. Kondoh, and K. Takano, “77 GHz MMIC Transceiver Modules with Thick-Film Multi-Layer Ceramic Substrate for Automotive Radar Applications,” *IEEE Microw. Theory and Tech. Society Int. Dig.*, vol. 3, pp. 1949–1952, Jun. 2003.

[2.5] H. Iizuka, T. Watanabe, K. Sato, and K. Nishikawa, “Millimeter-Wave Microstrip Line to Waveguide Transition Fabricated on a Single Layer Dielectric Substrate,” *IEICE Trans. Commun.*, vol. E85-B, no. 6, pp. 1169–1177, Jun. 2002.

[2.6] T. Shijo, S. Obayashi, and T. Morooka, "Design and development of 77-GHz pair-slot array antenna with single-mode post-wall waveguide for automotive radar," in *Proc. of IEEE Int. Symp. on Antennas and Propag.*, pp.476–479, Jul. 2011.

[2.7] X. Wang and A. Stelzer, "A 79-GHz LTCC Patch Array Antenna Using a Laminated Waveguide-Based Vertical Parallel Feed," *IEEE Antennas and Wireless Propag. Lett.*, vol. 12, pp. 987–990, Aug. 2013.

[2.8] F. Bauer and W. Menzel, "A 79-GHz Planar Antenna Array Using Ceramic-Filled Cavity Resonators in LTCC," *IEEE Antenna and Wireless Propag. Lett.*, vol. 12, pp. 910–913, Jul. 2013.

[2.9] Y. Uemichi, O. Nukaga, K. Nakamura, X. Han, R. Hosono, and N. Guan, "A Study on the Broadband Transitions between Microstrip Line and Post-Wall Waveguide in E-band," in *Proc. of the 46th European Microw. Conf.*, pp. 13–16, Oct. 2016.

[2.10] D. G. Babas and J. N. Sahalos, "Synthesis Method of Series-fed Microstrip Antenna Arrays," *Electronics Lett.*, vol. 43, issu. 2, pp. 78–80, Feb. 2007.

[2.11] T. Yuan, N. Yuan, and L.-W. Li, "A Novel Series-Fed Taper Antenna Array Design," *IEEE Antenna and Wireless Propag. Lett.*, vol. 7, pp. 362–365, Jul. 2008.

[2.12] A. Kuriyama, H. Nagaishi, H. Kuroda, and K. Takano, "A High Efficiency Antenna with Horn and Lens for 77 GHz Automotive Long Range Radar," in *Proc. of the 13th European Radar Conf.*, pp. 378–381, Oct. 2016.

[2.13] H. Iizuka, T. Watanabe, K. Sato, and K. Nishikawa, "Millimeter-Wave Microstrip Array Antenna for Automotive Radars," *IEICE Trans. Commun.*, vol. E86-B, no. 9, pp. 2728–2738, Sep. 2003.

[2.14] K. Sakakibara, S. Sugawa, N. Kikuma, and H. Hirayama, "Millimeter-Wave Microstrip Array Antenna with Matching-Circuit-Integrated Radiating-Elements for Travelling-Wave Excitation," in *Proc. of the Fourth European Conf. on Antennas and Propag.*, pp. 1–5, Apr. 2010.

[2.15] S. Sugawa, K. Sakakibara, N. Kikuma, and H. Hirayama, "Low-Sidelobe Design of Microstrip Comb-Line Antennas Using Stub-Integrated Radiating Elements in the Millimeter-Wave Band," *IEEE Trans. Antennas and Propag.*, vol. 60, no. 10, pp. 4699–4709 Oct. 2012.

[2.16] P. Wenig, R. Weigel, and M. Schneider, “A Dielectric Lens Antenna for Digital Beamforming and Superresolution DOA Estimation in 77 GHz Automotive Radar,” in *Proc. of Int. ITG Workshop on Smart Antennas 2008*, pp. 184–189, Feb. 2008.

[2.17] H.-N. Wang, Y.-T. Huang, and S.-J. Chung, “A Dielectric Lens Antenna Feeding with Microstrip Patch Antennas for 77GHz Long Range Radar Application,” in *Proc. of Asia Pacific Microw. Conf. 2012*, pp. 412–414, Dec. 2012.

[2.18] M. K. T. Al-Nuaimi and W. Hong, “Compact Size High Gain Lens Corrected Pyramidal Horn Antenna for 71-76GHz Band,” in *Proc. of Asia-Pacific Conf. on Antenna and Propag. 2014*, pp. 22–25, Jul. 2014.

[2.19] Y. Mizuno, K. Sakakibara, and N. Kikuma, “Loss Reduction of Microstrip-to-Waveguide Transition Suppressing Leakage from Gap between Substrate and Waveguide by Choke Structure,” in *Proc. of Int. Symp. on Antennas and Propag. 2016*, pp. 374–375, Oct. 2016.

[2.20] Y. C. Shih, T. N. Ton, and L. Q. Bui, “Waveguide-to-Microstrip Transitions for Millimeter-Wave Applications,” *IEEE Microw. Theory and Tech. Society Int. Dig.*, pp. 473–475, May 1988.

[2.21] W. Grabherr, W. G. B. Huder, and W. Menzel, “Microstrip to Waveguide Transition Compatible with MM-Wave Integrated Circuits,” *IEEE Trans. Microw. Theory Tech.*, vol. 42, issu. 9, pp. 1842–1843, Sep. 1994.

[2.22] E. Topak, J. Hasch, and T. Zwick, “Compact Topside Millimeter-Wave Waveguide-to-Microstrip Transitions,” *IEEE Microw. and Wireless Components Lett.*, vol. 23, no. 12, pp. 641–643, Oct. 2013.

[2.23] O. Anegawa, A. Otsuka, T. Kawasaki, K. Tsukashima, M. Kubota, and T. Nakabayashi, “RF Module for High-Resolution Infrastructure Radars,” *SEI Technical Review*, no. 86, pp. 35–40, Apr. 2018.

[2.24] C. Trampuz, I. E. Lager, M. Simeoni, and L. P. Ligthart, “Experimental Characterization of Channel Crosstalk in Interleaved Array Antennas for FMCW Radar,” in *Proc. of the 7th European Radar Conference*, pp. 439–442, Sep. 2010.

[2.25] B. B. Adela, P. T. M. van Zeijl, U. Johannsen, and A. B. Smolders, “On-Chip Antenna Integration for Millimeter-Wave Single-Chip FMCW Radar, Providing High Efficiency and Isolation,” *IEEE Trans. Antennas and Propag.*, vol. 64, no. 8, pp. 3281–3291, Aug. 2016.

[2.26] B.-H. Ku, P. Schmalenberg, O. Inac, O. D. Gurbuz, J. S. Lee, K. Shiozaki, and G. M. Rebeiz, “A 77–81-GHz 16-Element Phased-Array Receiver with 50 Beam Scanning for Advanced Automotive Radars,” *IEEE Trans. Microw. Theory Tech.*, vol. 62, no. 11, pp. 2823–2832, Nov. 2014.

[2.27] S. Tokoro, K. Kuroda, A. Kawakubo, K. Fujita, and H. Fujinami, “Electronically Scanned Millimeter-wave Radar for Pre-Crash Safety and Adaptive Cruise Control System,” in *Proc. of the IEEE Intelligent Vehicles Symp.*, pp. 304–309, Jun. 2003.

[2.28] W. Menzel and A. Moebius, “Antenna Concepts for Millimeter-Wave Automotive Radar Sensors,” in *Proc. of IEEE*, vol. 100, no. 7, pp. 2372–2379, Jul. 2012.

[2.29] M. Imbert, A. Papió, F. D. Flaviis, L. Jofre, and J. Romeu, “Design and Performance Evaluation of a Dielectric Flat Lens for Millimeter-Wave Applications,” in *Proc. of the 8th European Conf. on Antennas and Propag.*, pp. 3193–3196, Apr. 2014.

[2.30] O. Lafond, M. Himdi, H. Merlet, and P. Lebars, “An Active Reconfigurable Antenna at 60 GHz Based on Plate Inhomogeneous Lens and Feeders,” *IEEE Trans. Antennas and Propag.*, vol. 61, no. 4, pp. 2672–2678, Apr. 2013.

[2.31] T. Shimura, T. Ohshima, H. Ashida, S. Ishikawa, S. Fujio, A. Honda, Z. Li, K. Nishikawa, C. Kojima, K. Ozaki, M. Shimizu and Y. Ohashi, “Millimeter-Wave TX Phased Array with Phase Adjusting Function between Transmitters for Hybrid Beamforming with Interleaved Subarrays,” in *Proc. oft the 13th European Radar Conf.*, pp. 425–428, Oct. 2016.

[2.32] C. Wagner, A. Stelzer, and H. Jager, “A Phased-Array Radar Transmitter Based on 77-GHz Cascadable Transceivers,” *IEEE MTT-S Int. Microw. Symp. Dig.*, pp. 73–76, Jun. 2009.

[2.33] G. McFeetors and M. Okoniewski, “Distributed MEMS Analog Phase Shifter With Enhanced Tuning,” *IEEE Microw. and Wireless Components Lett.*, vol. 16, no. 1, pp. 34–36, Jan. 2006.

[2.34] D. Chicherin, M. Sterner, J. Oberhammer, S. Dudorovi, J. Åberg, and A. V. Räisänen, “Analog Type Millimeter Wave Phase Shifters Based on MEMS Tunable High-Impedance Surface in Rectangular Metal Waveguide,” *IEEE MTT-S Int. Microw. Symp. Dig.*, pp. 61–64, May 2010.

[2.35] Metawave Corporation
https://www.metawave.co/spektra

[2.36] A. Kuriyama, H. Nagaishi, and H. Kuroda, "Horn and Lens Antenna with a Small Antenna Substrate and High Production Tolerance for 77-GHz Automotive Long-Range Radar," *IEEJ Trans. Electrical and Electronic Engineering*, vol. 14, issu. 8, pp. 1244–1253, Aug. 2019.

[2.37] A. Kuriyama, H. Nagaishi, H. Kuroda, A. Kitayama, and S. Sasaki, "High Efficiency and Small Antenna with Horn and Lens for 77 GHz Automotive Radar," in *Proc. of the 18th Int. Symp. on Antenna Tech. and Applied Electromagnetics*, pp. 1–2, Aug. 2018.

[2.38] A. Kuriyama, H. Nagaishi, H. Kuroda, and A. Kitayama, "Horn and Lens Antenna with Low Height and Low Antenna Coupling for Compact Automotive 77-GHz Long-Range Radar," *IEICE Trans. Electron.* vol. E103-C, no. 10, pp. 1–8, Oct. 2020.

[2.39] H. Nagaishi, A. Kuriyama, H. Kuroda, and A. Kitayama, "Horn and Prism Antenna for Dual Range and Dual FOV Automotive Radar using 77-GHz Band," in *Proc. of the 18th Int. Symp. on Antenna Tech. and Applied Electromagnetics*, pp. 1–2, Aug. 2018.

[2.40] A. Kuriyama, H. Nagaishi, H. Kuroda, and A. Kitayama, "Horn and Lens Antenna Array with Chevron-Shaped Prism for 77-GHz Automotive Radar with Dual-Range Sensing and a Dual Field of View," *IEEJ Trans. Electrical and Electronic Engineering*, vol. 15, issu. 3, pp. 451–459, Mar. 2020.

Chapter 3

Proposal and Verification of Lens Horn Antenna Fed by Single Microstrip Antenna for Long-Range Radars

3.1 Introduction

In this chapter, a new structure of antenna for automotive long-range millimeter-wave radars is proposed as a basic structure of antennas for a dual-range dual-FOV radars, which can provide both small antenna substrate and high antenna gain.

First, the concept and basic design of an antenna with a horn, lens and single MSA are presented in Sections 3.2 and 3.3, respectively. Next, a robust design of the transition to connect microstrip line and lens horn antenna is proposed in Section 3.4. The simulated radiation performance and loss of the proposed antenna are described and discussed in Section 3.5. Then, the fabricated antenna and the measurement results are described and discussed in Section 3.6. Moreover, versatility of the proposed lens horn antenna is discussed in Section 3.7. Finally, the key points are summarized in Section 3.8.

3.2 Antenna structure with horn, lens, and horn-to-microstrip transition

To achieve a high antenna gain and reduce antenna costs, a new antenna structure with a pyramidal horn, dielectric lens, and single MSA has been investigated. Fig. 3.1 illustrates the structure: (a) shows a perspective view, and (b) shows cross-sectional views considering its integration with the MMICs. D_o and W_o are the output-aperture lengths of the horn in the Y and X directions, respectively. The coordinates of X and Y are shown in Fig. 3.1(a). D_i and W_i are the input-aperture lengths of the horn, and H is the height of the horn. L_s and W_s are the length and width of the antenna substrate, respectively.

Use of the single MSA, which works as a matching element of the transition between the horn and the microstrip line, by the proposed antenna provides the following effects: (1) the antenna gain is improved because the antenna has a shorter feed line than array antennas, (2) the antenna can be connected to the ICs by using the microstrip elements due to its feed structure, (3) the size of the antenna substrate is reduced compared to that in array antennas due to the reduction in the number of MSAs to one, and (4) the face size of the LRR is downsized by three-dimensional integration in which the MMICs are mounted behind a tapered part of the pyramidal horn, as shown on the right in Fig. 3.1(b).

Aluminum and poly-phenylene sulfide (PPS) were used as the material of the horn and lens, respectively. Aluminum and PPS are commonly used as the materials for the frames and radomes of radars, respectively. The horn and lens can be integrated into existing frame and radome, respectively. Thus, additional material costs for the horn and lens are negligibly small in the proposed antenna.

3.3 Design for low-height horn with lens antenna

A design method for the pyramidal horn with dielectric lens is explained in this section. The size of the output aperture of the horn is roughly derived using

$$\mathrm{HPBW} \simeq \frac{70\lambda_0}{D_A}, \tag{3.1}$$

where D_A and λ_0 are the aperture length of the antenna and wavelength in free space, respectively. In particular, to achieve HPBWs of 5 degrees in elevation and 15 degrees in azimuth, this equation indicates that the size of the output aperture (D_o and W_o) of the pyramidal horn should be 45 and 18 mm in the Y and X directions, respectively. The optimal input-aperture size of the horn, $D_i \times W_i$, is 2 × 4 mm to match the impedance of the input-aperture of the horn to that of the leading radiating edge of an MSA detailed in the next section.

The shape of the lens in the Y direction is described by the following equation [3.1], where D, L_F, and e_r are the diameter, focus distance, and dielectric constant of

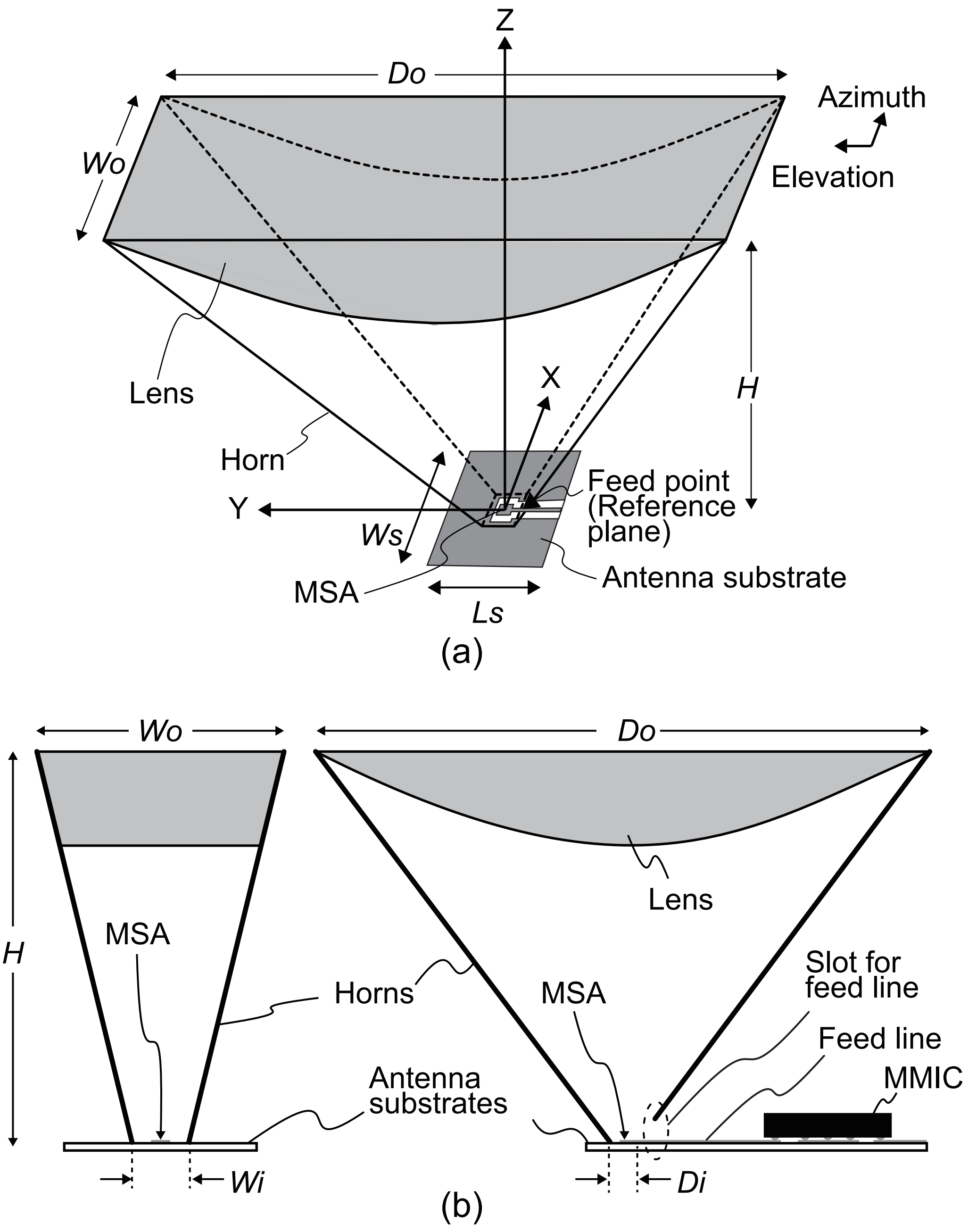

(a)

(b)

Fig. 3.1. Structure of lens horn antenna with single MSA on antenna substrate: (a) perspective view; (b) cross sections in X and Y directions, respectively.

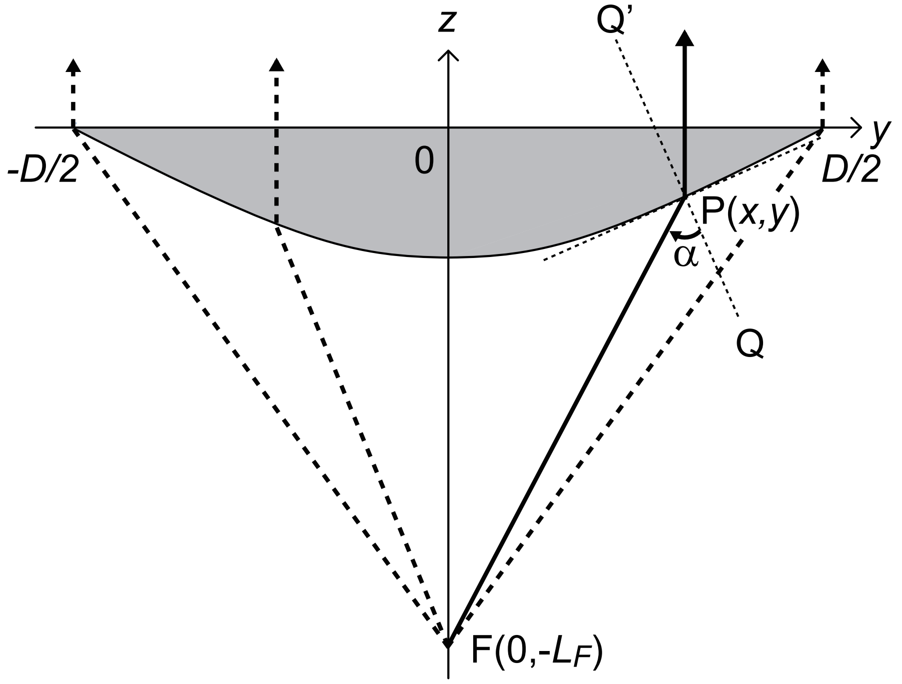

Fig. 3.2. Structure of lens to change wave shape from spherical to plane. Dotted line Q–Q' indicates normal line on surface of lens at point P.

the lens, respectively;

$$\begin{cases} z = \dfrac{-B + \sqrt{B^2 - A\left(D^2/4 - y^2\right)}}{A} \\ A = e_r - 1 \\ B = \sqrt{e_r\left(D^2/4 + L_F^2\right)} - L_F \ , \end{cases} \tag{3.2}$$

The y and z coordinates are shown in Fig. 3.2.

Technologies on lens with matched layer and antireflective coatings have been reported to enhance directivity of lens antennas. A lens antenna with matched layers was reported [3.2], which consist of square-lattice dielectric slabs designed on both surfaces of the lens. The size of the square-lattice dielectric slab was 2.5 × 1.9 × 0.95 mm (width × length × depth), which was optimized to a design frequency of 60 GHz. The fabricated antenna with the matched layers provided a higher directivity by 0.7 dB at 60 GHz than that without the layers. Another lens antenna with an antireflective coatings was proposed [3.3] to reduce reflection loss on beam scanning, which consist of three layers with different dielectric constant (5.35, 3, and 1.75). Simulated results showed that the lens antenna with the antireflective coatings improved an antenna gain of 3 dB at 77 GHz. Although the above technologies improve the directivity or antenna gain of lens antennas, their structures require additional materials and production process which needs highly-accurate thickness control of the matched layers. As a result, material and production costs increase. Moreover, the performance of the matched layer with small lattice integrated on the output surface of a lens may changed by foreign materials when the lens is integrated in a radome of an automotive radar. Thereby, I applied a lens with smooth faces on both input and output sides.

The height of a pyramidal horn with a lens antenna depends on the focus distance of the dielectric lens because the focus distance is much shorter than the height of an optimum horn [3.1]. Therefore, shortening the focus distance of the lens is an effective way to reduce the height of the horn with a lens antenna. However, the curvature of the lens increase as the focus distance is shortened, resulting in degradation of the lens transmittance. Transmittance T_s at the edge of the lens is calculated using the following Fresnel equation (3.3) [3.4].

$$T_s = \left| \frac{2\sqrt{e_r}\cos\alpha}{e_r\cos\alpha + \sqrt{e_r - \sin^2\alpha}} \right|^2 \tag{3.3}$$

In this equation, α is the incident angle of the wave onto the lens surface at arbitrary point P, as shown in Fig. 3.2, and is described as

$$\begin{aligned} \alpha = \frac{\pi}{2} + \tan^{-1}\left[\frac{y}{\sqrt{B^2 - A\left(D^2/4 - y^2\right)}}\right] \\ - \tan^{-1}\left[\frac{AL_F - B + \sqrt{B^2 - A\left(D^2/4 - y^2\right)}}{Ay}\right], \end{aligned} \tag{3.4}$$

where parameters A and B are defined in equation (3.2), and the y coordinate is shown in Fig. 3.2.

Fig. 3.3(a) shows the calculated transmittance (using equation (3.3)) dependence of the antenna gain on the focus distance of the lens by using a dashed line. The transmittance was normalized by those at a focus distance of 40 mm. This calculated result showed that the transmittance remarkably degraded where the focus distance was less than 25 mm. A dependence of the antenna gain on the focus distance was also simulated by using ANSYS HFSS$^{\text{TM}}$ to confirm the level of the gain degradation. The simulated result is shown by a solid line with open circles in Fig. 3.3(a). The gain degradation was normalized by those at the focus distance of 40 mm. In this simulation, the dielectric constant of 4.2 and $\tan\delta$ of 0.01 were used as loss factors for the lens. They were derived from the measurement results for the PPS. The material of the horn was aluminum with conductivity of 3.8 × 10^7 S/m. The calculation and simulation results were in good agreement as shown in Fig. 3.3(a). Fig. 3.3(b) shows a simulated dependence of a reflection coefficient S11 on the focus distance. Since the S11 of less than -13 dB in the sweep range of the focus distance is small enough, the S11 does not affect the gain. In accordance with these results, the focus distance

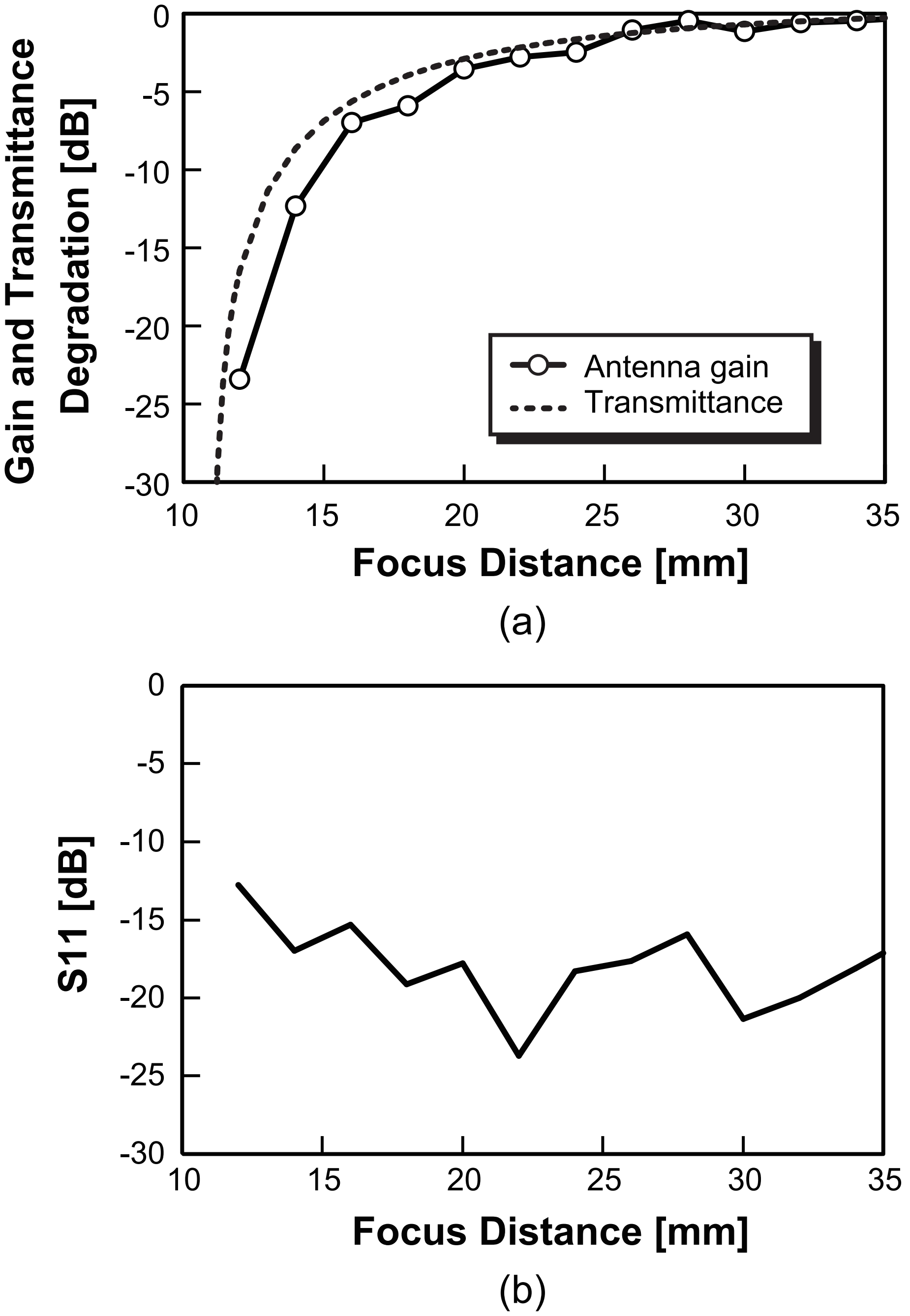

Fig. 3.3. (a) Calculated transmittance (dashed line) and simulated antenna gain (solid line with open circles) dependence of antenna gain (b) and reflection coefficient S11 dependence on focus distance of lens.

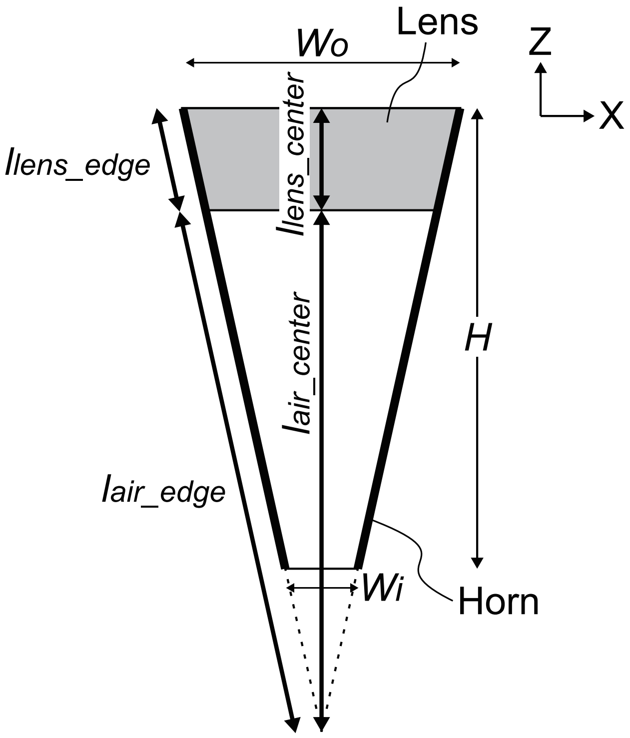

Fig. 3.4. Model of horn used to calculate maximum phase difference at horn output aperture in X direction.

of the lens L_F was designed to be 32 mm to reduce the low-height horn while keeping enough margin for gain degradation.

The maximum phase difference in the X direction of the radiated waves at the output aperture of the horn was within 180 degrees; therefore, the design method was different from that in the Y direction. The maximum phase difference was roughly calculated from the distances traveled by the waves at the center and edge of the horn for the four lenses shown in Fig. 3.4: $l_{\text{air\_center}}$, $l_{\text{lens\_center}}$, $l_{\text{air\_edge}}$, and $l_{\text{lens\_edge}}$. The thickness of the lens was constant. The maximum thickness of the lens was 6.8 mm, as obtained from equation (3.2), and horn height H was 29 mm. The calculated maximum phase difference of the radiated waves at the horn output aperture was 0.30π, which is close to that of the optimum horn (0.375π) [3.5]. Thus, the shape of the lens was designed flat in the X direction in consideration of the ease of production. As a result, a cylindrical lens was applied to the lens in this study.

Simulated radiation patterns of a horn with a lens antenna are shown in Fig. 3.5. The antenna gain was 25.1 dBi, and the HPBWs were 5 degrees in elevation and 15 degrees in azimuth. Fig. 3.6 shows simulated reflection coefficient S11 of the horn with a lens antenna. The horn with lens antenna had a wide matching bandwidth where the S11 was below -10 dB, and the S11 had dips which had an interval of about 4 GHz.

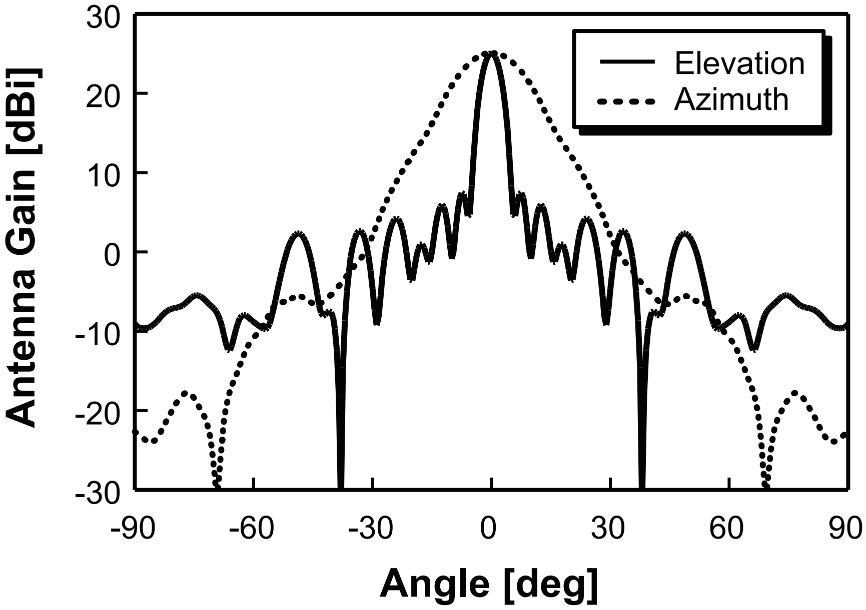

Fig. 3.5. Simulated radiation patterns of horn with lens antenna at 76.5 GHz.

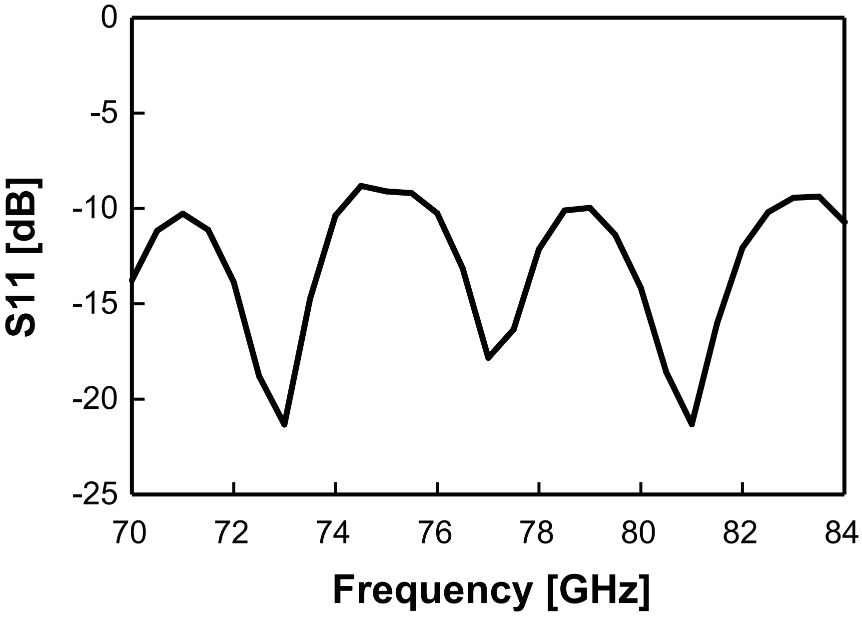

Fig. 3.6. Simulated reflection coefficient S11 of horn with lens antenna.

3.4 Robust design of horn-to-microstrip transition

3.4.1 Impedance matching with wide frequency band

In this section, a technology is presented for widening the frequency bandwidth to obtain a high tolerance to errors in the etching of metal patterns, such as the MSA used as a matching element in the proposed horn-to-microstrip transition.

A schematic of the MSA and the ground pattern around the antenna comprising a horn-to-microstrip transition is shown in Fig. 3.7(a). L_P and W_P are the lengths of the MSA in the Y and X directions, respectively. L_G and W_G are the lengths of the ground opening around the MSA in the Y and X directions, respectively. Using the MSA with the excited TM10 mode converts the quasi-TEM mode of the microstrip line into the TE10 mode of the horn. The size of the MSA was initially calculated from the following well-known equations for a rectangle MSA [3.5]. Here, h is the thickness of a dielectric layer of an antenna substrate, where $W_P/h > 1$. Rogers RO3003 was applied to the antenna substrate whose thickness of 0.127 mm, dielectric constant of 3.2, and $\tan\delta$ of 0.004.

$$\begin{cases} W_P = \dfrac{\lambda_0}{2}\sqrt{\dfrac{2}{e_r+1}} \\ L_P = \dfrac{\lambda_0}{2\sqrt{e_{eff}}} - 2\Delta L \\ e_{eff} = \dfrac{e_r+1}{2} + \dfrac{e_r-1}{2}\left[1+\dfrac{12h}{W_P}\right]^{-\frac{1}{2}} \\ \Delta L = 0.412h\dfrac{(e_{eff}+0.3)\left(\dfrac{W_P}{h}+0.264\right)}{(e_{eff}-0.258)\left(\dfrac{W_P}{h}+0.8\right)} \end{cases} \tag{3.5}$$

Fig. 3.8 shows the simulated reflection coefficient S11 of a lens horn antenna with a horn-to-microstrip transition. A reference plane of the S11 was placed on the feed line at the slot of the horns as indicated in Fig. 3.7(a). The dotted line indicates the S11 of the proposed antenna with the MSA, horn, and lens. The S11 had dips whose interval was about 4 GHz indicated by arrows in Fig. 3.8, where the frequency of the dips and their interval were almost the same as those observed in Fig. 3.6. Therefore, the origin of these dips was the result of impedance matching of the lens horn antenna, and the dips appeared in the S11 of the horn-to-microstrip transition due to impedance matching between the input-aperture of the horn and leading radiating edge of the MSA. A dip in the S11 at 76 GHz was caused by the above mechanism. Here, the

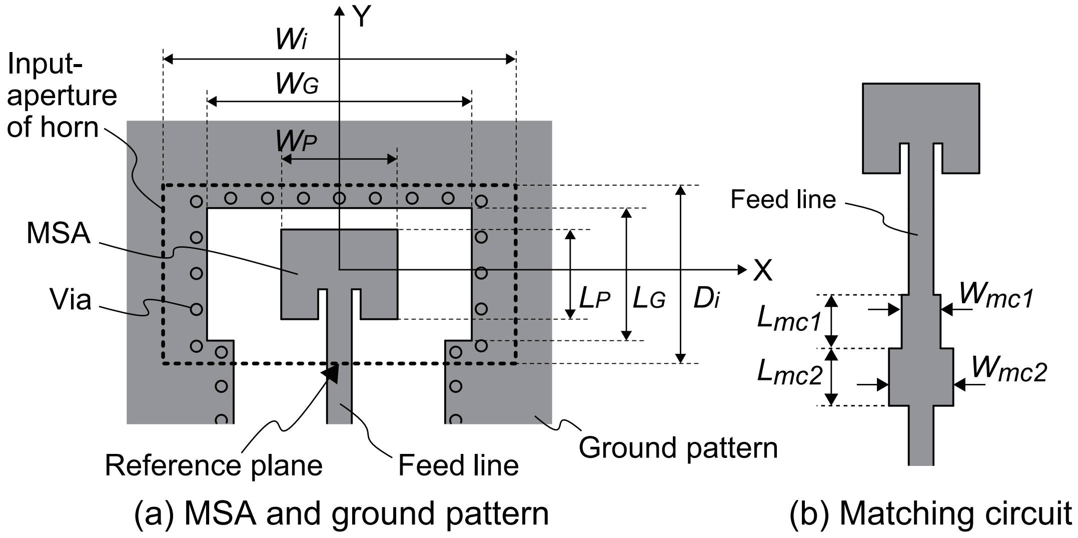

Fig. 3.7. Schematic of MSA and ground pattern, and impedance matching circuit.

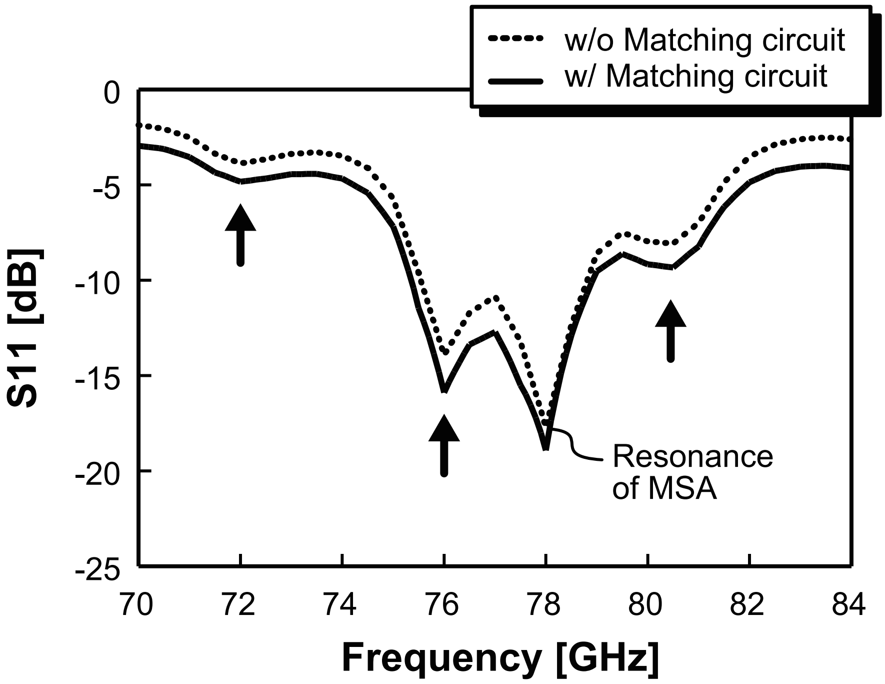

Fig. 3.8. Simulated reflection coefficient S11 of proposed antenna with horn-to-microstrip transition.

frequencies of the dips were different by about 1 GHz between Figs. 3.6 and 3.8, which might be caused by difference of terminated impedance of the input-aperture of the horn; the input-aperture of the horn was terminated by a waveguide port in Fig. 3.6, while that was terminated by an MSA and ground pattern in Fig. 3.8. To widen the frequency bandwidth, the resonance frequency of the MSA was designed to be about 77.5 GHz, which is higher than the frequency of the dip at 76 GHz. This takes into consideration the potential misalignment between the horn and MSA detailed in the next section. The optimized size of the MSA ($L_p \times W_p$) was 1.02 × 1.33 mm.

A matching circuit was inserted into the feed line to expand the bandwidth by 10%. As shown in Fig. 3.7(b), it consisted of two microstrip lines (L_{mc1} and L_{mc2}), each with a length of $\lambda_g/4$, where λ_g is the effective wavelength of microstrip lines. Their widths for matching circuits W_{mc1} and W_{mc2} were 0.35 and 0.5 mm, respectively. As shown in Fig. 3.8, the proposed lens horn antenna with the horn-to-microstrip transition had a frequency bandwidth of 3.6 GHz where the S11 was below -10 dB.

3.4.2 Robust design against misalignment of horn and MSA

A design process to obtain a high tolerance to misalignment due to mechanical deviation during mass production is presented in this section. The proposed antenna has three components (horn, lens, and MSA), so misalignment of these three components in the X, Y, and Z directions should be investigated. Misalignments of these components in the Z direction are negligible because they can be tightly assembled by using screws or other methods. A misalignment of the lens and horn in the X or Y direction is also negligible due to the shape of the lens, which is convex on the inside of the horn. However, misalignment of the horn and MSA can occur in the assembly process due to mechanical deviation during production. Therefore, the robustness against misalignment of the horn and MSA was investigated in this study.

The horn must contact the ground pattern around the MSA to reduce the reflection at the input aperture of the horn. In a rectangular waveguide-to-microstrip transition [2.5], the openings of a ground pattern L_2 surrounded by vias are designed to be the same size as the waveguide aperture L_1, as shown in Fig. 3.9, to obtain the same impedance on both sides of the matching element. The optimum structure for the opening of the ground pattern for a horn-to-microstrip transition differs from that for a rectangular waveguide because the impedance of the horn aperture depends on the horn height. Therefore, the optimum structure of the ground pattern for a horn-to-microstrip transition was investigated with respect to the antenna gain degradation.

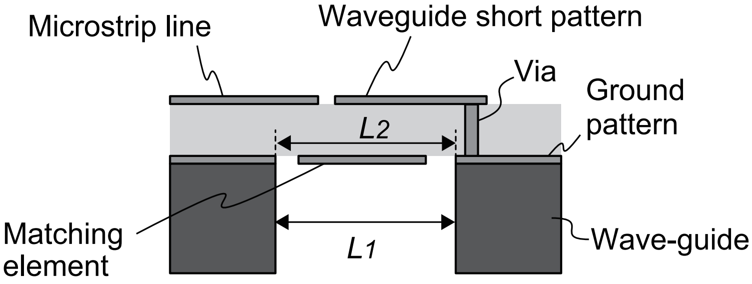

Fig. 3.9. Structure of rectangular waveguide-to-microstrip transition [2.5].

3.4.2.1 Maximum gain degradation

A method for designing the ground opening size to obtain a high tolerance to misalignment of the horn and MSA during production is presented in this section. First, the dependence of the maximum gain on the ground opening length L_G and the misaligned length dY of the horn in the Y direction is discussed. The X and Y coordinates are defined in Fig. 3.1(a), and the aligned integration (dY=0 mm) indicates where the center of the input aperture of the horn and the MSA overlap. The size of the MSA and input aperture of the horn are the same as those described in Section 3.4.1.

The simulated dependence of the antenna gain variation on the misaligned length dY at 76.5 GHz is shown in Fig. 3.10, where the gains were normalized by that at dY =0 mm. The solid lines with open circles, triangles, and squares indicate the results for ground patterns with openings ($L_G \times W_G$) of 1.5 × 3 mm, 2 × 3 mm, and 2.5 × 3 mm, respectively. The misaligned length dY of the horn was varied from -0.3 to 0.3 mm. The results show that the ground patterns with openings of 1.5 × 3 mm and 2 × 3 mm produced a small gain degradation (within 0.3 dB) at misaligned length dY=±0.3 mm. In contrast, the antenna gain for the ground pattern with an opening of 2.5 × 3 mm was degraded by 3 dB at misaligned length dY=-0.3 mm.

To analyze these results, the reflection coefficients S11 for each structure were simulated. Fig. 3.11 shows the simulation results for the ground patterns with an opening of 1.5 × 3 mm and 2.5 × 3 mm. The dotted and solid lines indicate S11 at misaligned lengths dY of 0 and -0.3 mm, respectively.

The simulation results for the ground pattern with an opening of 1.5 × 3 mm showed that the dip around 78 GHz shifted to a lower frequency at dY=-0.3 mm, and S11 at 76.5 GHz decreased as a result. The shift of the dip in the S11 was caused by increasing coupling capacitance of the MSA as it came closer to the horn. The resonance frequency of the MSA was designed to be higher than the 77-GHz band, as described in Section 3.4.1, so the ground pattern with an opening of 1.5 × 3 mm provided a high tolerance to misalignment of the horn and MSA.

In contrast to the simulation results of S11 for a ground pattern with an opening of

1.5 × 3 mm, those for one with an opening of 2.5 × 3 mm were degraded: from -11 dB to -6 dB at 76.5 GHz for dY=-0.3 mm, as shown in Fig. 3.11(b). To illustrate the cause of this degradation, schematics of the horn and MSA integrations are shown in Fig. 3.12 for (a) misaligned length dY of 0 and (b) $-\Delta L$. The shaded areas in the figures represent the post-wall waveguide part surrounded by the horn, ground pattern in the bottom layer, and the vias. Its length L_{pwg} is extended from 0.05 mm ($0.02\lambda_g$) to 0.55 mm ($0.23\lambda_g$) by the misaligned length dY ($= -\Delta L$) of -0.3 mm, which is close to $\lambda_g/4$. As a result, the post-wall waveguide part works as an open stub. This changes the impedance condition of the reference ground for the MSA from short to open near the leading radiating edge of the MSA, and this impedance mismatch of the MSA causes as a result. This degradation of S11 corresponds to a gain degradation of 0.8 dB. The rest of the S11 degradation of 2.2 dB may have been caused by a standing-wave in the post-wall waveguide part. A large current flow through the vias, which are the terminal edge of the open stub, and some of the fed power is consumed.

Simulation results for a surface current distribution on a ground pattern in the bottom layer of the antenna substrate are shown in Fig. 3.13 for ground patterns with openings of (a) 1.5 × 3 mm and (b) 2.5 × 3 mm. The surface current at misaligned lengths dY of 0 mm and -0.3 mm are depicted in the left and right areas, respectively. A large concentration of surface current formed around the vias for the ground pattern with an opening of 2.5 × 3 mm, as indicated by the dotted oval in Fig. 3.13(b) while such a concentration was not observed for the ground pattern with an opening of 1.5 × 3 mm (Fig. 3.13(a)). A concentration of surface current indicates that some of the fed power is consumed, as described above. These simulation results for the surface current distribution indicate that some of the gain degradation was caused by the standing-wave at the post-wall waveguide part, which had a length close to $\lambda_g/4$.

Next, the dependence of the variation in the maximum gain on the ground opening length W_G and the misaligned length dX of the horn is discussed. The simulated dependence of the antenna gain variation on the misaligned length dX at 76.5 GHz is shown in Fig. 3.14, where the gains were normalized by that at dY=0 mm. The solid lines with open circles, triangles, and squares indicate the results for ground patterns with openings ($L_G \times W_G$) of 1.5 × 3 mm, 1.5 × 4 mm, and 1.5 × 5 mm, respectively. The misaligned length dX of the horn was varied from -0.3 to 0.3 mm. The gain degradations caused by the misalignment of the horn in the X direction were within 0.02 dB at the whole variation of the misalignment and were smaller than those in the Y direction. These results were due to the structure of the MSA and horn: the distance between the antenna and horn was sufficiently large, and the misalignment did not affect the TM10 mode of the antenna.

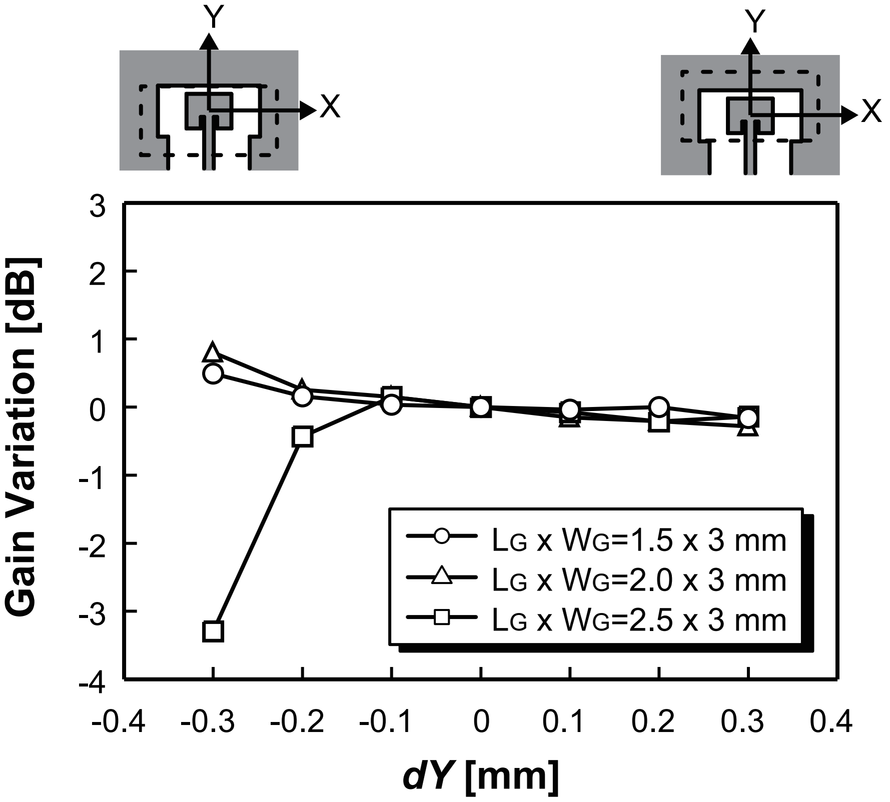

Fig. 3.10. Simulated misalignment dependence of antenna gain in Y direction at 76.5 GHz.

In accordance with these simulation results for the gain degradation caused by the misalignment of the horn and MSA in the X and Y directions and in consideration of the margin of fabrication errors for the input-aperture size of the horn and opening of the ground pattern, a ground pattern with an opening ($L_G \times W_G$) of 1.5 $\times$ 3 mm was selected for this study.

3.4.2.2 Beam-tilt due to horn misalignment

The beam-tilts of the major lobes caused by misalignment of the horn in the X and Y directions are described here. The simulation results for beam-tilt angles at 76.5 GHz are plotted in Fig. 3.15 for a ground pattern with an opening ($L_G \times W_G$) of 1.5 $\times$ 3 mm. The directions of the misalignment and beam-tilts in elevation and azimuth are defined in Fig. 3.1(a). The solid lines with open circles and triangles indicate the misalignment of the horn in the Y and X directions, respectively. The misaligned length dY of the horn was varied from -0.3 to 0.3 mm in each direction. The beam-tilt angles of the proposed antenna were within 0.3 degrees in elevation and 0.7 degrees in azimuth for misaligned lengths dY=0.1 mm and dX=0.1 mm, respectively.

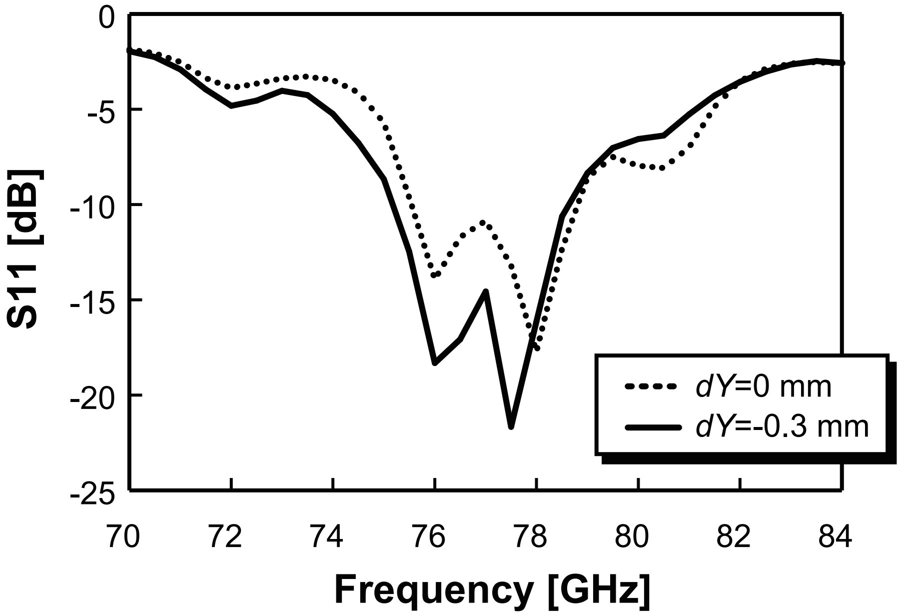

(a) Ground opening of 1.5 x 3 mm

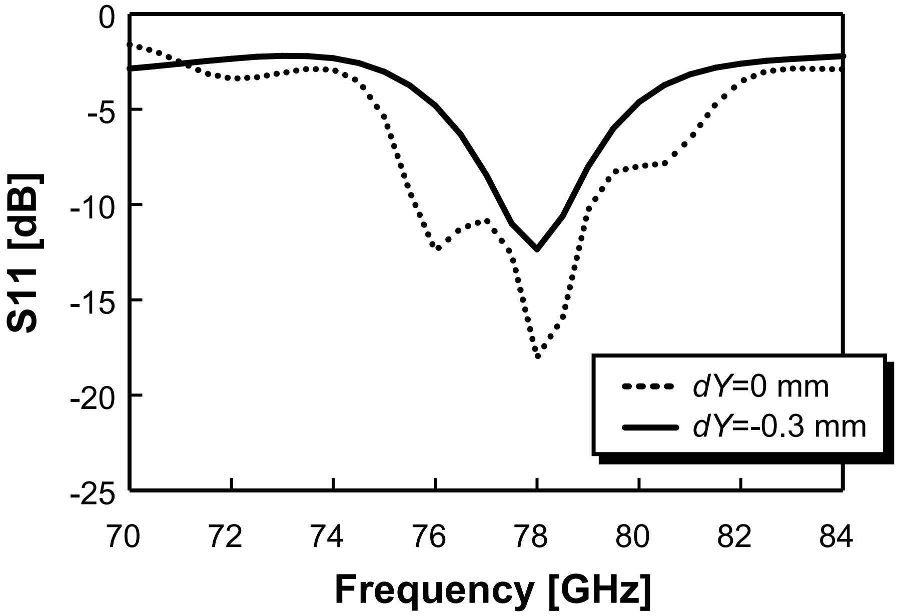

(b) Ground opening of 2.5 x 3 mm

Fig. 3.11. Simulated reflection coefficient S11 with respect to horn misalignment in Y direction.

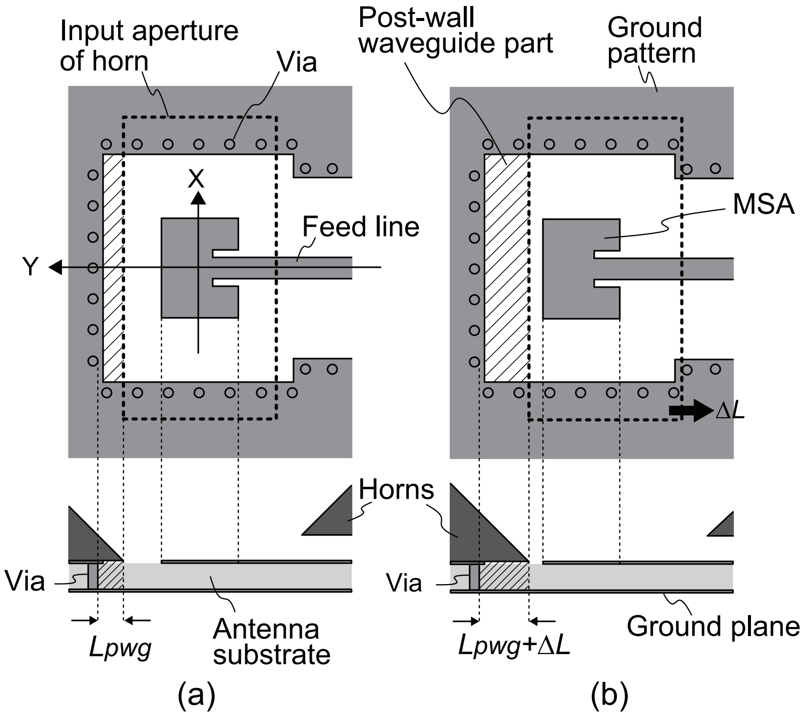

Fig. 3.12. Schematic of horn and MSA integration with ground pattern opening of 2.5 × 3 mm: (a) dY of 0 and (b) $-\Delta L$.

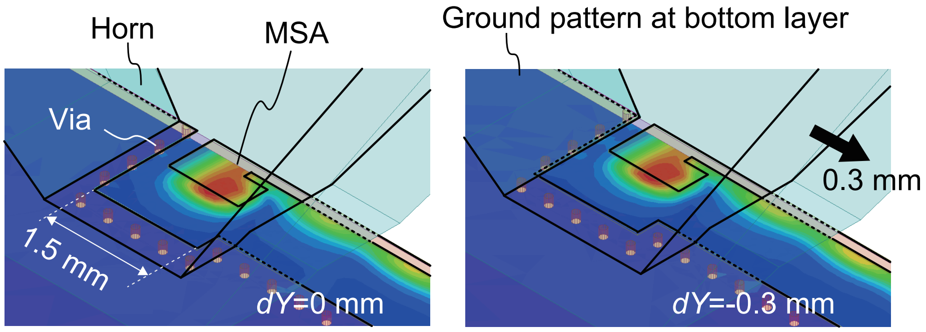

(a) Ground opening of 1.5 x 3 mm

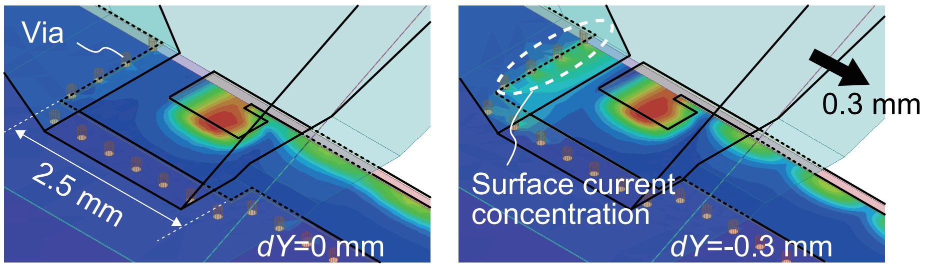

(b) Ground opening of 2.5 x 3 mm

Fig. 3.13. Surface current distribution for ground openings of (a) 1.5 × 3 mm and (b) 2.5 × 3 mm.

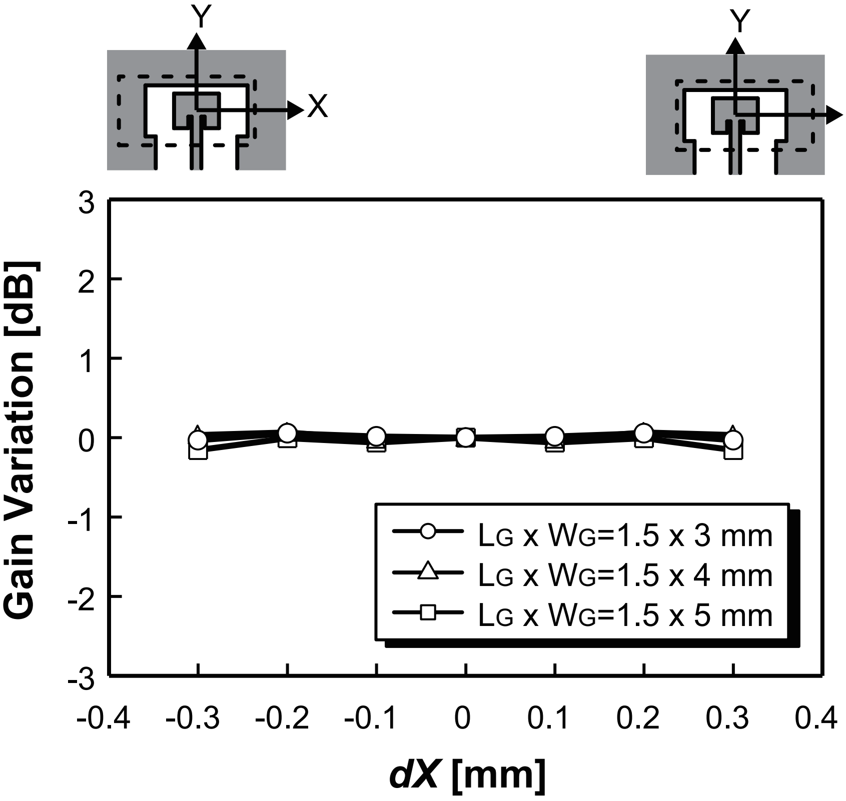

Fig. 3.14. Simulated misalignment dependence of antenna gain in X direction at 76.5 GHz.

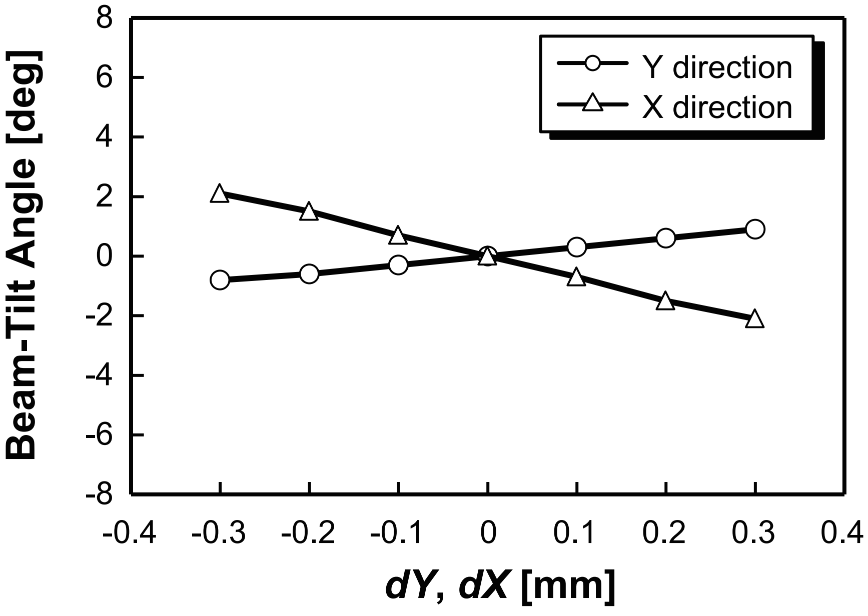

Fig. 3.15. Simulated misalignment dependence of beam-tilt at 76.5 GHz for ground pattern with opening of 1.5 × 3 mm.

3.5 Simulation results for radiation performance and loss factors

This section summarizes the simulation results described in Sections 3.3 and 3.4. Parameters of the materials used in the proposed antenna as loss factors are summarized in Table 3.1. Fig. 3.16 shows the simulated radiation pattern of the proposed antenna for a horn-to-microstrip transition at 76.5 GHz, where the feed point was placed on the feed line at the slot of the horns as indicated Fig. 3.1(a). The solid and dotted lines represent the radiation pattern for elevation and azimuth, respectively. The proposed antenna had an antenna gain of 23.6 dBi, and the HPBWs were 5 and 15 degrees in elevation and in azimuth, respectively. The radiation pattern for elevation was asymmetrical due to radiation by the feed line in the input aperture of the horn and the asymmetrical structure of the input aperture of the horn, which had a slot to pass through the feed line, as shown in Fig. 3.1(b).

The simulated antenna gains and losses are listed by component in Table 3.2. The antenna gain of an optimum horn is about 26.0 dBi as calculated using an aperture efficiency of about 60%. Thus, the loss due to reducing the height of the horn by using a dielectric lens was 0.9 dB. The transmission loss of the horn-to-microstrip transition was 1.5 dB.

Table 3.3 summarizes the simulation results for the antenna gain variation and beam-tilt angle of the proposed antenna at 76.5 GHz for a misaligned length of the horn to MSA of 0.1 mm. They show that the proposed transition between the horn and microstrip line had a high tolerance to misalignment since the gain degradation of 0.03 dB and beam-tilt angles of 0.3 and 0.7 degrees were small enough compared with the antenna gain of 23.6 dBi and HPBWs of 5 and 15 degrees in elevation and azimuth, respectively.

Table 3.1. Parameters of materials used in simulations for proposed antenna.

Element	Material	Parameter	Value
Horn	Al	Conductance	3.8×10^7 S/m
Lens	PPS	e_r	4.2
		$\tan\delta$	0.01
Antenna substrate	RO3003	e_r	3.2
		$\tan\delta$	0.004

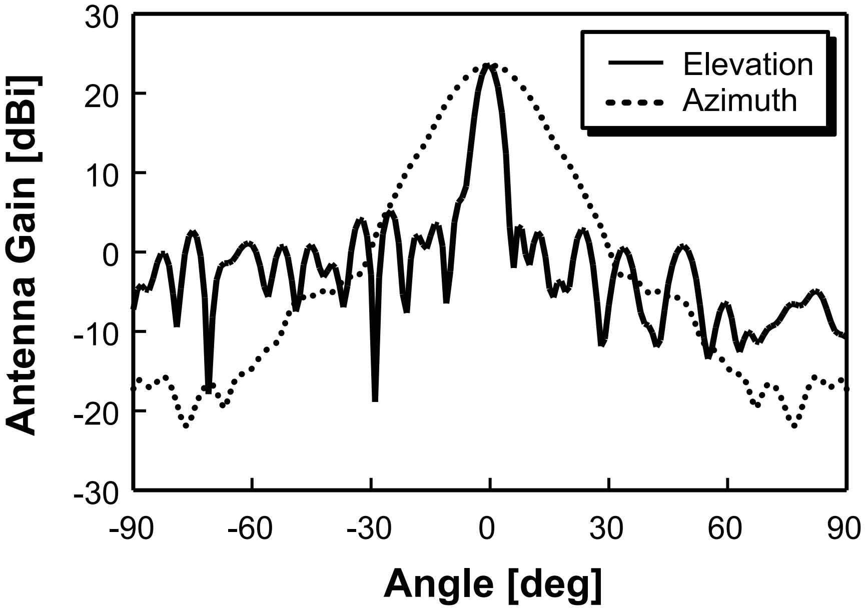

Fig. 3.16. Simulation results for radiation patterns at 76.5 GHz.

Table 3.2. Simulated antenna gains and loss factors at 76.5 GHz.

Item	Aperture efficiency	Antenna gain
Optimum horn antenna	∼60%	∼26.0 dBi
Proposed antenna without transition	49.3%	25.1 dBi
Proposed antenna with transition	34.6%	23.6 dBi

Factor	Loss
Height reduction of horn with lens	0.9 dB
Horn-to-microstrip transition	1.5 dB

Table 3.3. Simulated maximum gain degradation and beam-tilt angle for misaligned length dY of ±0.1 mm at 76.5 GHz.

Item	Horn misalignment	Variation
Antenna gain degradation	Y direction	0.04 dB
	X direction	0.02 dB
Beam-tilt angle	Y direction	0.3 degrees
	X direction	0.7 degrees

3.6 Fabricated antenna and measurement results

3.6.1 Fabricated antenna

Photographs of the fabricated antenna are shown in Fig. 3.17: (a) and (b) show perspective views of the antenna without and with the dielectric lens, respectively, and (c) shows a top view without the lens. The antenna had an output-aperture size ($D_o \times W_o$) of 45 $\times$ 18 mm and a height (H) of 29 mm. The size of the antenna substrate ($W_s \times L_s$) in the fabricated prototype antenna required to fix the horn to the antenna substrate was 20 $\times$ 20 mm, which was determined by referring to a standard WR-10 waveguide. In the measurement setup, the antenna substrate was pasted onto an aluminum plate. The horn was fixed to the aluminum plate with the antenna substrate with 4 mmϕ screws, which are commonly used to connect a standard WR-10 waveguide. Therefore, the size of the antenna substrate can be reduced by changing the method used to fix the horn and the antenna substrate, such as by reducing the number of screws or reducing the screw pitch. In principle, the required size of the antenna substrate is 4 $\times$ 2 mm which is equivalent to the input-aperture size of the horn. Hereafter, the antenna substrate size is used in comparison with the previous works.

Aluminum and PPS were used as the materials for the pyramidal horn and dielectric lens, respectively. A mono-layer resin substrate (Rogers RO3003) was applied to the antenna substrate.

3.6.2 Measurement results

The simulation and measurement results for the normalized gain of the fabricated antenna at 76.5 GHz are shown in Fig. 3.18 for (a) elevation and (b) azimuth. The insertion loss of the feed line for measurement was de-embedded, where the feed point was shown in Fig. 3.1(a). The solid and dotted lines indicate the measurement and simulation results, respectively. The antenna achieved an antenna gain of 23.5 dBi and produced HPBWs of 4.5 and 16 degrees in elevation and azimuth, respectively. The measurement results are in good agreement with the simulation results with respect to the major lobes in both directions.

The simulated and measured reflection coefficient S11 of the fabricated antenna is shown in Fig. 3.19, where a reference plane was placed at the end of a feed line for measurement with insertion loss of about 2 dB. The solid and dotted lines indicate the measurement and simulation results, respectively. The measurement results had two dips due to impedance matching of horn with lens and resonance of the MSA, the same as for the simulation results at around 76 GHz and 78 GHz, respectively. For the S11 below -10 dB, the fabricated antenna had a wide frequency bandwidth for

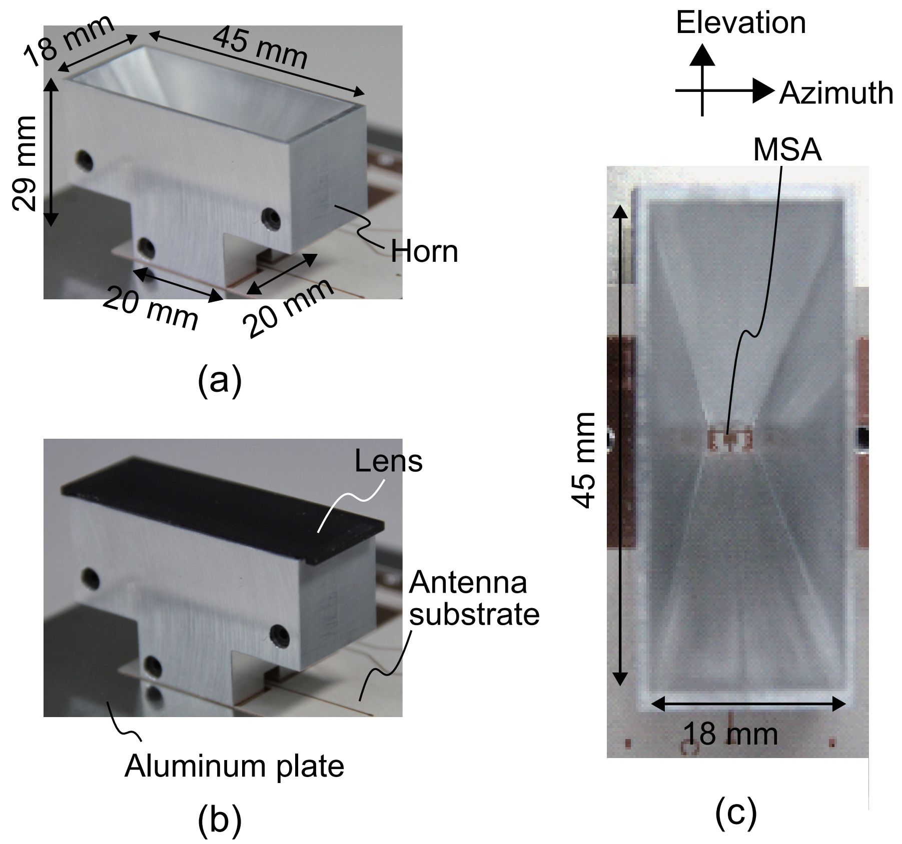

Fig. 3.17. Photographs of fabricated antenna: (a) perspective view without dielectric lens, (b) perspective view with lens, and (c) top view without lens.

impedance matching of up to 4 GHz, which is sufficient for a 1-GHz bandwidth in the 77-GHz band. The proposed antenna therefore has a high tolerance to frequency variations caused by size deviation of the MSA during fabrication.

Table 3.4 shows a benchmark comparison with other antennas. In comparison with the antennas with a microstrip line as the feed element, the proposed antenna provided higher antenna gain per unit area of the antenna substrate than the conventional series-fed microstrip patch array antenna [2.13]. The proposed lens horn antenna can reduce its cost because of small size of antenna substrate, where the additional costs for the horn and lens are negligibly small by using the existing frame and radome in LRRs, respectively. The fabricated antenna had a height (H) of 29 mm, which is low enough for LRRs because they are usually installed in areas behind the bumper or emblems on the front grill, which has a depth of several centimeters, as mentioned in Section 2.2.

The measured antenna gain variations caused by misalignment of the horn and MSA at 76.5 GHz are shown in Fig. 3.20 for (a) misaligned lengths of dY and (b) dX. The solid line with closed circles and dotted line with open circles indicate the

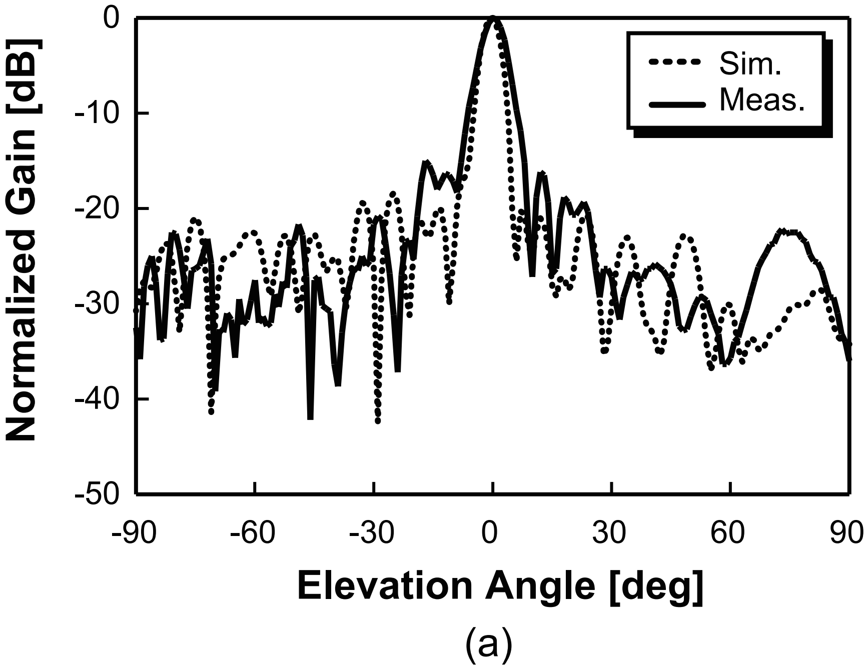

(a)

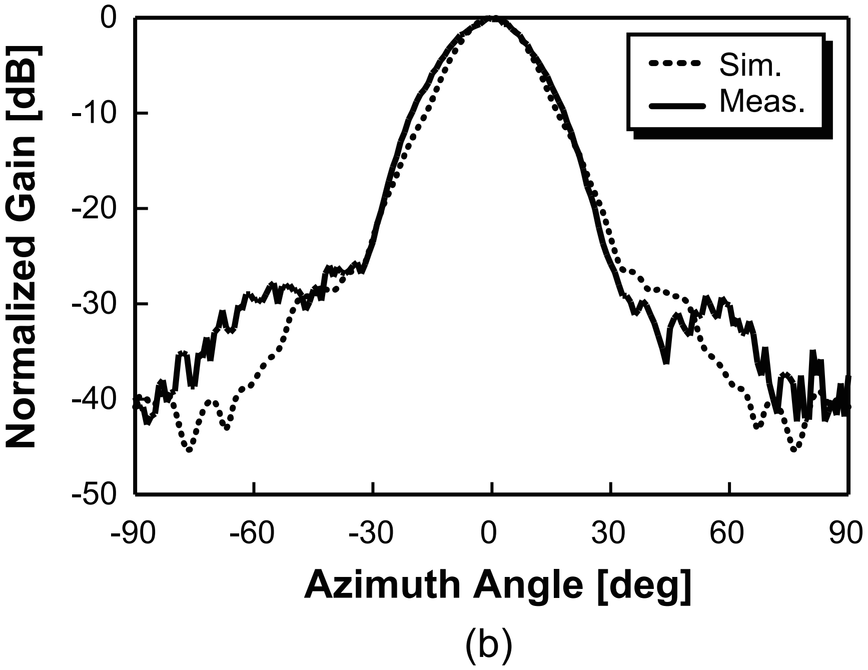

(b)

Fig. 3.18. Measured radiation patterns of fabricated antenna at 76.5 GHz.

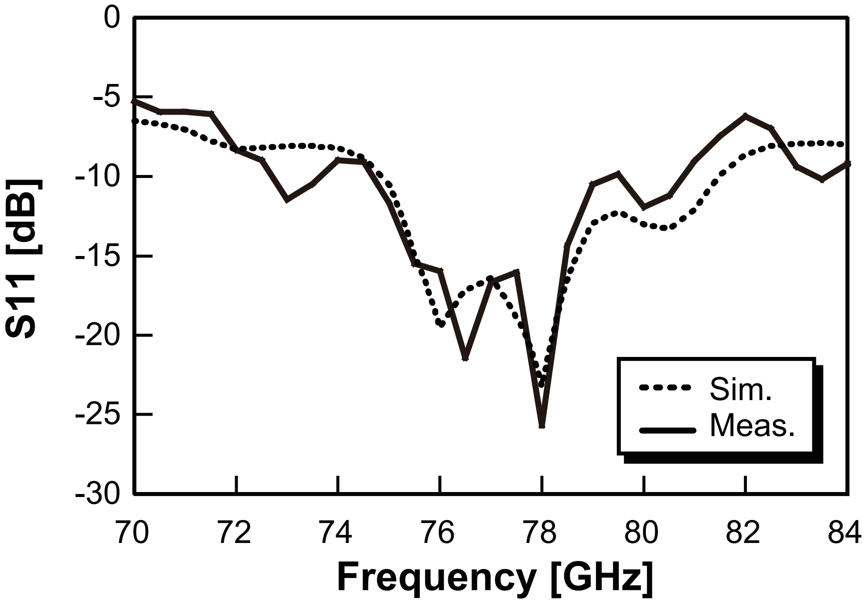

Fig. 3.19. Measured reflection characteristics S11 of fabricated antenna.

Table 3.4. Benchmark comparison of antennas for millimeter-wave radars for automotive applications.

Item	This study	[2.13]	[2.16]	[2.17]
Antenna type	Lens horn antenna with single MSA	MSA array	Lens and MSA array	Lens and MSAs
Feed elements	Microstrip line	Microstrip line	Microstrip line	Microstrip line
e_r of antenna substrate	3.2	2.2	N.A.	2.6
Frequency	76–77 GHz	76–77 GHz	76–77 GHz	76–77 GHz
Antenna gain	23.5 dBi	22.5 dBi	MSA array $+1.5$ dB	20.2 dBi
Output-aperture area	810 mm^2	408 mm^2	3588 mm^2	875 mm^2
Substrate area (in principle)	8 mm^2 (prototype $\leq$ 400 mm^2)	408 mm^2	3588 mm^2	1113 mm^2
Antenna height	29 mm	N.A.	N.A.	17.66 mm

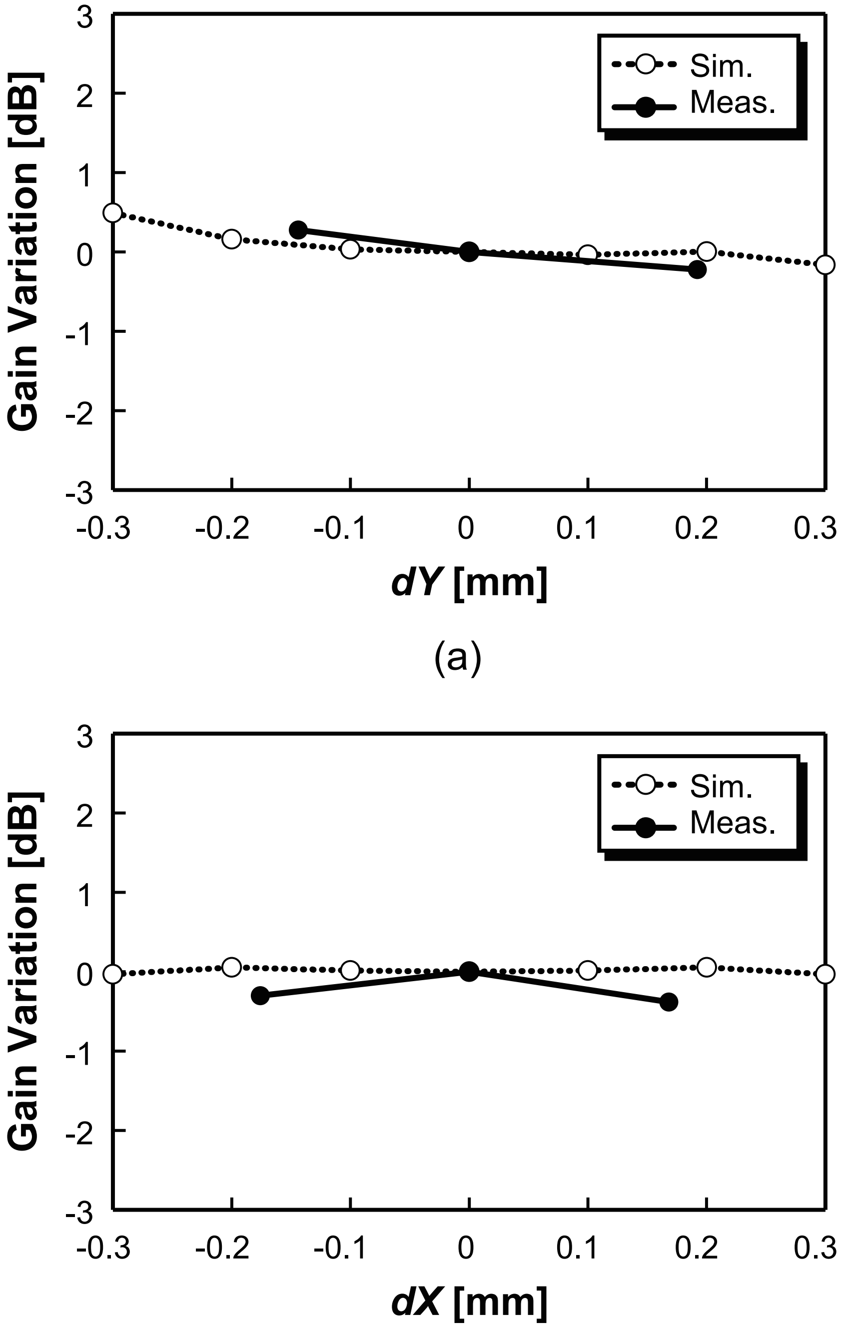

Fig. 3.20. Measured misalignment dependence of antenna gain variation at 76.5 GHz

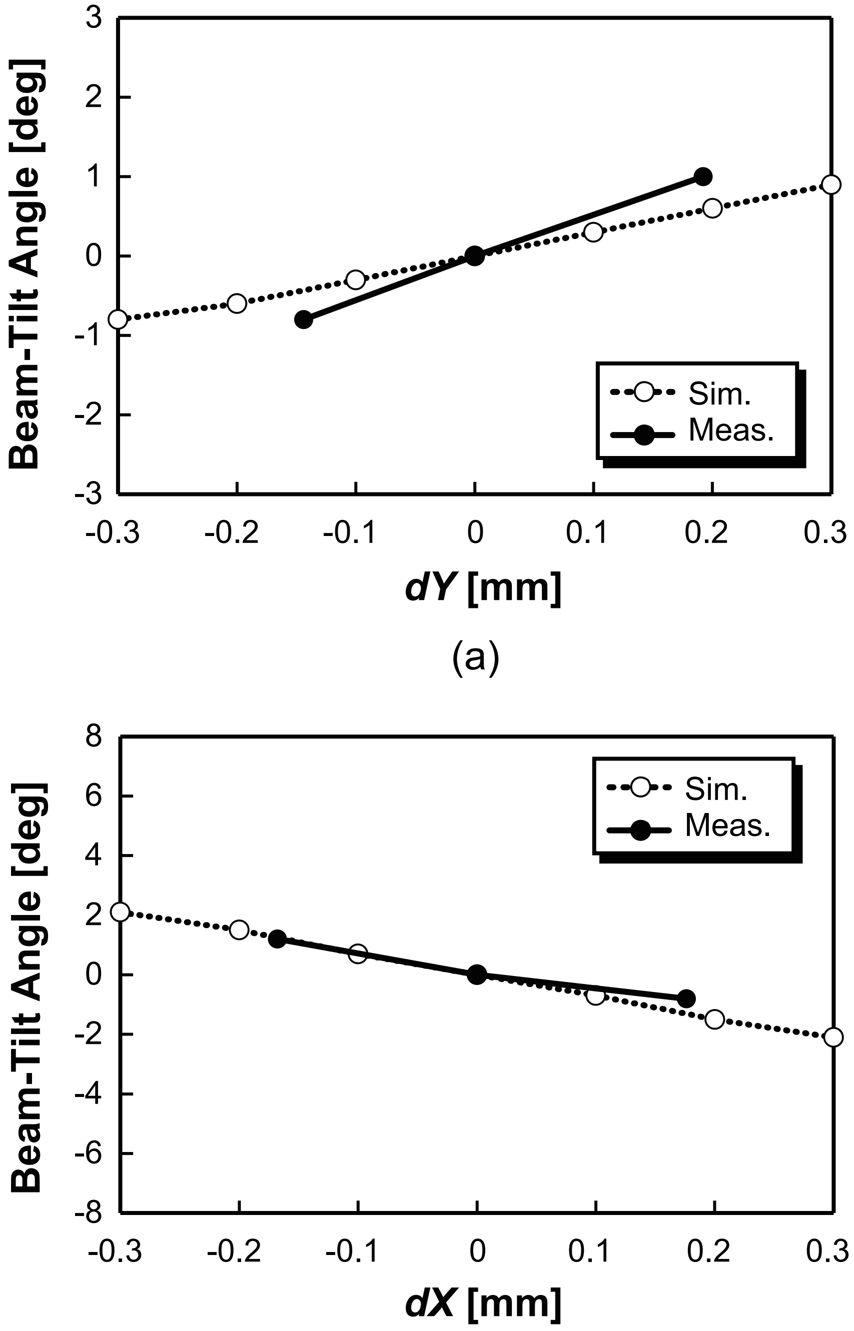

(a)

(b)

Fig. 3.21. Measured misalignment dependence of beam-tilt angle at 76.5 GHz.

Table 3.5. Measurement results for maximum gain degradation and beam-tilt angle at misaligned length dY of ±0.1 mm at 76.5 GHz.

Item	Horn misalignment	Variation
Antenna gain degradation	Y direction	0.1 dB
	X direction	0.2 dB
Beam-tilt angle	Y direction	0.6 degrees
	X direction	0.7 degrees

measurement and simulation results, respectively. The measurement results showed the same tendency as the simulation results. The fabricated antenna provided a gain degradation of 0.1 dB and 0.2 dB, respectively, where misaligned lengths dY and dX were within ±0.1 mm.

Fig. 3.21 shows the measurement results for the beam-tilt angles at 76.5 GHz for (a) misaligned lengths of dY and (b) dX. The solid line with closed circles and dotted line with open circles indicate the measurement and simulation results, respectively. The measurement results had the same tendency and order as the simulation results in both the Y and X directions. The fabricated antenna provided beam-tilt angles of 0.6 degrees and 0.7 degrees, respectively, where misaligned lengths dY and dX were within ±0.1 mm.

The measurement results for the gain degradation and beam-tilt angle are listed in Table 3.5, where the misaligned lengths of the horn to the MSA (dY and dX) were ±0.1 mm. These results demonstrate that the proposed antenna with a horn-to-microstrip transition has a high tolerance to misalignment caused by mechanical variation during mass production since the maximum gain degradation of 0.2 dB was small enough compared with the antenna gain of 23.5 dBi. The beam-tilt angles of 0.6 and 0.7 degrees were also small compared with the HPBWs of 4.5 and 16 degrees in elevation and azimuth, respectively.

3.7 Versatility of proposed lens horn antenna fed by single microstrip antenna

A design frequency dependence of the proposed antenna with horn, lens, and MSA has been investigated as a versatility of the proposed technology in the previous sections. The frequency of 60, 90, and 110 GHz were chosen as examples, which are commonly applied to radar sensors or wireless communication systems.

First, I explain a method to optimize the size of the proposed antenna for the

77-GHz band to other frequencies. The size of the output-aperture of the horn is determined by using the equation (3.1) which has an item on frequency. Since the maximum phase difference in the X direction depends on the flare angle of the horn, the height and input-aperture size of the horn are automatically decided from the output-aperture size of the horn. The shape of the dielectric lens is provided by using the equation (3.2), which do not depend on the frequency. The antenna gain of the antenna with horn and lens depends on the focus distance of the lens as shown in Fig. 3.3. The focus distance is in proportion to the height of the horn while keeping the flare angle of the horn. Therefore, the focus distance of the lens is also uniquely determined from the output-aperture size.

According to the above discussion on the dependence of the sizes of the elements in the antenna on the design frequency, the sizes of the horn and lens were changed corresponding to the design frequency using the following equation.

$$Size(f_1) = Size(f_0) \times \frac{f_0}{f_1} \tag{3.6}$$

Here, f_0 and f_1 are 76.5 GHz and the design frequency, respectively, and $Size(f_0)$ and $Size(f_1)$ are the size of the horn and lens for the design frequency of f_0 and f_1, respectively. By using the equation, the output-aperture sizes ($W_o \times D_o$) became 23 × 57, 15 × 38, and 13 × 31 mm for the design frequency of 60, 90, and 110 GHz, respectively. The input-aperture sizes ($W_i \times D_i$) were 5.1 × 2.55, 3.4 × 1.7, and 2.8 × 1.4 mm for the design frequency of 60, 90, and 110 GHz, respectively. The heights of the horn were 41, 27, and 22 mm, and focus distances of the lens were 41, 27, and 22 mm for the design frequency of 60, 90, and 110 GHz, respectively.

On the other hand, the size of the MSA was optimized using the equation (3.5) to provide the largest directivity in each design frequency. Moreover, the thickness of the substrate was determined by using the equation (3.6) to prevent a higher-order mode which stands in the dielectric substrate. The sizes of the MSA ($W_p \times L_p$) became 1.73 × 1.33, 1.15 × 0.89, and 0.94 × 0.73 mm for the design frequency of 60, 90, and 110 GHz, respectively.

The above main parameters of the antenna are listed in Table 3.6. To simplify the comparison, the matching circuit added the input terminal of the MSA was not applied in this section.

Next, I describe and discuss simulation results of the antennas designed in each frequency. Simulated results for the antenna gain are shown in Fig. 3.22. Solid and dotted lines indicate the antenna gain in elevation and azimuth, respectively, in each graph. The simulation used the same parameters of the materials for the horn, lens, and antenna substrate as those described in Table 3.1. The antenna gains of each antenna were 23.7, 23.7, and 23.9 dBi for the design frequency of 60, 90, and 110

Table 3.6. Main parameters of proposed antenna for each design frequency.

Design frequency	60 GHz	76.5 GHz	90 GHz	110 GHz
Output-aperture size [mm]	23×57	18×45	15×38	13×31
Input-aperture size [mm]	5.1×2.55	4×2	3.4×1.7	2.8×1.4
Horn height [mm]	37	29	25	20
Lens focus distance [mm]	41	32	27	22
MSA size [mm]	1.73×1.33	1.33×1.02	1.15×0.89	0.94×0.73
Substrate thickness [mm]	0.162	0.127	0.108	0.088

Table 3.7. Comparison of simulation results for main performance of antennas.

Design frequency		60 GHz	76.5 GHz	90 GHz	110 GHz
Antenna gain		23.7 dBi	23.6 dBi	23.7 dBi	23.9 dBi
HPBW	Elevation	5°	5°	5°	5°
	Azimuth	16°	15°	16°	16°
Matching frequency bandwidth ($S11 < -10$ dB)		2.5 GHz	3.3 GHz	3.9 GHz	4.6 GHz
Relative matching frequency bandwidth		4.1%	4.3%	4.3%	4.2%

GHz, respectively. The antennas whose design frequencies were 60, 90, and 110 GHz had the HPBWs of 5 and 16 degrees in elevation and azimuth, respectively. These results are comparable to those for the antenna whose design frequency is 76.5 GHz.

Simulated results for the reflection coefficient S11 are shown in Fig. 3.23. The matching frequency bandwidths where the S11 is below -10 dB were 2.5, 3.9, and 4.6 GHz for the design frequency of 60, 90, and 110 GHz, respectively. To compare the performance of the matching frequency bandwidth, I calculated a relative bandwidth BW_r of each antenna by using the following equation:

$$BW_r = \frac{BW}{f_1}, \tag{3.7}$$

where BW is the matching frequency bandwidth and f_1 is the design frequency. The antennas whose design frequencies were 60, 76.5, 90, and 110 GHz had the relative matching frequency bandwidths of 4.1%, 4.3%, 4.3%, and 4.2%, respectively. These results showed that the relative matching frequency bandwidth of the antennas designed with frequencies of 60, 90, and 110 GHz were comparable to those for the antenna whose design frequency was 76.5 GHz.

The above simulated results are listed in Table 3.7. Since the simulation results for

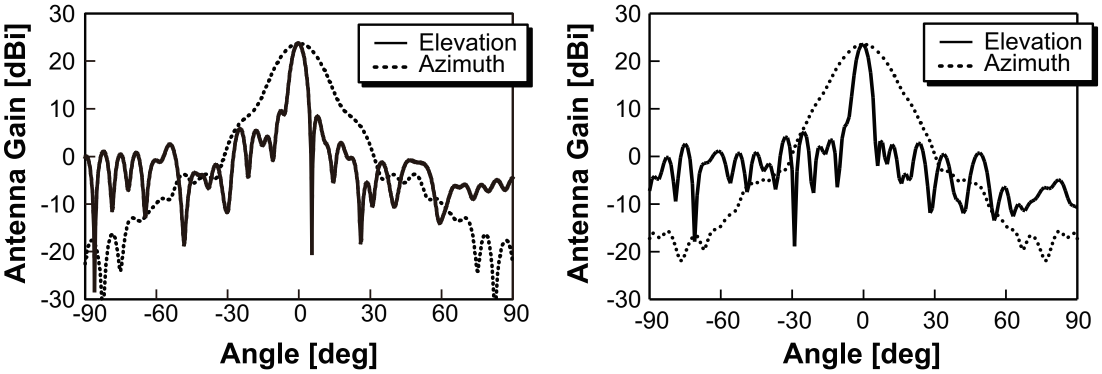

(a) 60 GHz (b) 76.5 GHz

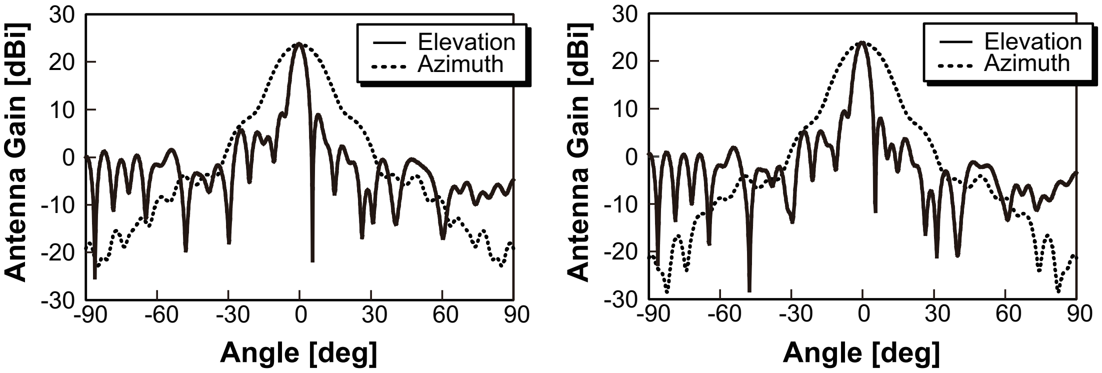

(c) 90 GHz (d) 110 GHz

Fig. 3.22. Simulation results for radiation pattern of antenna with horn, lens, and MSA whose design frequencies were (a) 60 GHz, (b) 76.5 GHz, (c) 90 GHz, and (d) 110 GHz.

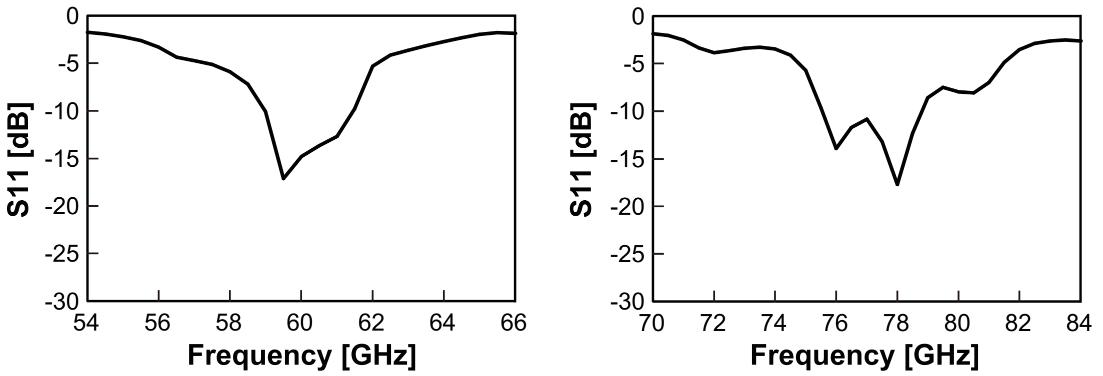

(a) 60 GHz (b) 76.5 GHz

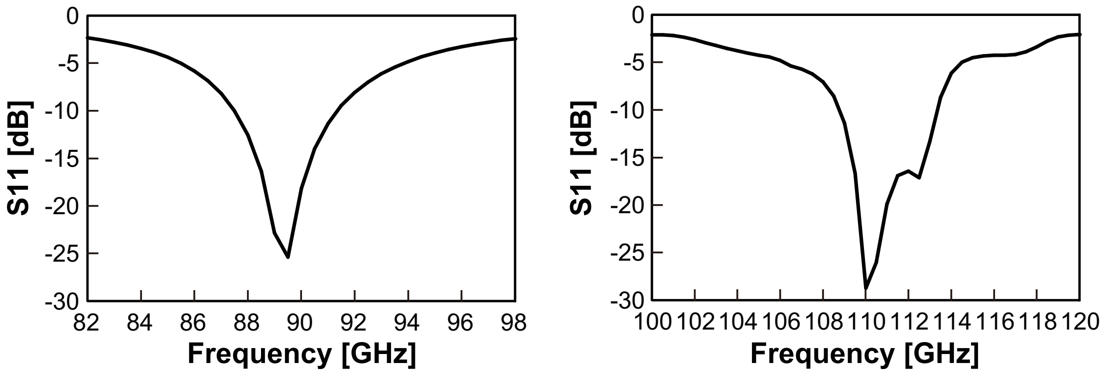

(c) 90 GHz (d) 110 GHz

Fig. 3.23. Simulation results for reflection coefficient S11 of antenna with horn, lens, and MSA whose design frequencies were (a) 60 GHz, (b) 76.5 GHz, (c) 90 GHz, and (d) 110 GHz.

the radiation and reflection performance of the antennas with different design frequencies were comparable, the proposed antenna with a horn, lens, and MSA has versatility on design frequency for providing the high antenna gain and wide matching frequency bandwidth.

3.8 Conclusion

A high-gain antenna fed with a microstrip line of LRRs for automotive applications using the 77-GHz band has been investigated. An antenna with a pyramidal horn, dielectric lens, and horn-to-microstrip transition composed of a single MSA as a matching element was proposed in order to achieve a high antenna gain and to reduce the area of the antenna substrate. Measurement results for a fabricated antenna with a substrate less than 20 × 20 mm showed that it had an antenna gain of 23.5 dBi. In principle, the required size of the antenna substrate can be reduced to 4 × 2 mm which is equivalent to the input-aperture size of the horn. The antenna had HPBWs of 4.5 and 16 degrees in elevation and azimuth, respectively. The antenna achieved a matching frequency bandwidth of 4 GHz, meaning that it has a high tolerance to frequency variations caused by size deviation of the MSA during fabrication.

To obtain a high tolerance to misalignment of the horn and MSA, a new horn-to-microstrip transition was proposed in which the opening of the ground pattern around the MSA is smaller than the input aperture of the horn. Measurement results showed that an antenna with the proposed horn-to-microstrip transition provided a gain degradation of less than 0.2 dB and beam-tilt angles of less than 0.6 and 0.7 degrees in elevation and azimuth, respectively, where the horn was misaligned with the MSA by 0.1 mm. The gain degradation and beam-tilt angles were small enough compared with the antenna gain and HPBW. Thus, the proposed antenna had a high tolerance to misalignment of the horn and MSA due to mechanical deviation during production.

Moreover, simulation results showed that the proposed antenna designed to apply it to frequencies of 60, 90, and 110 GHz provided the comparable antenna gains of 23.7, 23.7, and 23.9 dBi for the design frequency of 60, 90, and 110 GHz, respectively. The simulation results for the HPBWs of those antennas were 5 and 16 degrees in elevation and azimuth, respectively, which are also comparable to those in the antenna whose design frequency was 76.5 GHz. The simulation results showed that antennas whose design frequencies were 60, 76.5, 90, and 110 GHz had the relative matching frequency bandwidth of 4.1%, 4.3%, 4.3%, and 4.2%, respectively. Since the simulation results for the radiation and reflection performance of the antennas with different design frequencies were comparable, the proposed antenna with a horn, lens, and MSA had versatility on design frequency for providing the high antenna gain and wide matching frequency bandwidth.

References

[3.1] Y. T. Lo and S. W. Lee, “Antenna Handbook Theory, Applications, and Design,” Springer Science+Business Media, New York, 1988.

[3.2] H. Yi, S.-W. Qu, K. B. Ng, and C. H. Chan, “3-D Printed Discrete Dielectric Lens Antenna with Matching Layer,” in *Proc. of the Int. Symp. on Antennas and Propag. Conf.*, pp. 115–116, Dec. 2014.

[3.3] N. T. Sönmez and N. T. Tokan, “Effects of antireflective coatings on scanning performance of millimetre-wave lenses,” *IET Microw., Antennas and Propag.*, vol. 10, issu. 14, pp. 1485–1491, Nov. 2016.

[3.4] E. Hecht, “Optics (5th ed.),” Pearson Education Ltd., 2016.

[3.5] C. A. Balanis, “Antenna Theory, Analysis and Design (3rd ed.),” John Wiley & Sons Inc., 1997.

Chapter 4

Downsizing of Antennas for Compact Long-Range Radars

4.1 Introduction

To improve the gain while keeping the antenna substrate small, a new antenna structure with a single MSA, horn, and lens was proposed in which the antenna and MMICs can be integrated on the same side of the substrate as described in Chapter 3. The antenna had a high gain and small mono-layer substrate, but the horn height was problematic. A new antenna structure with low-height horn and lens is thus required.

Moreover, an antenna isolation is important for reducing the sizes of a substrate and projected area of a front-end module while keeping the accuracy of DOA estimation in the phase-shifted monopulse method as described in Section 2.4.5. Here, the projected area is the area of the module seen from the boresight, which should be small to make the face of LRRs small.

This chapter presents the detailed design of a new antenna structure comprising a low-height lens horn antenna fed by a single MSA with a high gain and small antenna substrate. It also discusses the isolation of a lens horn antenna array for an Rx that can be applied to a small front-end module for a compact LRR. First, the techniques for reducing the height of the lens horn antenna and for optimizing its structure are described in Section 4.2. Next, the structure of the newly proposed small front-end module and the antenna isolation (especially Rx-Rx) are described and discussed in Section 4.3. Then, the measurement results for a prototype of the proposed antenna structure are presented in Section 4.4. Moreover, versatility of the proposed lens horn antenna is discussed in Section 4.5. Finally, the key points are summarized in Section 4.6.

4.2 Low-height antenna with horn and lens

4.2.1 Technique to reduce height of horn and lens

The first step in reducing the height of a horn and lens antenna with a high gain and small antenna substrate for a Tx is to shorten the focus distance of the dielectric lens. This is because the height of the antenna depends on the focus distance for a reduced-height design in which the focus distance is much less than the height of an optimum horn [3.1]. Therefore, shortening the focus distance is an effective way to reduce the height.

Fig. 4.1(a) shows a cross section in the YZ-plane of the previous design of a horn and lens antenna, where H and D are the height of the horn and diameter of the lens, respectively. The length of the output-aperture of the horn is the same as the diameter of the lens. The MSA is fed through a feed line passing through a slot in the input-aperture of the horn, as shown in the inset. Two techniques for reducing the height of the horn by $1/n$ by shortening focus distance L_F are illustrated in Figs. 4.1(b) and (c). The one in (b) (hereafter technique (b)) uses a lens with focus distance L_F/n and lens diameter D. The one in (c) (hereafter technique (c)) arranges n sets of a lens and horn in the Y direction; the focus distance is L_F/n, the lens diameter is D/n, and the output-aperture length of the horn is D/n.

The shape of the lens is described by the equation (3.2). According to this equation, the lens in technique (b) is much thicker at its center than that in the previous design whereas that in technology (c) is $1/n$, meaning that it is as thin as that in the previous design. Therefore, with technique (b), the antenna gain degrades due to the large curvature of the lens surface even though both techniques have the same whole output-aperture length of D.

The simulated dependence of the gain degradation and reflection coefficient S11 on the focus distance with technique (b) are plotted in Fig. 4.3 (the gain at each focus distance was normalized by that at a focus distance of 40 mm). The simulations were done using ANSYS HFSS$^{\text{TM}}$. The parameters for materials such as lenses and horns used in the simulation are the same as listed in Table 3.1. The results show that the antenna gain degrades about 10 dB when the focus distance is reduced from 30 mm to 15 mm. The gain degradation is caused by reflection on the input surface of the lens as illustrated on the right side of Fig. 4.1(b); near the edge of the lens, the transmission of a radiated wave from the MSA is much smaller than the reflection due to the deep incident angle of the wave on the lens surface [2.36]. Since the S11 of less than -13 dB in the sweep range of the focus distance is small enough, the S11 does not affect the gain. Contrary to technique (b), technique (c) does not have the large reflection on the lens surface around its edge due to the curvature of the lens

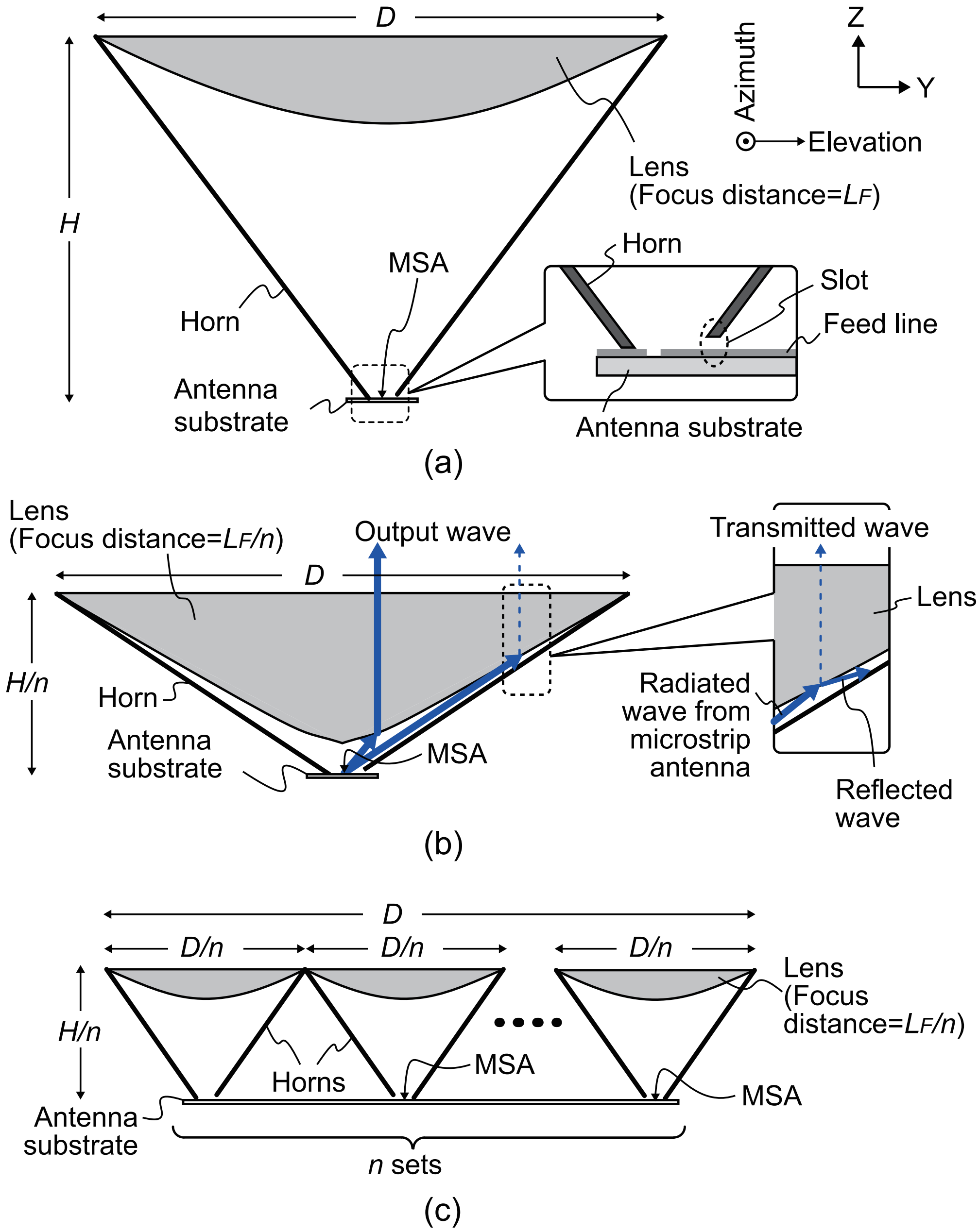

Fig. 4.1. Techniques used to reduce height of horn and lens antenna: (a) previous design with single horn, lens, and MSA, (b) low-height antenna with single horn, lens, and MSA, and (c) low-height array antenna with n sets of horn, lens, and MSA.

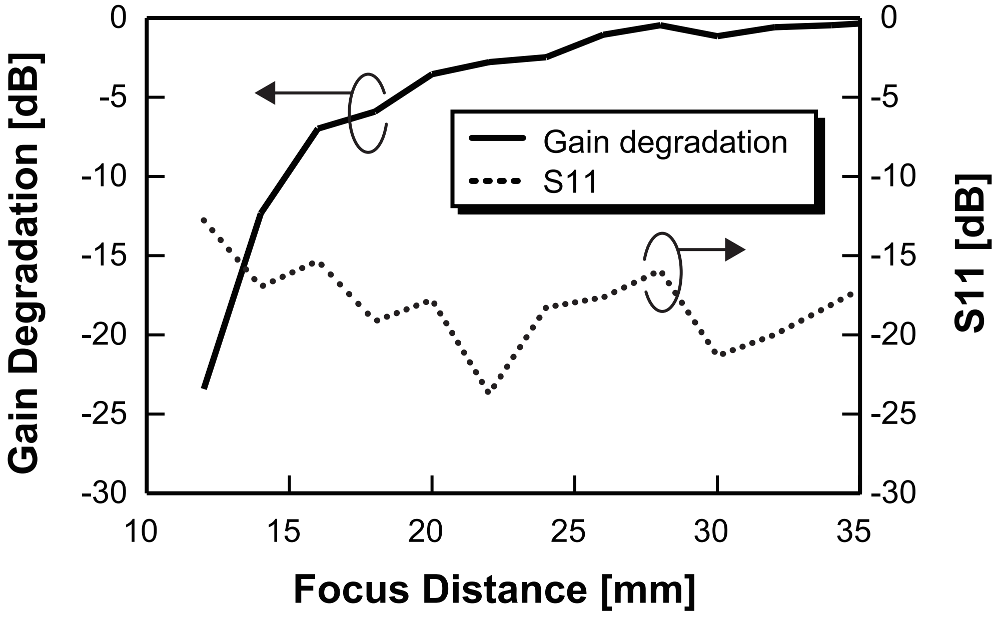

Fig. 4.2. Simulated dependence of gain degradation and reflection coefficient S11 on focus distance with technique (b).

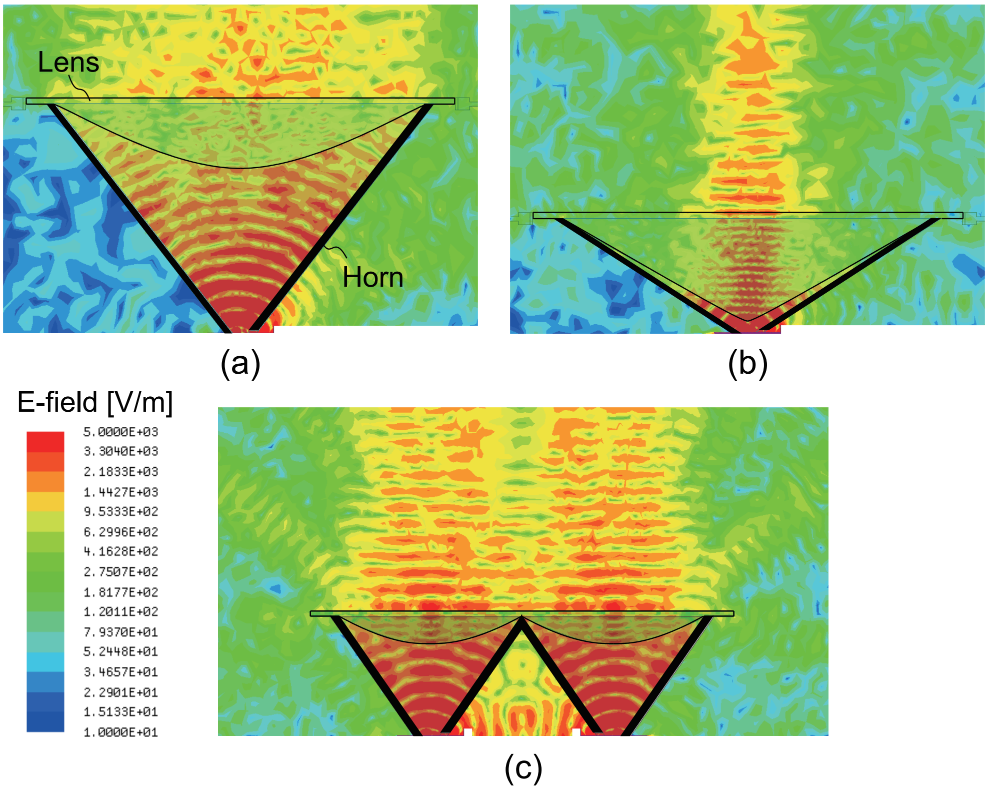

(a)

(b)

(c)

Fig. 4.3. Simulated results for magnitude of electric field in (a) previous design, (b) technique (b) in Fig. 4.1(b), and (c) technique (c) in Fig. 4.1(c).

surface being almost the same as that in the previous design. Fig. 4.3 shows simulated results for the maximum magnitude of electric field (ComplexMag_E in HFSS$^{\mathrm{TM}}$) in three structures of antennas: (a) the antenna described in Chapter 3, (b) antenna with technique (b), and (c) antennas with technique (c). Figs. 4.3(a) and (c) show that the antennas radiate electric wave from almost whole areas of the output-apertures, whereas Fig. 4.3(b) shows that the radiated electric wave is limited in the center of the output-aperture. According to the above simulation results, we used technique (c) in this study.

The next step is optimizing dividing value n considering both feed loss and antenna substrate size. It is important to reduce the transmission loss between the antenna and MMICs when designing the front-end module as well as to improve the antenna gain because feed-line transmission loss degrades antenna output power. The output power of the MMICs cannot be increased in this millimeter-wave application due to the characteristics of semiconductor devices (break-down voltage, heat dissipation, etc.). It is also important to reduce the number of feed elements with high-frequency sensitivity to improve robustness against production deviations such as errors in the etching of metal patterns on the substrate. Fig. 4.4 shows a series of horn and lens array structures with reduced height, considering connectivity to MMICs. The thin solid lines indicate the structure of a horn with an input-aperture $W_i \times L_i$ and a total output-aperture $W_o \times L_o$. The thick solid lines indicate metal patterns on the substrate such as those for MSAs, feed lines, baluns, phase shifters, and dividers. Squares with dotted lines indicate the MMICs, and rectangles with dashed lines indicate the required antenna substrate size ($W_s \times L_s$ at a minimum). Since the power amplifiers in Tx MMICs commonly have differential outputs to achieve high output power [1.35], a balun is required in structure (a). In structures (b), (c), and (d), MSAs are used to drive the array antenna with differential signals. Their E-planes are indicated in Fig. 4.4(b) by thick arrays. The feed points of the MSAs are directly connected to the differential outputs of the MMIC to reduce feed loss and improve robustness.

The lens is cylindrical with parabolic and flat profiles in the Y and X directions, respectively [2.36]. The shape of the radiated wave in the Y direction is transformed from spherical to plane by the lens while that in the X direction is transformed by the horn. Therefore, the flare angle in the Y direction should be smaller than that in the X direction. For the total output-aperture size (18 × 44 mm), the divided configurations of the antenna are those shown as Fig. 4.4. As shown in the figure, the size of the antenna substrate, the length of the feed lines, and the number of dividers and phase shifters increase as the horn height is reduced. Fig. 4.5 shows the dependence of the required area for the antenna substrate and the feed loss between the MMIC and

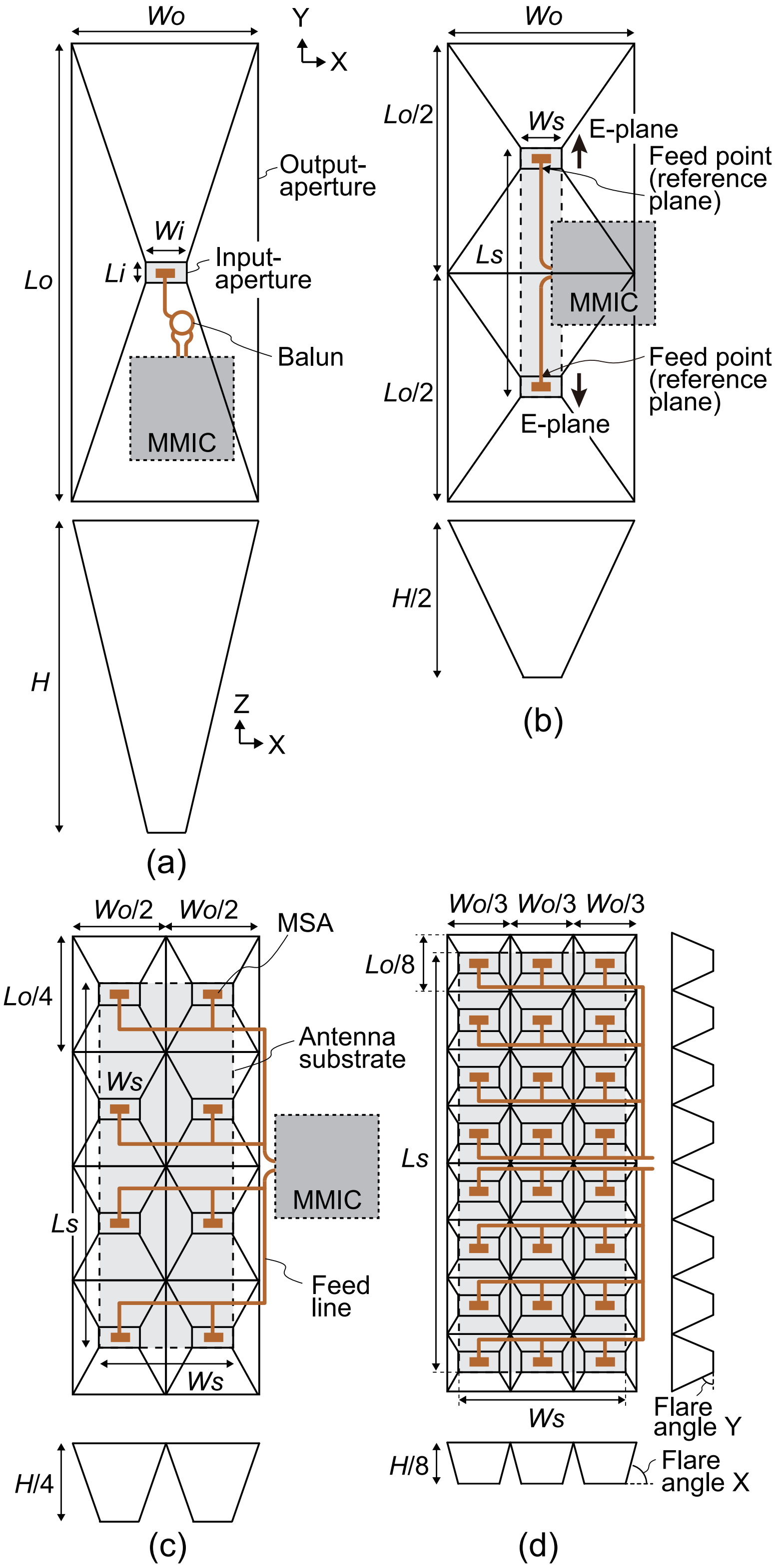

Fig. 4.4. Structures of horn and lens array with reduced height, considering connectivity to MMICs: (a) previous design, (b) half height, (c) quarter height, and (d) 1/8 height.

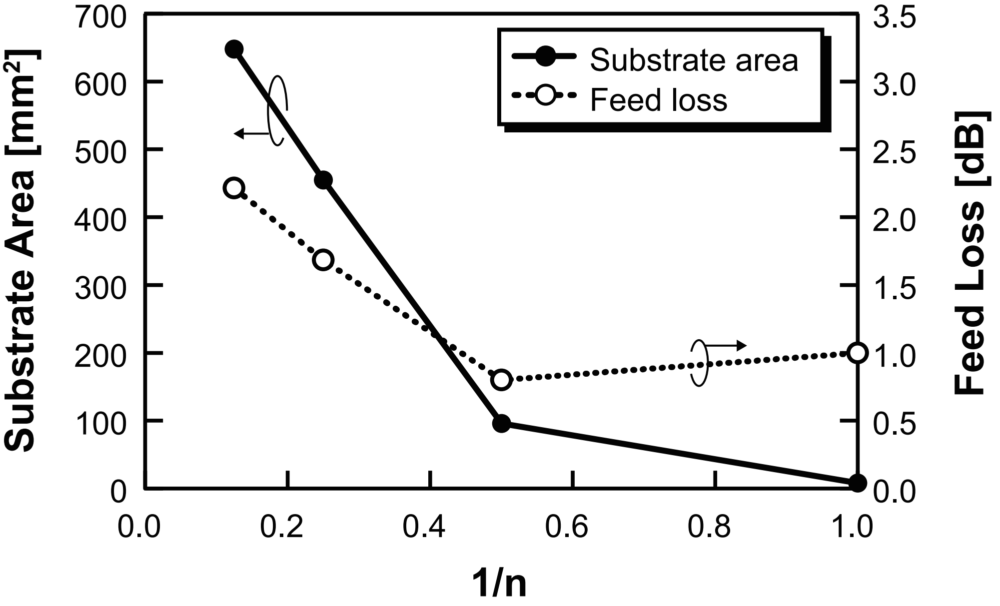

Fig. 4.5. Dependence of required area for antenna substrate and feed loss between MMIC and MSAs on dividing value n.

the MSAs on dividing value n. Feed loss is the mean value of the transmission loss between the MMIC and each MSA. The balun, microstrip line, and divider losses used in the calculation were 1 dB, 0.8 dB/cm, and 0.3 dB, which were obtained by simulation using the Rogers RO3003 substrate with a dielectric constant of 3.2 and $\tan\delta$ of 0.004. The size of the antenna substrate and feed loss increase drastically when n is greater than 4, so a dividing value of 2 was used in this study.

4.2.2 Simulation results for low-height horn and lens antenna

The simulated radiation pattern at 76.5 GHz and the simulated reflection coefficient S11 for the proposed low-height horn and lens antenna with two differential arrays are plotted in Fig. 4.6. Reference planes of the characteristics were placed on the feed lines at the slots of the horns as indicated in Fig. 4.4(b). The sizes of the output and input-apertures of the horn ($W_o \times L_o$ and $W_i \times L_i$) were 18 $\times$ 44 and 4 $\times$ 2 mm, respectively, and height H was 14 mm. The size of the MSA was 1.38 $\times$ 1.07 mm. A boundary condition under the antenna substrate was Al to have the same condition as measurements detailed in Section 4.4.1. The antenna had a gain of 23.2 dBi and HPBWs of 5 and 19 degrees in elevation and azimuth, respectively. The antenna provided the S11 of less than -16 dB in the 77-GHz band. These results demonstrate that the proposed low-height horn and lens antenna can provide almost the same performance as one with the previous design described in Chapter 3. Moreover, the required size of the antenna substrate ($W_s \times L_s$) is 4 $\times$ 24 mm, which is 1/8 that of

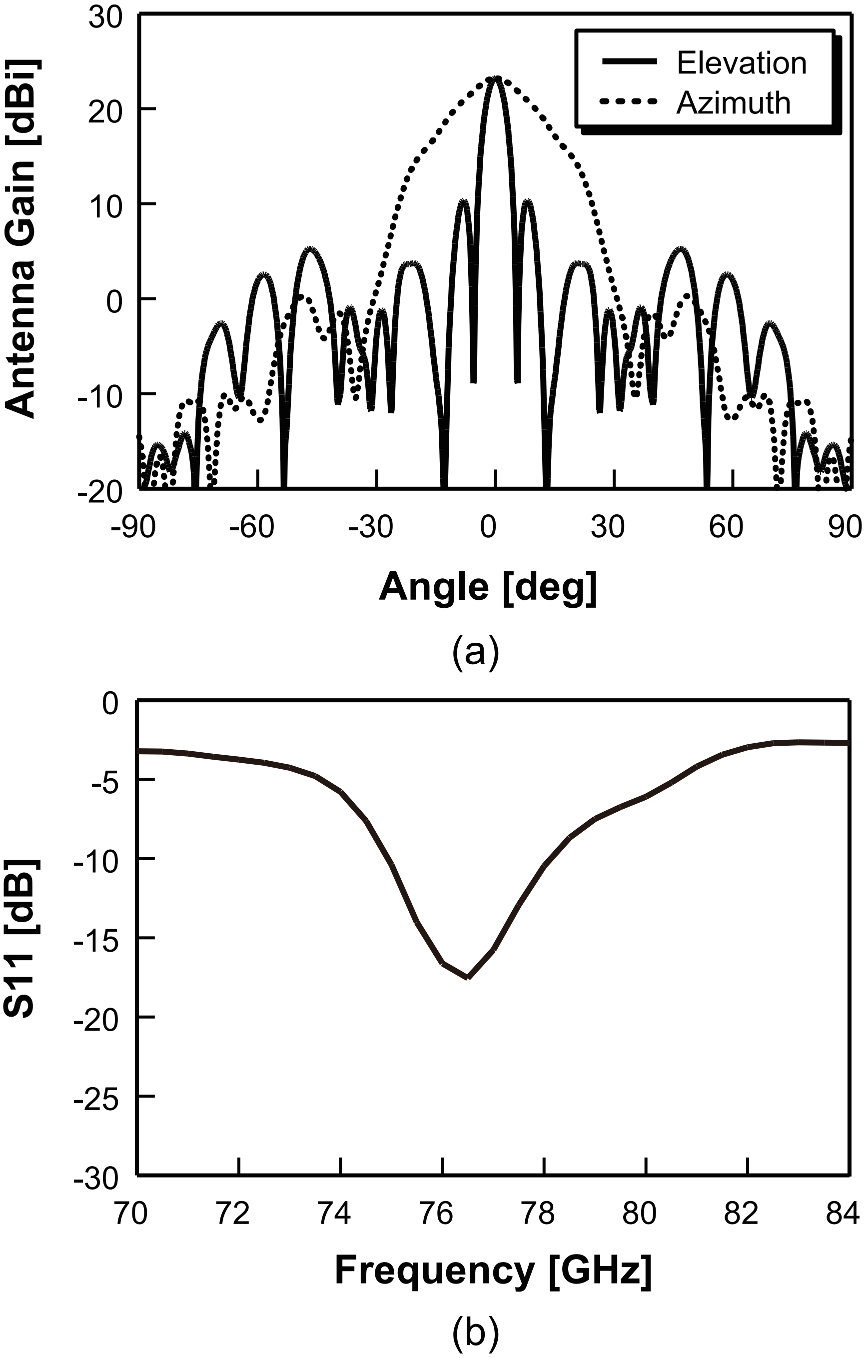

Fig. 4.6. Simulated (a) radiation pattern at 76.5 GHz and (b) reflection coefficient S11.

the output-aperture of the antenna.

4.3 Isolation for high-density antenna integration

In addition to having a high antenna gain and small antenna substrate, high-density integration of antennas with a high antenna isolation is also required to reduce the size of the substrates and projected area of a front-end module for a compact LRR. The gap between Rx antennas in particular should be reduced in order to widen the DOA estimation angle [4.1] while keeping the output-aperture area unchanged in order to maintain high antenna gain. However, achieving high isolation from Rx to Rx is more difficult than that from Tx to Rx. Moreover, reducing the gap degrades the isolation. In contrast, the isolation from Tx to Rx can be increased by extending the distance between Tx and Rx antennas. Therefore, a method for achieving high antenna isolation without gap between Rx antennas was developed.

Fig. 4.7 illustrates the concept of the newly proposed structure for the front-end module. It uses a transceiver with one Tx antenna and a four-channel Rx antenna array to estimate the DOA by the phase-shifted monopulse method [1.33]. The proposed low-height horn and lens antenna is used as the Tx antenna with an output-aperture area of $W_{ot} \times L_o$. The Rx antenna array is composed of four unit antennas with the same output-aperture area ($W_{or} \times L_o/2$). The antennas are arranged two-by-two without gap, and the MSA of each one is connected to one of the four input terminals of the MMIC mounted in the shaded area of the tapered part of the horns. The configuration of the front-end module provides a small projected area which is almost the same as a total output-aperture area of Tx and Rx antennas. The azimuth DOA estimation (X direction) is done by comparing the phase differences of the received signals between Ch1 and Ch2 or between Ch3 and Ch4 using the phase-shifted monopulse method. Therefore, in the configuration of Rx antennas and an MMIC described above, low antenna coupling between Ch1 and Ch2 (hereafter ANT-1 and ANT-2, respectively) or between Ch3 and Ch4 (hereafter ANT-3 and ANT-4, respectively) is required to improve DOA estimation accuracy.

The simulated antenna isolation between the ANT-1 and ANT-2 and the simulated reflection coefficient S11 are shown in Fig. 4.8. The output-aperture of the horn ($W_{or} \times L_o$/2) was 9 $\times$ 22 mm, height H was 14 mm, and the other elements in the horn and lens antenna were the same as those described in Section 4.2. The values were optimized considering the gain and beamwidths. The proposed Rx antenna array had an antenna isolation of greater than 42 dB and S11 of less than -11 dB in the 77-GHz band, where the positions of the reference planes for the characteristics were the same as those in the Tx antenna as indicated in Fig. 4.7. The simulated S11 is

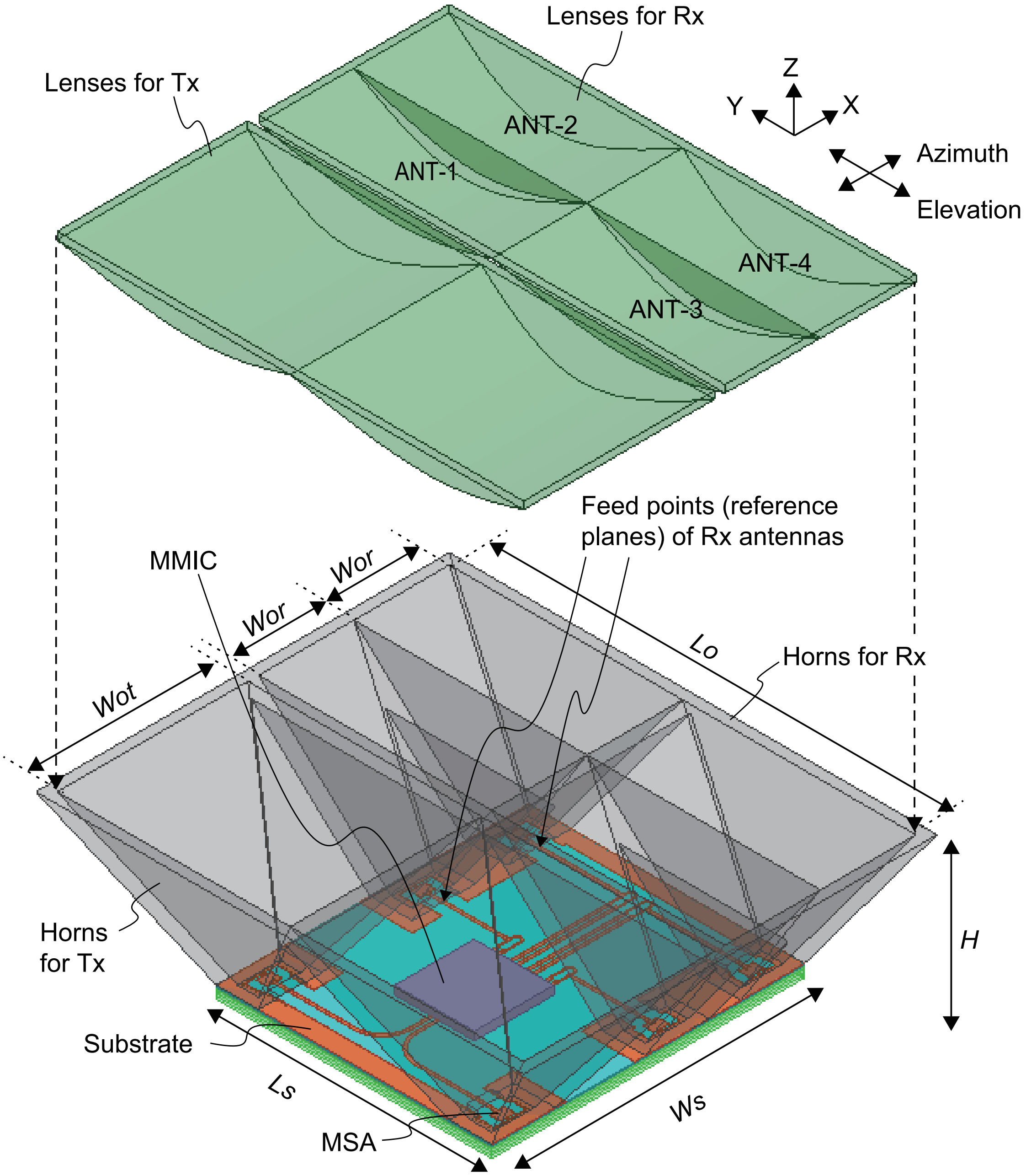

Fig. 4.7. Concept of proposed structure for front-end module with one Tx and four Rx antennas in compact LRR.

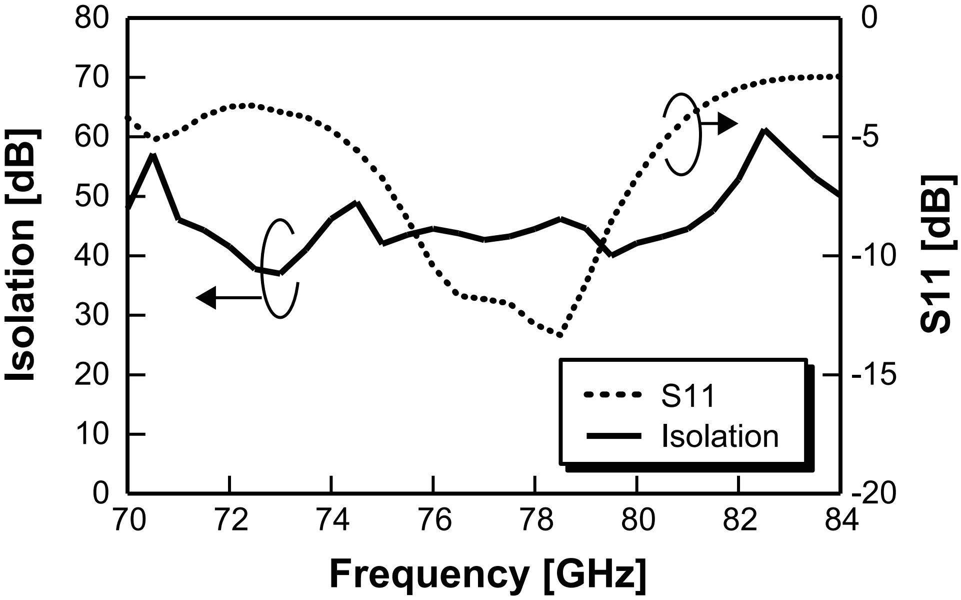

Fig. 4.8. Simulated antenna isolation and reflection coefficient S11.

acceptable because the Rx antennas are connected to the MMIC by using feed lines with transmission loss of 1 to 2 dB in the front-end module.

To analyze the cause of the high isolation, we simulated an electric field of Rx antennas at 76.5 GHz as shown in Fig. 4.9 where only the ANT-1 was activated; the other antennas were connected to 50Ω loads. The high antenna isolation is caused by two mechanisms as shown in Fig. 4.9(a): 1) beam focusing by the horn for ANT-1 where only a diffracted wave leaks into the horn for ANT-2 as indicated by dotted line with arrow and 2) transmission loss in the horn for ANT-2 due to phase disorder by reflection on the surface of the horn as indicated by dashed oval. Moreover, Fig. 4.9(b) shows that maximum magnitudes of electric field are 13925 and 166 V/m at points A and B, respectively, where the point A has the largest magnitude near the center of the MSA and the point B has the same relative position to the MSA as the point A. A degradation ratio of the magnitude from the point A to B is −38 dB, whose level is equivalent to an isolation of 39 dB without loss of horn-to-microstrip transitions (1.5 dB per channel as listed in Table 3.2). Thus, the isolation can be roughly explained by the magnitude. Furthermore, integral values of the magnitude in the output-apertures of the horns (indicated in Fig. 4.9(b)) were calculated to roughly estimate the effect of the former mechanism. The integral value of the magnitude of ANT-2 was 16 dB smaller than that of ANT-1, which meant that the effect of the former mechanism to the isolation was 16 dB. The remaining 22 dB was mainly caused by the latter mechanism, since transmission loss of the horn for ANT-1 is small. The results indicate that the influence of the latter mechanism is greater than that of the former one to provide the

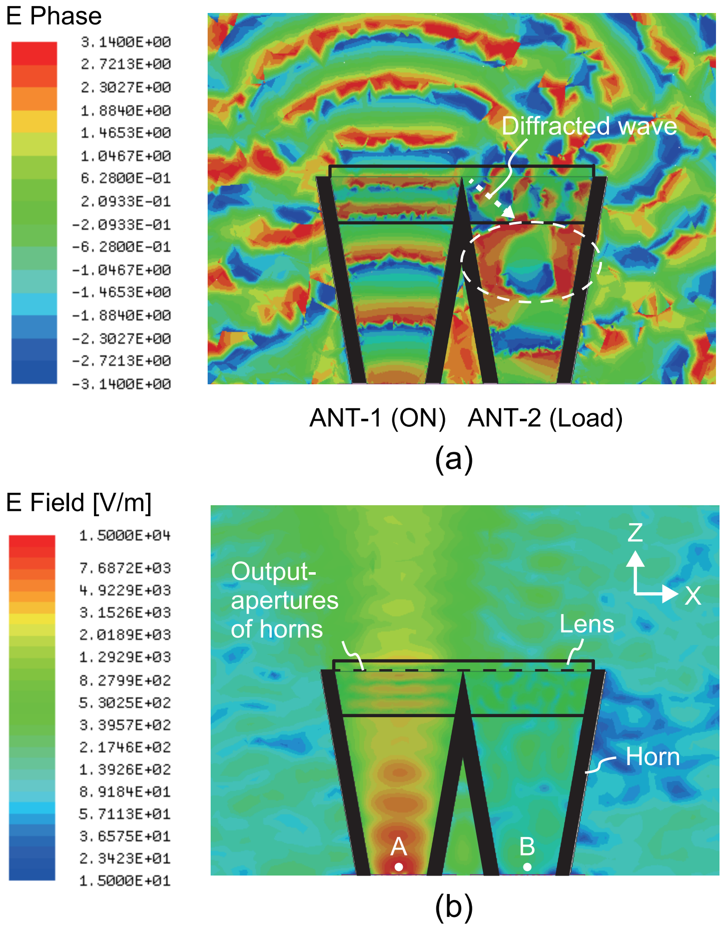

Fig. 4.9. Simulated (a) snapshot of phase and (b) maximum magnitude of electric field in ZX-plane at 76.5 GHz.

high isolation.

4.4 Fabricated antennas and measurement results

4.4.1 Fabricated antennas

Perspective and top view photographs of a fabricated low-height horn and lens Tx antenna are shown in Fig. 4.10. The output-aperture size $W_{ot} \times L_o$ and height were 18×44 mm and 14 mm, respectively. Perspective and top view photographs of a fabricated horn and lens Rx antenna array are shown in Fig. 4.11. The output-aperture size $W_{or} \times L_o/2$ and height of the unit antenna were 9×22 mm and 14 mm, respectively. The diameters and focus distance of each lens were 22 and 16 mm for both the Tx and Rx antennas. Al and PPS were used as the materials for the horns and lenses, respectively, in consideration of material cost. Since Al and

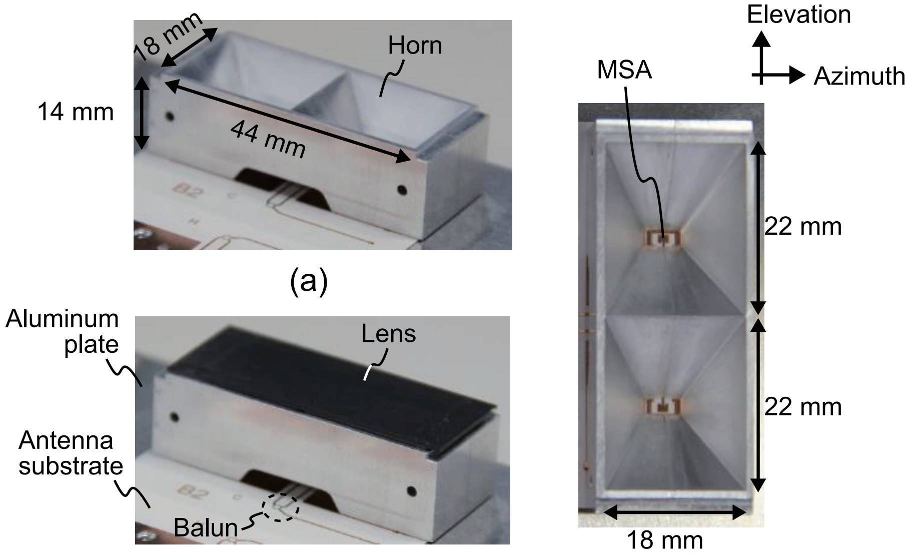

(a) (b) (c)

Fig. 4.10. Photographs of fabricated low-height horn and lens antenna for Tx: (a) and (b) perspective view without and with lens, respectively; (c) top view without lens.

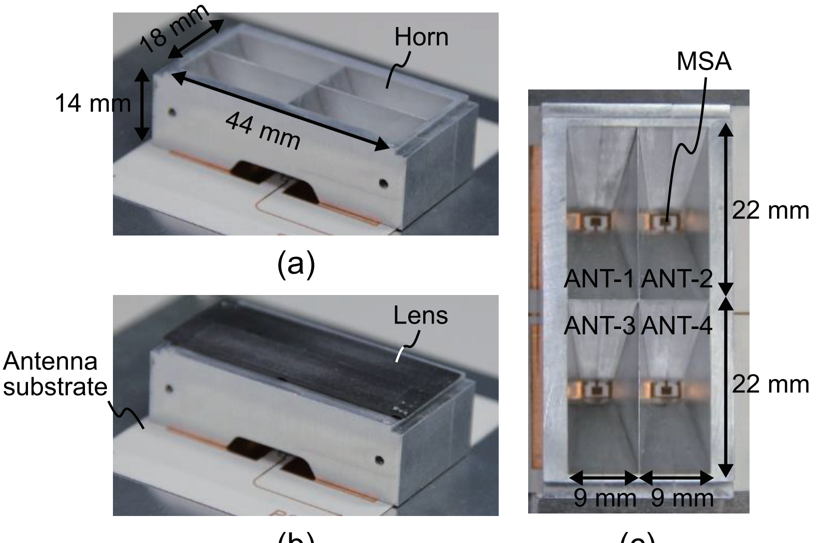

(a) (b) (c)

Fig. 4.11. Photographs of fabricated low-height horn and lens antenna array for Rx: (a) and (b) perspective view without and with lens, respectively; (c) top view without lens.

PPS are commonly used for the frames and radomes of radar devices, the increase in material cost is negligible. A Rogers RO3003 mono-layer resin substrate was used as the antenna substrate. A rat-race balun was inserted into the feed lines of two of the MSAs to measure the radiation pattern of the Tx antenna by using a single-ended spectrum analyzer. In the measurement setup, the antenna substrate was pasted onto an aluminum plate. The horn was fixed to the aluminum plate along with the antenna substrate with screws to form a good electrical contact between the horns and ground patterns designed on the antenna substrate.

4.4.2 Measurement results for Tx antenna

The measured and simulated elevation and azimuth radiation patterns of the proposed low-height Tx antenna at 76.5 GHz are shown in Fig. 4.12. The low-height antenna provided an antenna gain of 23.5 dBi and a flat beam with elevation and azimuth HPBWs of 4.5 and 21 degrees, respectively. The transmission loss of the balun and feed lines was de-embedded. The measurement results are in good agreement with the simulation ones with respect to the major lobes in both directions.

Fig. 4.13 shows the measured reflection coefficient S11 of the fabricated antenna, where a reference plane was placed at the end of a feed line for measurement with transmission loss of 2 dB. It was less than -18 dB in the 77-GHz band, which is small enough for this antenna to be used in a radar sensor. The measured S11 was similar to the simulated one. The small periodical dips with few-GHz periods in the measurement and simulation were caused by an impedance mismatch between the feed line and contact pattern on the antenna substrate used for connecting a GSG (ground-signal-ground) probe [4.2] due to an error in etching of the feed line and contact pattern.

As shown by the comparison in Table 4.1, the height of the horn in the proposed low-height horn and lens antenna was half that with the previous design while maintaining a flat beam and high antenna gain. Although the required substrate area of the low-height antenna was larger than that with the previous design, it was still much smaller than the output-aperture area compared with the previous work [2.13]. Moreover, the differential inputs with the proposed antenna provided high robustness against frequency deviations caused by etching errors, which are problems in mass production, because the antenna did not have feed elements with high frequency sensitivity such as baluns, dividers, and phase shifters.

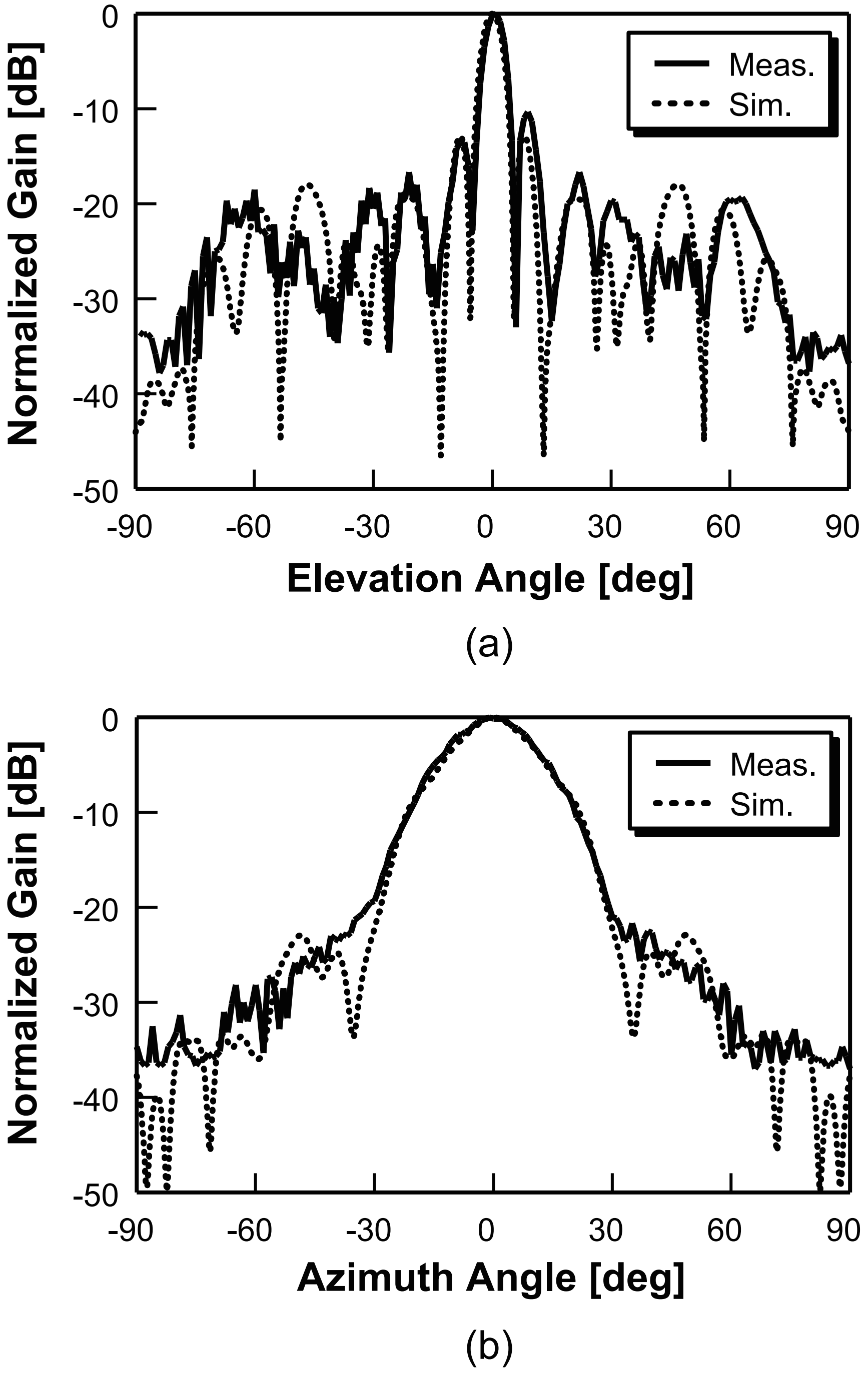

(a)

(b)

Fig. 4.12. Measured and simulated (a) elevation and (b) azimuth radiation patterns at 76.5 GHz for proposed Tx antenna.

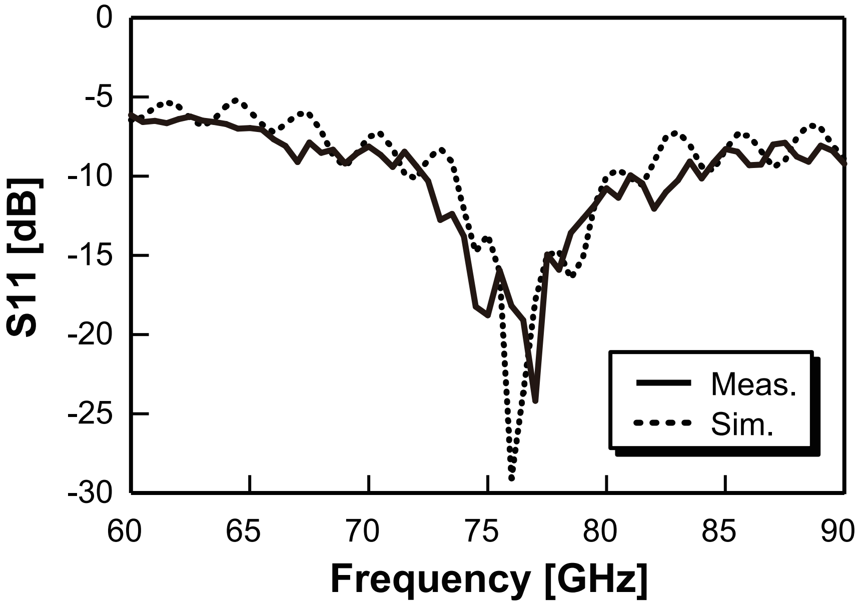

Fig. 4.13. Measured and simulated reflection coefficient S11 of proposed Tx antenna with feed line for measurement.

Table 4.1. Comparison of low-height antenna and previous design.

Item	Low-height antenna	Previous (Chapter 3)	[2.13]
Antenna gain	23.5 dBi	23.5 dBi	22.5 dBi
HPBWs (elevation / azimuth)	4.5° / 21°	4.5° / 16°	4° / 26.3°
Output-aperture area	792 mm^2	810 mm^2	408 mm^2
Horn height	14 mm	29 mm	N.A.
Substrate area (in principle)	96 mm^2	8 mm^2	408 mm^2
Additional feed element except feed line	None	Balun	None

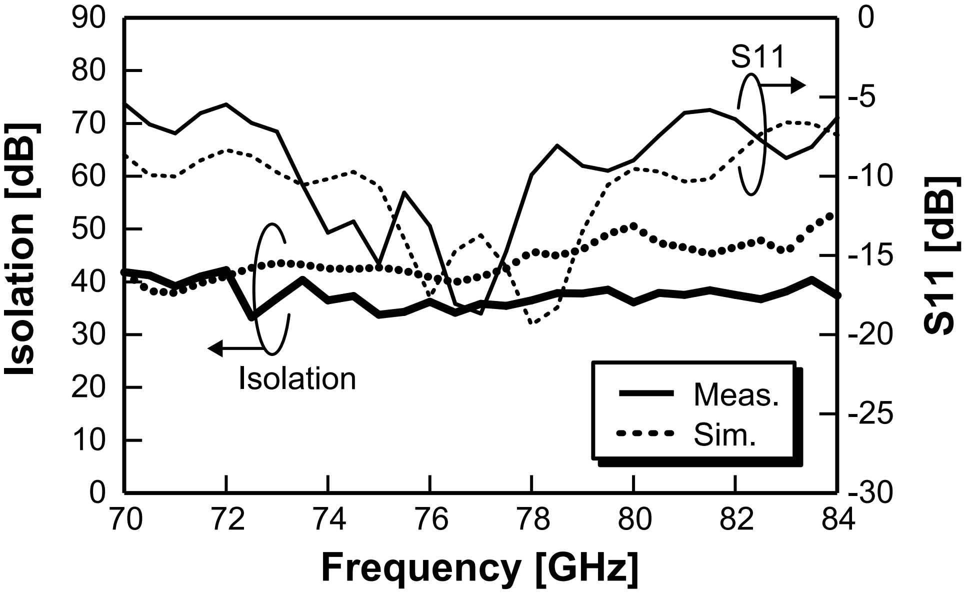

Fig. 4.14. Measured and simulated antenna isolation and reflection coefficient S11 of Rx antenna array with feed lines for measurement.

4.4.3 Measurement results for antenna isolation between Rx antennas

Fig. 4.14 shows the measured and simulated antenna isolation between ANT-1 and ANT-2 (and between ANT-3 and ANT-4) and reflection coefficient S11 of a fabricated Rx horn and lens antenna array, where the reference planes were placed at the ends of feed lines for measurement with transmission loss of 1.5 dB per channel. The simulation was done using an antenna model in which the feed lines were added to the model described in Section 4.3 to provide the same condition as the measurement. The simulated isolation of greater than 40 dB in the 77-GHz band was smaller than that in Fig. 4.8 due to a leaked wave from the slot of the horn (indicated in Fig. 4.1(a)) to the added feed line of the opposite channel as shown in Fig. 4.15. Fig. 4.15 shows the simulation results for the magnitude of electric-field on the antenna substrate at 76.5 GHz without and with a perfectly matched layer (PML) indicated by a dashed rectangle in the figure. The PML was arranged between the antenna substrate and horn to work as an ideal absorber preventing radiation of electric waves from the slot of ANT-1 to the feed line for ANT-2. The magnitude of electric-field at the feed line for ANT-2 (indicated by using dashed oval) was smaller in Fig. 4.15(b) than that in Fig. 4.15(a) due to insertion of the PML between ANT-1 and ANT-2.

The measured isolation was greater than 34 dB in the 77-GHz band. The difference between simulated and measured results may be caused by manufacturing errors, such as an edge roundness of the horns, and simulation errors of few dB due to setting of

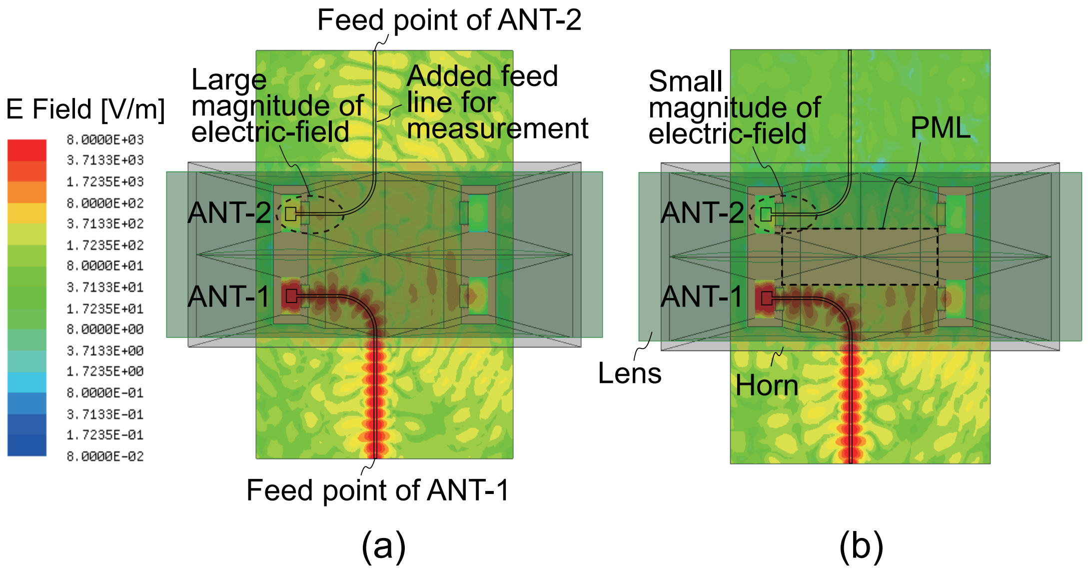

Fig. 4.15. Simulated snapshot of magnitude of electric-field on surface of antenna substrate (a) without and (b) with PML at 76.5 GHz.

a boundary condition. Moreover, a measurement result for an isolation without the feed lines for measurement was 31 dB by de-embedding transmission loss of the feed lines for both channels (1.5 dB×2), which is small enough for this antenna to be used for FMCW radars. The measured S11 was less than −13 dB in the 77-GHz band, which is also small enough for this antenna to be used in a radar sensor. Moreover, the measured S11 was similar to the simulated one. The difference of dip frequency around 77 GHz was caused by an etching error of the MSAs in fabrication. The small periodical dips in the measured and simulated S11 were due to the etching error of the contact patterns explained above.

As demonstrated by the measurement results, the proposed horn and lens Tx and Rx antennas composed of only commercially available materials are applicable to small front-end modules due to their high antenna gain, small antenna substrate, and low antenna coupling.

4.5 Versatility of proposed lens horn antenna on antenna isolation

A design frequency dependence of the antenna isolation between adjacent Rx antennas with horn, lens, and MSA has been investigated as a versatility of the proposed technology in the previous sections. Similar to Section 3.7, the frequency of 60, 90, and 110 GHz were chosen as examples.

In the investigation of versatility, the sizes of the horn, lens, thickness of antenna substrate were changed corresponding to the design frequency using the same method described in Section 3.7. The sizes of output-aperture ($W_o \times D_o$) for the design frequency of 60, 90, and 110 GHz were 11.5 × 28, 7.7 × 18.7, and 6.3 × 15.3 mm, respectively. The arrangement of Rx antennas was the same as shown in Fig. 4.7. Table 4.2 lists the main parameters for the Rx antennas for each design frequency. Loss factors of materials for horn, lens, and antenna substrate were same as Chapter 3 (Table 3.1).

Simulated results for the antenna isolation between Rx antennas arranged in X direction (corresponding to azimuth) and reflection coefficient S11 are shown in Fig. 4.16. Solid and dotted lines indicate the isolation and S11, respectively, in each graph. The simulation used the same parameters of the materials for the horn, lens, and antenna substrate as those listed in Table 3.1. The isolations of each antenna were 46, 42, and 45 dB for the design frequency of 60, 90, and 110 GHz, respectively. The antennas whose design frequencies were 60, 90, and 110 GHz had the S11 of -11, -11, and -13 dB, respectively. Table 4.3 lists the simulated isolation and S11 of antennas at 60, 76.5, 90, 110 GHz whose design frequencies are 60, 76.5, 90, and 110 GHz, respectively. These results showed that the isolation between Rx antennas and S11 of the antennas designed with frequencies of 60, 90, and 110 GHz were comparable to those for the antenna with design frequency of 76.5 GHz.

Since the simulation results for the isolation and reflection performance of the antennas with different design frequencies were comparable, the proposed antenna with horns, lenses, and MSAs had versatility on design frequency for providing the antenna isolation.

Table 4.2. Main parameters of proposed antenna for each design frequency.

Design frequency	60 GHz	76.5 GHz	90 GHz	110 GHz
Output-aperture size [mm]	11.5 × 28	9 × 22	7.7 × 18.7	6.3 × 15.3
Input-aperture size [mm]	5.1 × 2.55	4 × 2	3.4 × 1.7	2.8 × 1.4
Horn height [mm]	17.9	14	11.9	9.7
Lens focus distance [mm]	20.4	16	13.6	11.1
MSA size [mm]	1.74 × 1.34	1.38 × 1.07	1.18 × 0.91	0.96 × 0.74
Substrate thickness [mm]	0.162	0.127	0.108	0.088

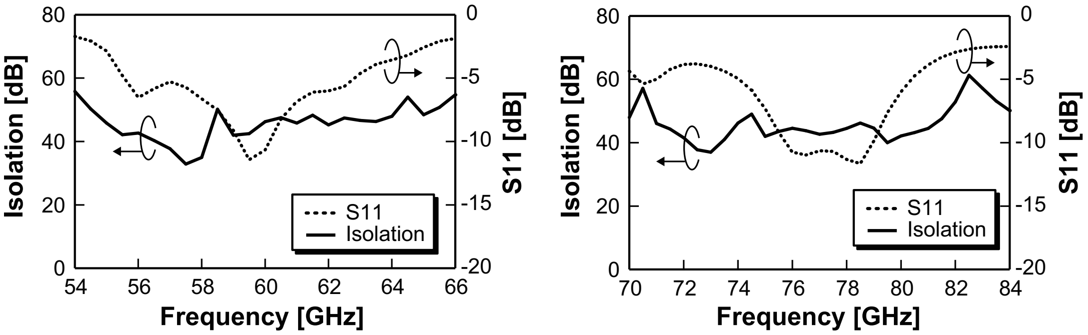

(a) 60 GHz (b) 76.5 GHz

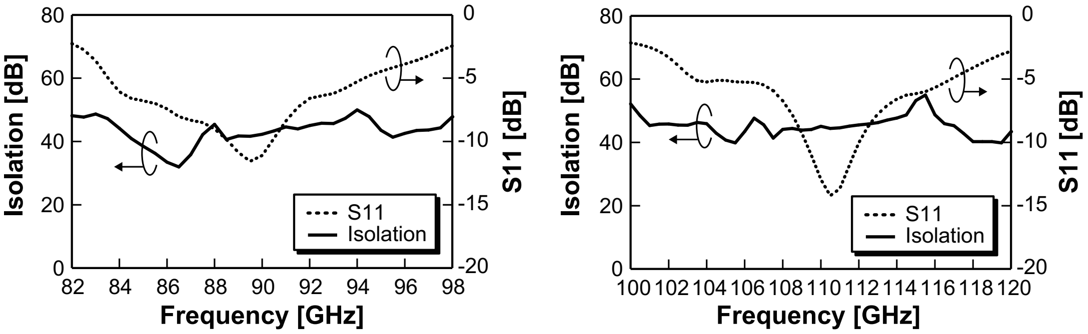

(c) 90 GHz (d) 110 GHz

Fig. 4.16. Simulation results for isolation between adjacent Rx antennas arranged in X direction and reflection coefficient S11, whose design frequencies were (a) 60 GHz, (b) 76.5 GHz, (c) 90 GHz, and (d) 110 GHz.

Table 4.3. Comparison of simulation results for isolation between adjacent antennas arranged in X direction and reflection coefficient S11 at center frequency of each design.

Design frequency	60 GHz	76.5 GHz	90 GHz	110 GHz
Antenna isolation	46 dB	44 dB	42 dB	45 dB
S11	−11 dB	−11 dB	−11 dB	−13 dB

4.6 Conclusion

The presented Tx and Rx antenna structures reduce the size required for LRRs in the 77-GHz band for automotive application due to the use of antennas with a horn, lens, and MSAs. Antenna height was reduced by half while maintaining a high gain by introducing an antenna structure composed of two differential horn and lens arrays with the diameter and focus distance of the lenses half those in the previous design. The MSAs are directly connected to differential outputs of the MMIC.

A Tx antenna, fabricated using commercially available materials, had a height and output-aperture size of 14 mm and 18 × 44 mm, respectively, and achieved an antenna gain of 23.5 dBi and a reflection coefficient S11 with a feed line for measurement of less than -18 dB in the 77-GHz band. The antenna required a substrate 96 mm^2 at a minimum. The antenna had a flat beam with HPBWs of 4.5 and 21 degrees in elevation and azimuth, respectively.

An Rx antenna array composed of four sets of lens horn antennas with an output-aperture size of 9 × 22 mm and a two-by-two array configuration was fabricated for application in a newly proposed small front-end module for a compact LRR. The front-end module has a small substrate and small projected area due to mounting the MMIC in the shaded area of the tapered part of the horns and mounting the Rx antennas without gap. The measurement results for the fabricated Rx antenna array showed that an antenna isolation between the antennas arranged in the direction corresponding to azimuth was greater than 31 dB and the S11 with feed lines was less than -13 dB in the 77-GHz band. The measured isolation is large enough for frequency-modulated continuous wave radars to provide DOA estimation in azimuth using the phase-shifted monopulse method. The simulation results showed that the high isolation was due to the structure of the horn and lens antenna.

As demonstrated by the measurement results, the proposed antennas with a horn, lens, and MSA enable the fabrication of small front-end modules for compact automotive LRRs with azimuth DOA estimation in the 77-GHz band.

Moreover, simulation results showed that the proposed antenna designed to apply it to frequencies of 60, 76.5, 90, and 110 GHz provided an antenna isolation between adjacent Rx antennas arranged in X direction (corresponds to azimuth) of 46, 44, 42, and 45 dB at 60, 76.5, 90, and 110 GHz, respectively. Since the simulation results for the isolation between the Rx antennas with different design frequencies were comparable to that for the Rx antenna with the design frequency of 76.5 GHz, the proposed antenna with horns, lenses, and MSAs had versatility on design frequency for providing the antenna isolation.

References

[4.1] H. Asamuma, Y. Sekiguchi, K. Honda, and M. Kishida, “Front-Side- Looking Millimeter Wave Radar for Front-Side-Pre-Crash Safety System,” *Fujitsu Ten Tech. J.*, no. 34, pp. 33–38, Jan. 2010.

[4.2] T. Jamneala, P. D. Bradley, and D. A. Feld, “Employing a Ground Model to Accurately Characterize Electronic Devices Measured With GSG Probes,” *IEEE Trans. Microw. Theory Tech.*, vol. 52, no. 2, pp. 640–645, Feb. 2004.

Chapter 5

Widening Beamwidth of Antennas for Dual-Range Dual Field-of-View Radars

5.1 Introduction

The newly proposed antenna with horn, lens, and MSA had small antenna substrate while keeping a high antenna gain and high isolation, and could be applied to compact LRRs as described in Chapters 3 and 4. The antenna provided a flat beam where an HPBW in azimuth was much wider than that in elevation; however, the HPBW in azimuth was about ±10 degrees which was about 1/3 narrower than the specification of radiation performance for a middle-range detection (MRR-mode) shown in Fig. 1.12. In this chapter, a new technology to widen the beamwidth of the antenna based on the proposed lens horn antenna fed by a single MSA described in Chapter 3, considering a Tx architecture of dual-range dual-FOV radars.

In this chapter, I first explain two approaches to widen the beamwidth for MRR-mode by using the lens horn antenna, and why a new configuration is required for the Tx antenna structure in Section 5.2. Next, Section 5.3 explains the newly developed architecture for the Tx antenna array. Then, the concept and principle of the proposed antenna array, its limitations, and a novel antenna structure are then described in Section 5.4. The configuration of a Tx antenna suite for LRR- and MRR-modes is described in Section 5.5. The fabricated antennas are described and the measurement results are presented in Section 5.6. Moreover, versatility of the proposed lens horn antenna is discussed in Section 5.7. Finally, the key points are summarized in Section 5.8.

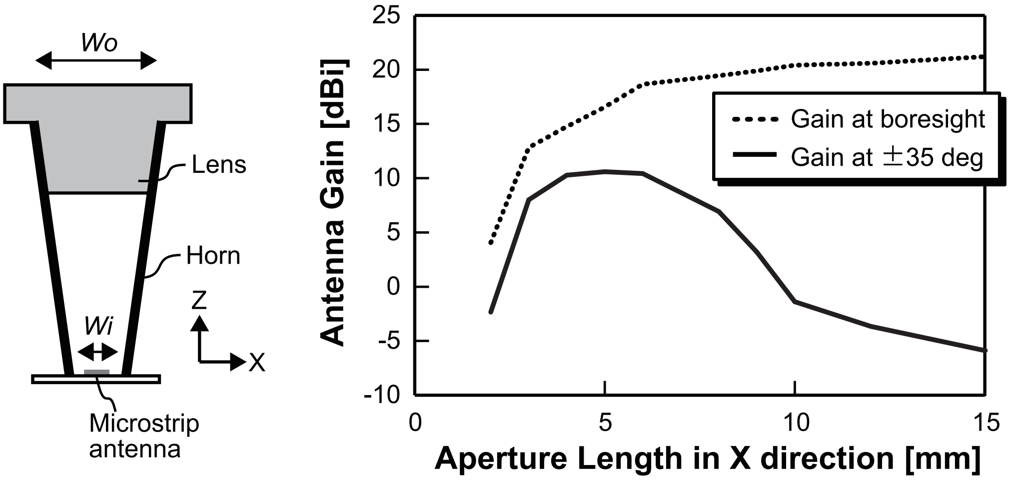

(a) (b)

Fig. 5.1. (a) Cross sectional structure of lens horn antenna in ZX-plane and (b) simulated dependence of antenna gains at boresight and at azimuth angles of ± 35 degrees on output-aperture length of lens horn antenna in X direction at 76.5 GHz.

5.2 Issues on lens horn antenna to widen beamwidth

The detailed design of the lens horn antenna was described in Chapter 3. In this section, an antenna structure for MRR-mode to widen the beamwidth was investigated, which was based on the lens horn antenna and provided a radiation pattern for MRR-mode shown in Fig. 1.12. There are two ways to widen the azimuth beamwidth of the lens horn antenna: shorten the output-aperture length W_o in the X direction or make the output side of the lens concave in the X direction. The output-aperture length W_o and X coordinate are indicated in Fig. 5.1(a).

First, shortening the output-aperture length in the X direction is described.

Fig. 5.1(b) shows the simulated dependence of antenna gains at boresight and at azimuth angles of ± 35 degrees on aperture length W_o at 76.5 GHz. Solid and dotted lines indicate the antenna gain at boresight (corresponds to the maximum gain) and at azimuth angles of ± 35 degrees, respectively.

In the simulation, an output-aperture size (Do) in Y direction was 33 mm which was the aperture length to provide an HPBW of 7 degrees in elevation. The height of the horn was 18 mm which was determined to have a comparable flare angle in Y direction compared with a horn with the output-aperture length Do of 45 mm (discussed in Chapter 3). The input and output-aperture sizes ($L_i \times W_i$ and $L_o \times W_o$) was 2 $\times$ 4. The diameter and focus distance of the lens were 33 and 20 mm, respectively. The sizes of the MSA ($L_A \times W_A$) and the ground pattern ($L_G \times W_G$) were 1.06 $\times$ 1.38 and 1.5 $\times$ 3 mm, respectively. These values were optimized to provide a high antenna

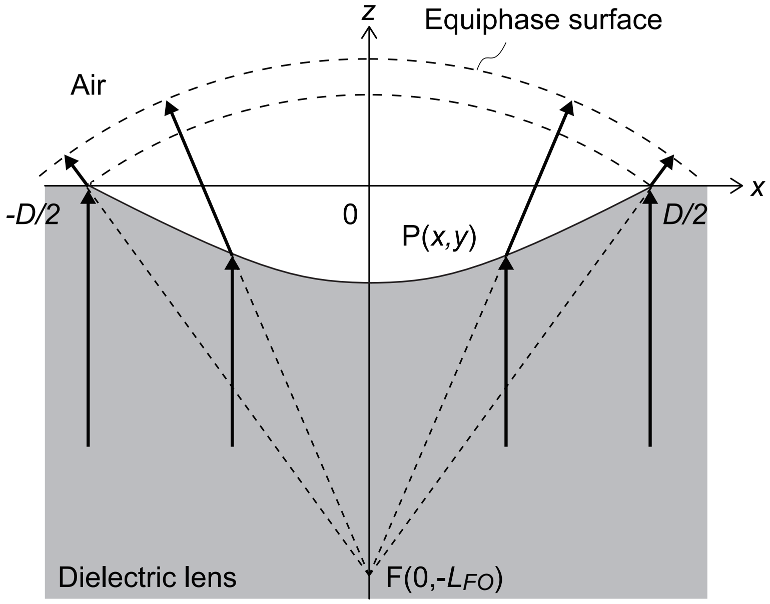

Fig. 5.2. Structure of lens with concave output-aperture used to transform wave shape from flat to spherical.

gain. The materials for the horn and lens were the same as those listed in Table 3.1. The simulation was done by using HFSS$^{\mathrm{TM}}$.

Fig. 5.1(b) showed that the antenna gain at azimuth angles of ±35 degrees increased up to about 10 dBi as the output-aperture length in the X direction became short to 4 mm. In contrast, the gain at boresight decreased to about 16 dBi as the output-aperture length in the X direction became short. Moreover, the both gains were largely degraded when the output-aperture length W_o was less than 4 mm because the W_o became closer to the length that gave the cutoff frequency, where E-plane was paralleled to YZ-plane. According to the simulation results, it is hard to achieve the antenna gain of 15 dBi at azimuth angles of ±35 degrees, meaning that shortening the length of the output-aperture of a single lens horn antenna is not suitable for widening the beamwidth for MRR-mode.

Next, making the output side of the lens concave in the X direction is explained. Fig. 5.2 shows the cross-sectional structure of a concave lens. The lens spreads the waves transmitted through the horn, thereby widening the beamwidth. The shape of the lens in the X direction is described by the following equation [3.1]

$$\begin{cases} z = \dfrac{-B + \sqrt{B^2 - A\left(D^2/4 - x^2\right)}}{A} \\ A = e_r - 1 \\ B = \sqrt{e_r\left(D^2/4 + L_{FO}^2\right)} - L_{FO}, \end{cases} \tag{5.1}$$

where D and L_{FO} are the diameter and focus distance of the concave lens, respec-

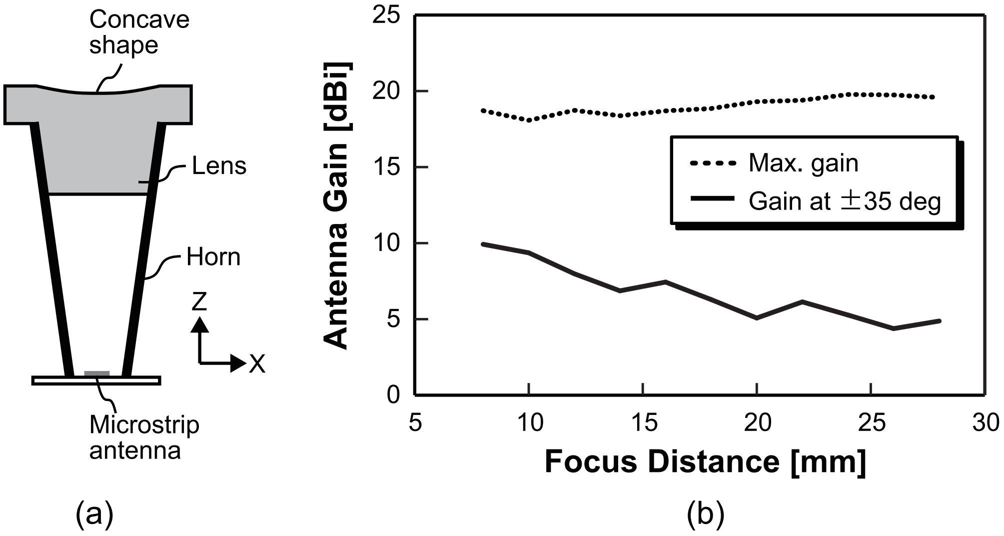

Fig. 5.3. Simulated antenna gain with concave lens at 76.5 GHz: (a) structure of antenna with concave lens based on lens horn antenna; (b) simulated maximum antenna gain and antenna gain at azimuth angles of ±35 degrees.

tively. The x and z coordinates are shown in Fig. 5.2.

Fig. 5.3(a) shows the ZX-plane cross-sectional view of a lens horn antenna with a concave lens, and Fig. 5.3(b) shows the simulated dependence of the maximum antenna gain and antenna gain at azimuth angles of ±35 degrees on the focus distance of the lens. The output-aperture length of the horn and the diameter of the concave lens were both 9 mm. The other parameters for the horn, lens, and MSA were the same as those given in the former way described above. Fig. 5.3(b) shows that the antenna gain at azimuth angles of ±35 degrees increased as the focus distance was shortened; however, the gain was less than 10 dBi, which is less than the target gain. These results indicate that making the output side of the lens concave in the X direction is also not suitable for widening the beamwidth for MRR-mode.

A lens with the concave structure on its input surface also provides the same effect as the lens shown in Fig. 5.3(a). However, such structure requires thicker lens because the lens has parabolic shape in Y direction. Since a thick lens has problem in its production process, the structure was not applied in this study.

Since neither of these methods results in a single lens horn antenna that can provide a radiation pattern with a beamwidth of up to ±35 degrees, a new Tx antenna structure is required. In the following sections, I present our newly developed architecture for such a structure based on the lens horn antenna.

5.3 Architecture of Tx antenna array for dual-range dual-FOV radars

The newly developed architecture for the Tx antenna array includes three sets of antennas, as illustrated in Fig. 5.4. They radiate beams at the boresight, left side, and right side, as shown in Fig. 5.5. The gains of ANT-2 and ANT-3 decrease around an azimuth angle of -10 to 10 degrees while ANT-1 covers that area for MRR-mode. Each antenna is fed by an individual power amplifier (PA) connected to a VCO. The PAs are switched at a certain timing, for example, at the chirp interval for FMCW radars. At the time of writing, MMICs [1.34] with three outputs for transmitters are commercially available. The design of ANT-1 is described in Chapter 3. The technologies used to obtain ANT-2 and ANT-3 are explained in Section 5.4. The proposed antenna array composed of ANT-1, ANT-2, and ANT-3 is described in Section 5.5.

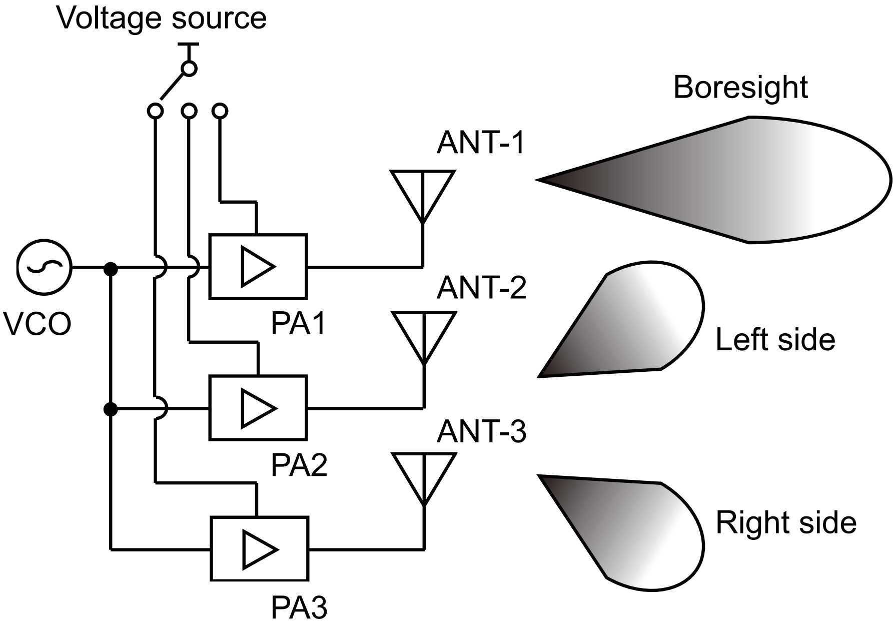

Fig. 5.4. Architecture of proposed Tx with three antennas that radiate beams in different directions.

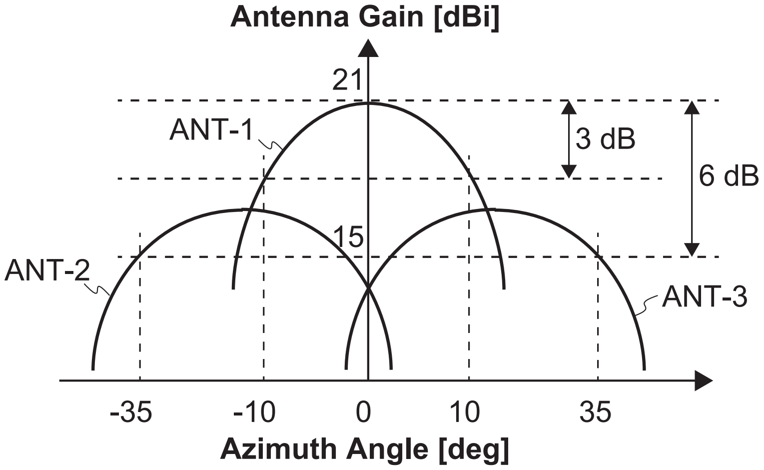

Fig. 5.5. Radiation pattern for dual-range dual-FOV radar obtained by using three types of antennas.

5.4 Structure and principle of lens horn antenna with prism for MRR-mode

This section describes the proposed structure for an antenna based on the lens horn antenna for MRR-mode. First, the concept and principle of the new antenna and its limitations are described in Section 5.4.1. Then, a novel antenna structure is described and discussed in Sections 5.4.2 and 5.4.3, respectively.

5.4.1 Principle of lens horn antenna with prism and its limitations

I propose placing a prism on the output-aperture of the lens to tilt the radiated beam, as illustrated in Fig. 5.6. The prism is placed on the output surface of the lens. Its surface is sloped at a certain angle in order to tilt the beam in the X direction. The angle of the tilt from boresight, $\Delta\theta$, is derived using the Fresnel equation [3.2]:

$$\Delta\theta \, [\mathrm{deg}] = \frac{180}{\pi} \sin^{-1}\left[\sqrt{e_r} \sin \frac{\beta\pi}{180}\right] - \beta, \tag{5.2}$$

where β [deg] is the slope angle of the prism as defined in Fig. 5.6(b). The critical angle of a PPS with a dielectric constant of 4.2 is about 30 degrees, as calculated using the Fresnel equation, so a slope angle of less than 30 degrees is suitable.

I simulated radiation performances of the antenna with a horn, lens, prism, and single MSA by using the ANSYS HFSS$^{\mathrm{TM}}$. The materials for the horn, lens, and antenna substrate were the same as those described in Table 3.1. The input and output-aperture sizes ($L_i \times W_i$ and $L_o \times W_o$) were 2 × 4 and 33 × 9 mm, respectively, and the horn height H was 18 mm. The diameter and focus distance of the lens were 33

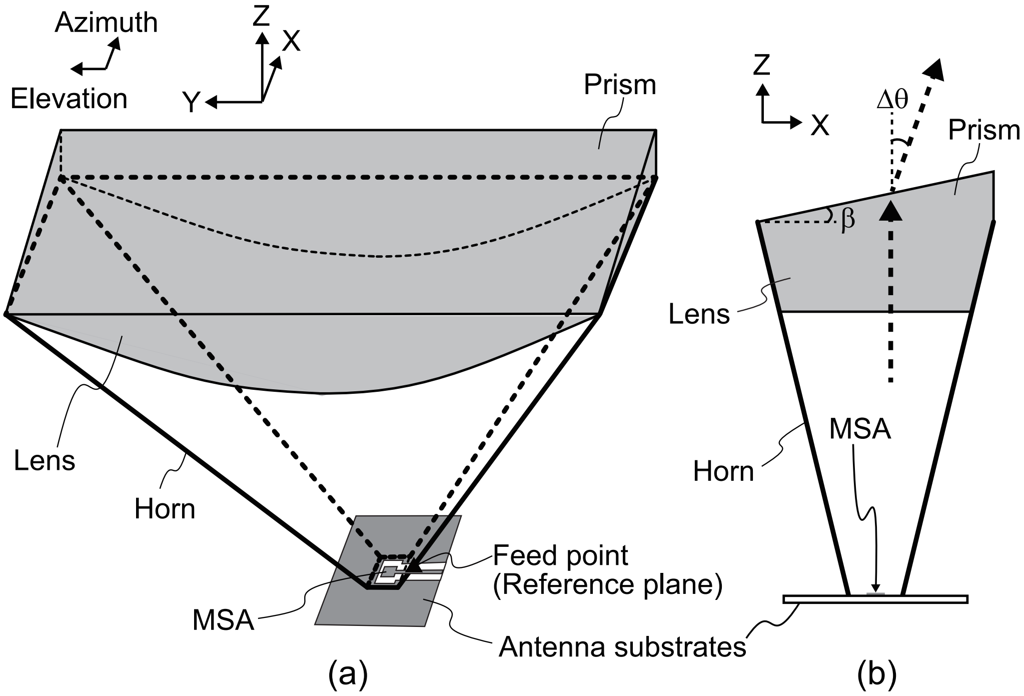

Fig. 5.6. Structure of lens horn antenna with prism: (a) perspective view; (b) ZX-plane cross-sectional view.

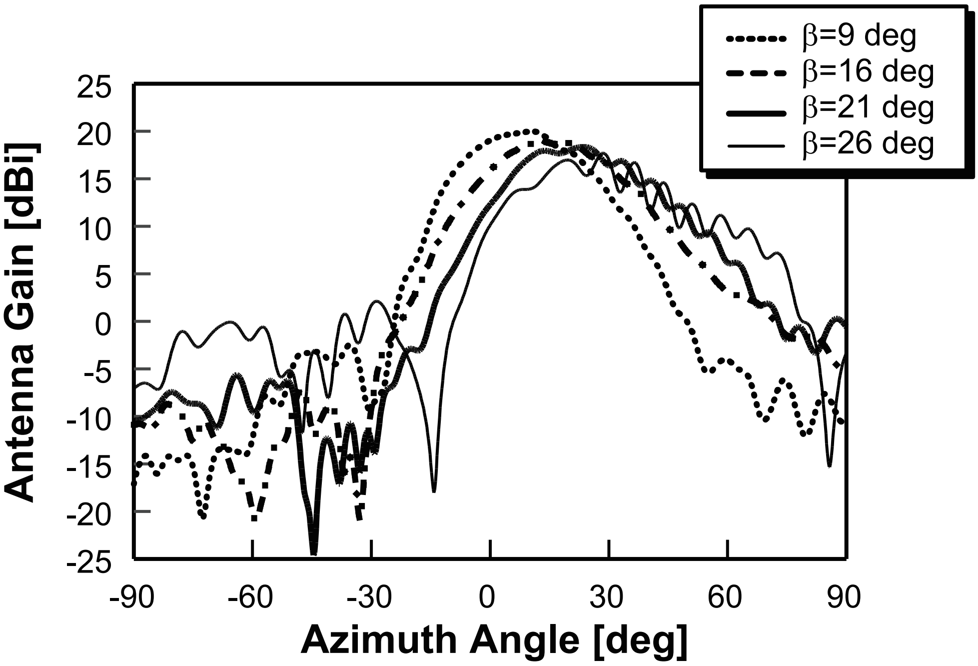

Fig. 5.7. Simulation results for dependence of radiation pattern on azimuth angle of prism for proposed lens horn antenna with prism at 76.5 GHz.

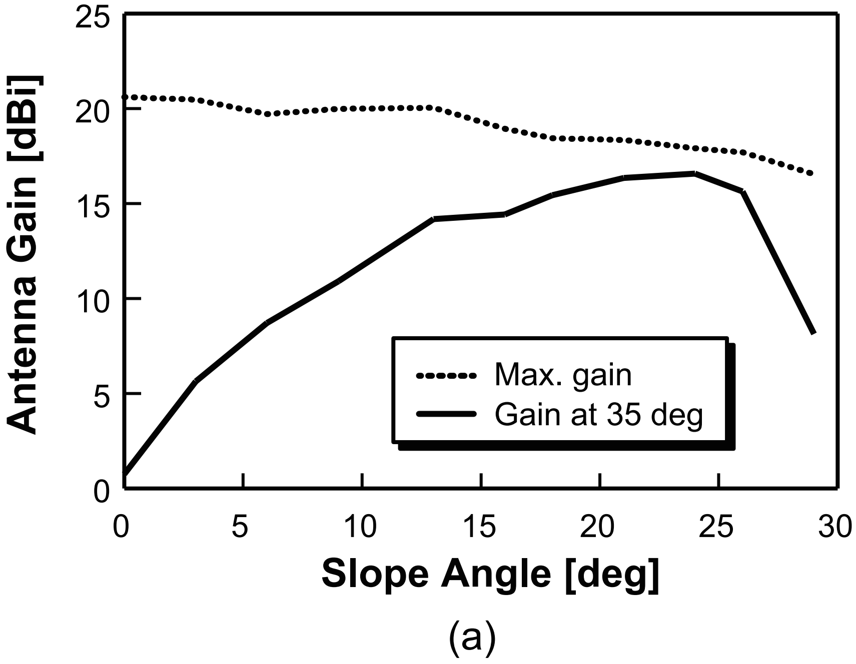

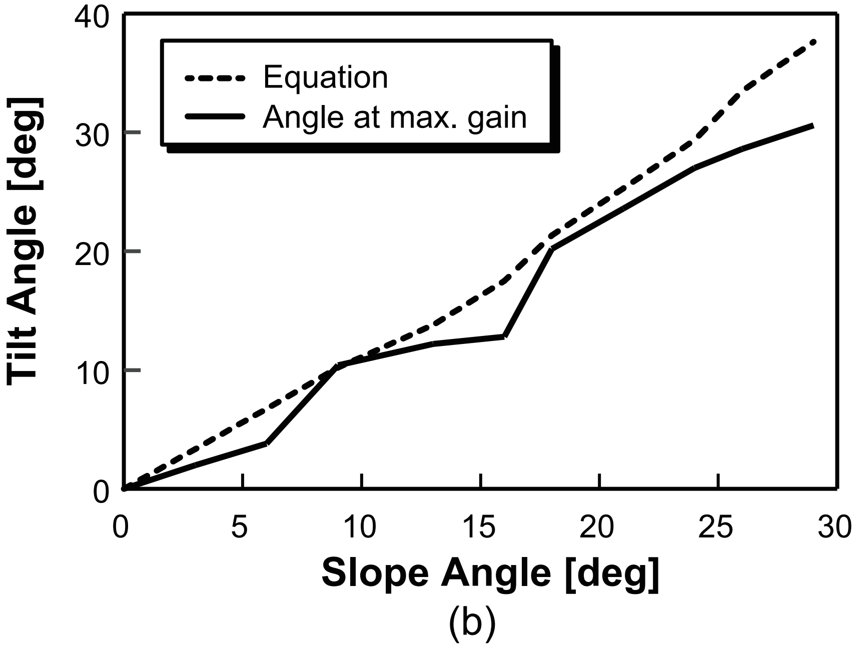

Fig. 5.8. Simulation results for proposed lens horn antenna with prism at 76.5 GHz: (a) dependence of antenna gain on slope angle of prism and (b) dependence of tilt angle of radiation pattern on slope angle of prism.

and 20 mm, respectively. The sizes of the MSA ($L_A \times W_A$) and the ground pattern ($L_G \times W_G$) were 1.06 × 1.38 and 1.5 × 3 mm, respectively. These values were optimized to provide both a high antenna gain and wide beamwidth shown in Fig. 5.5.

As shown in Fig. 5.7, the peak of the radiation pattern shifted in the azimuth direction. The antenna gain at an azimuth angle of 35 degrees increased to more than 15 dBi when the slope angle was increased to more than 18 degrees as shown in Fig. 5.8(a) due to the peak shift. A feed point was placed on the feed line at the slot of the horns as indicated Fig. 5.6(a). These results show that, with the proposed lens horn antenna with prism, the peak of the radiation pattern can be tilted by adjusting the slope angle of the prism and that the proposed antenna has the potential to achieve the target antenna gains for MRR-mode.

However, Fig. 5.7 shows that the radiation pattern between azimuth angles of 20 and 60 degrees was wavy, and Fig. 5.8(a) shows that the antenna gain at 35 degrees degraded when the slope angle was larger than 26 degrees. To analyze the cause of the small waves in the wavy range on the major lobe, the magnitude and phase distribution of an electric field radiated from the lens horn antenna with prism were simulated.

As shown in Fig. 5.9, the antenna with a slope angle of 26 degrees had a large-magnitude electric field on the side-wall of the prism, as indicated by the dotted oval in Fig. 5.9(b), which caused radiation from the side-wall.

In contrast, the antenna with a slope angle of 16 degrees did not have a large-magnitude electric field on the side-wall of the prism. The large-magnitude electric field was caused by reflection of the radiated waves at the output surface of the prism, as indicated by the dashed lines with arrows in Fig. 5.9(b). In the antenna with a slope angle of 16 degrees, the incident angle of the reflected waves on the prism side-wall exceeded the critical angle, as indicated by the dashed line with arrow in Fig. 5.9(a). This means that radiation from the side-wall did not occur. As shown in the lower portion of Fig. 5.9(b), the antenna with a slope angle of 26 degrees had a rough phase plane while the one with a slope angle of 16 degrees had a flat phase plane. These results indicate that the small waves in the wavy range on the major lobe in the radiation pattern shown in Fig. 5.7 were due to failed phase synthesis between the main radiation from the output surface of the prism and the radiation from the side-wall of the prism.

To confirm that failed phase synthesis was the degradation mechanism, I simulated radiation when a PML was attached to the side-wall of the prism. The PML works as an ideal absorber preventing radiation of electric waves from the side-wall. The shapes of the major lobe of the radiation pattern for a slope angle of 16 degrees with and without the PML were almost the same, as shown in Fig. 5.10(a). In contrast, the small waves in the radiation pattern disappeared when the PML was used, as shown

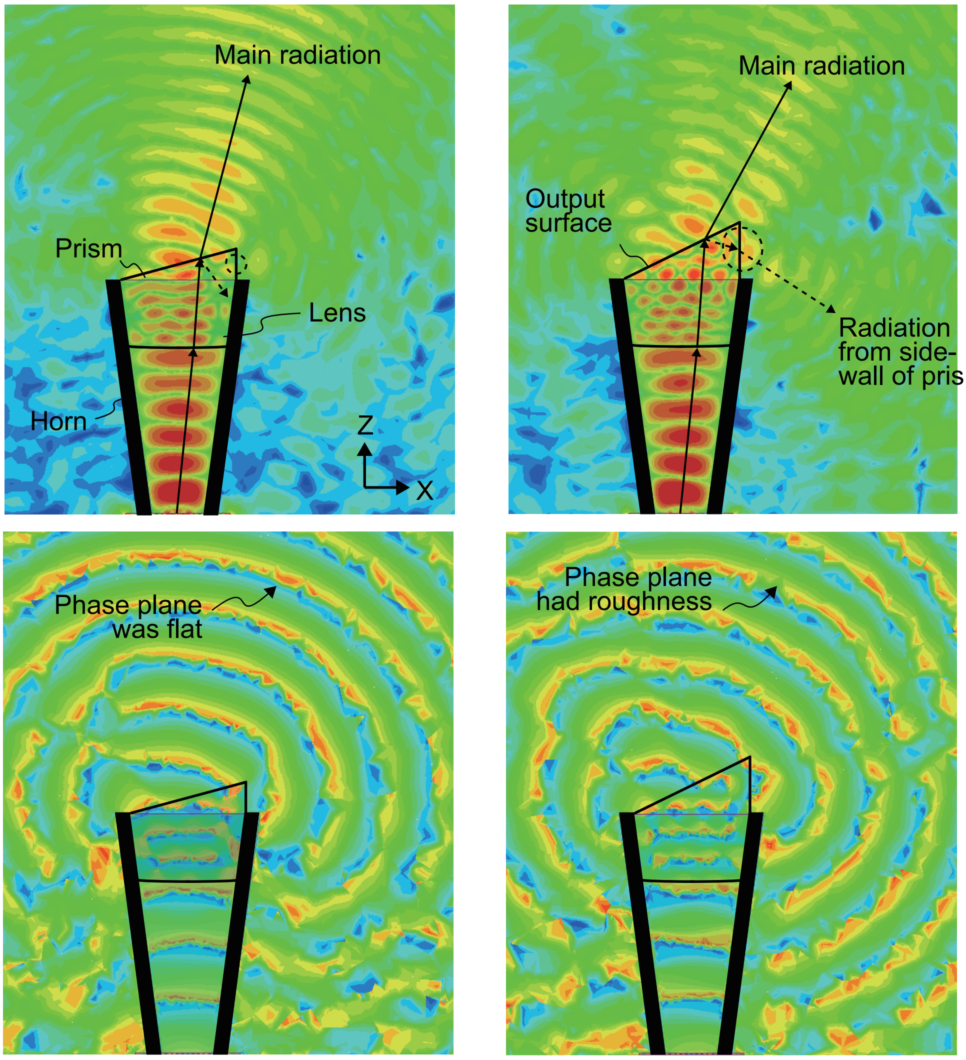

(a) Slope angle of 16 deg (b) Slope angle of 26 deg

Fig. 5.9. Simulation results for magnitude (upper side) and phase (lower side) distribution of electro-magnetic waves on ZX-plane at 76.5 GHz: (a) slope angle of 16 degrees; (b) slope angle of 26 degrees.

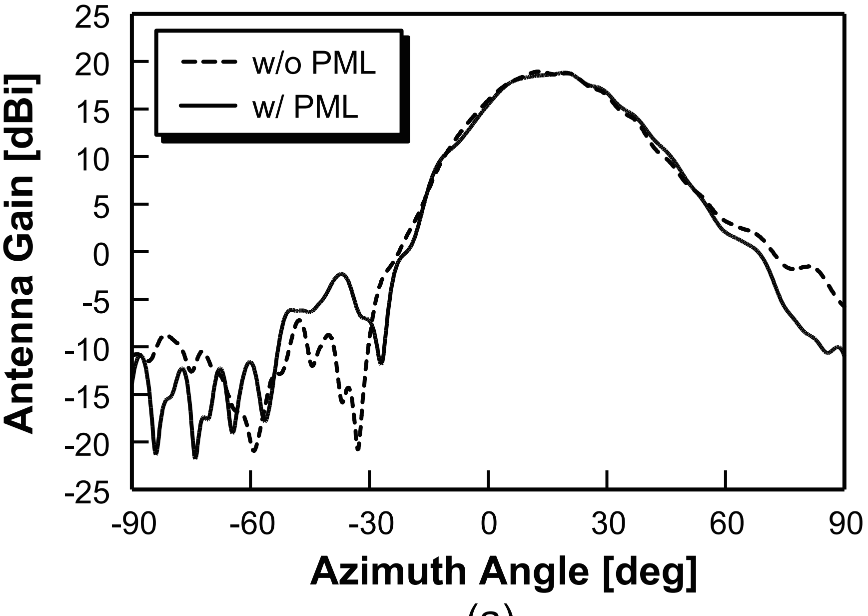

(a)

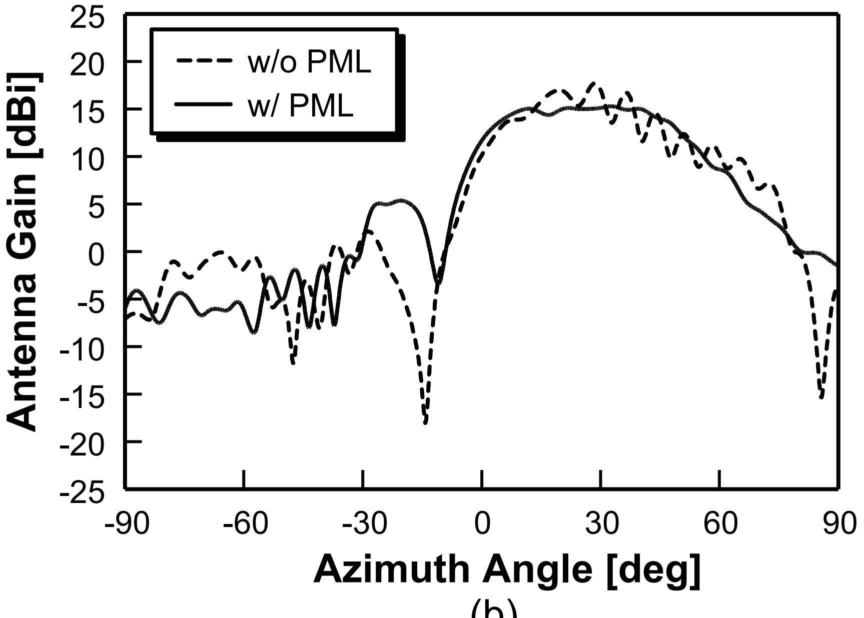

(b)

Fig. 5.10. Simulation results for radiation pattern with and without PML on side-wall of prism at 76.5 GHz: (a) slope angle of 16 degrees; (b) slope angle of 26 degrees.

in Fig. 5.10(b). These results confirm that the small waves in the radiation pattern for a slope angle of 26 degrees were caused by radiation from the side-wall. These findings mean that further improvement is needed in the radiation pattern of the lens horn antenna with prism, as described in the next section.

5.4.2 Further improvement in radiation pattern

To improve the radiation pattern of the lens horn antenna with prism for MRR-mode, I propose using two antennas with opposite radiation directivities for the transmitter. Two lens horn antennas sharing a prism are arranged in the X direction, as shown in Fig. 5.11. The prism has a chevron shape, and the portions of the prism output surface corresponding to the two antennas ("surface A" and "surface B") are angled in opposite directions to reduce radiation from the inactivate antenna. The dashed lines with arrows in the figure indicate the path of a wave radiated from the MSA in antenna A. A portion of the wave is reflected back from output surface A, where the incident angle of the reflected wave on output surface B is larger than 180 degrees, as shown

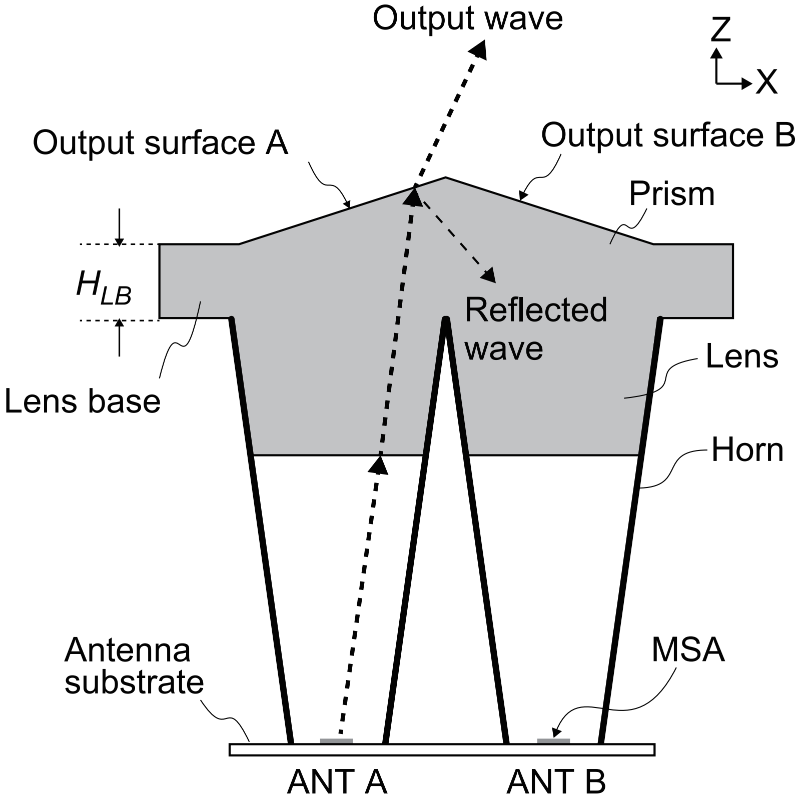

Fig. 5.11. X-Z cross-section view of antenna array composed of two lens horn antennas sharing a prism.

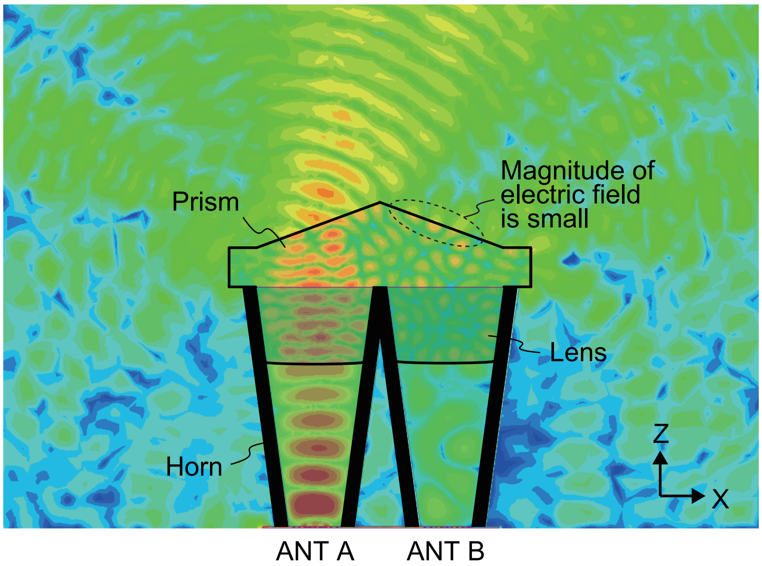

(a) Magnitude distribution of electric field

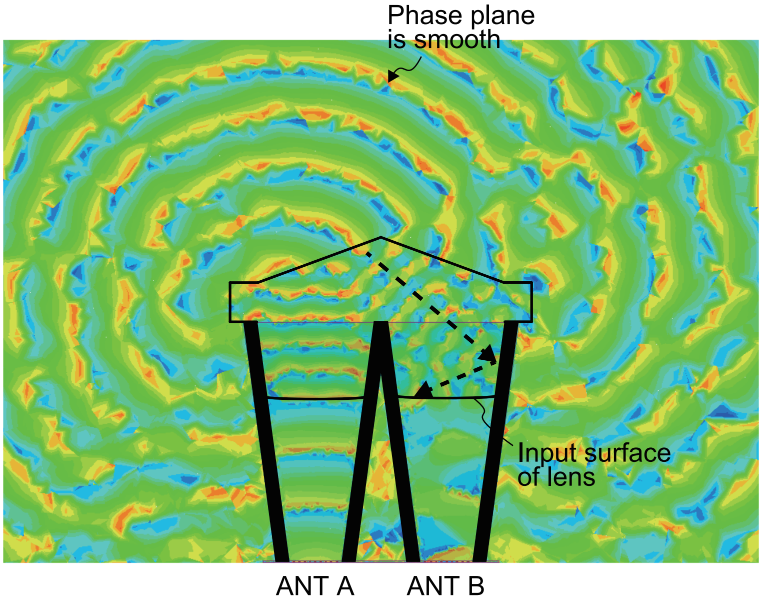

(b) Phase distribution of electric field

Fig. 5.12. Simulated (a) magnitude and (b) phase distributions of electric field on ZX-plane at 76.5 GHz.

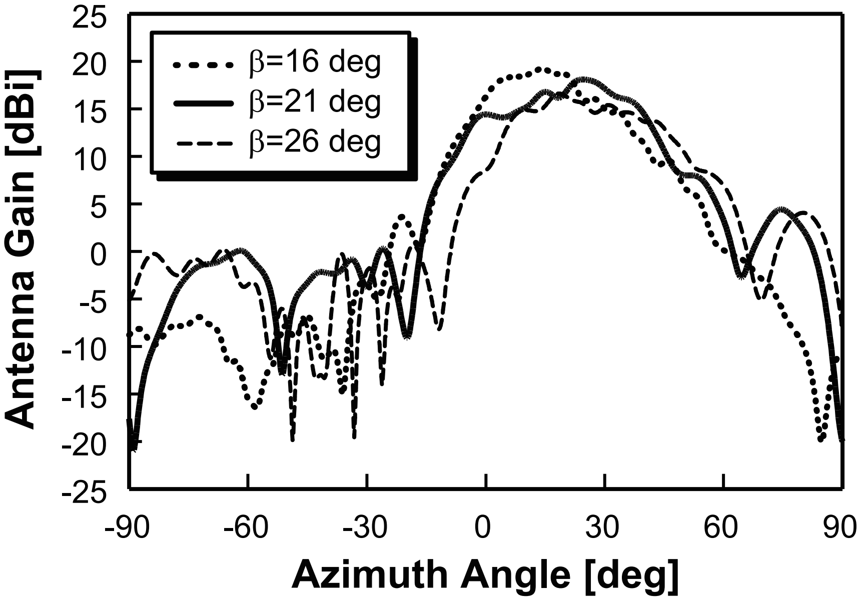

Fig. 5.13. Simulated radiation pattern in azimuth of proposed antenna array composed of two lens horn antennas sharing chevron-shaped prism at 76.5 GHz for prism slope angles of 16, 21, and 26 degrees.

in Fig. 5.11.

Thus, the wave reflected on output surface A is (ideally) not output from output surface B. With this configuration, the main wave output from surface A is not interfered with by a wave output from surface B, so the radiation pattern is smooth.

I simulated the magnitude and phase distributions of an electric field on the ZX-plane at 76.5 GHz when antenna A was activated and antenna B was connected to a 50Ω load. The slope angle of the prism was 21 degrees. The thickness of the lens base, H_{LB}, was set to 3 mm in consideration of the stiffness needed for a lens with a prism that functions as the radome of a radar package. The other parameters for the horns, lenses, and MSAs were the same as those given in Chapter 3; the antennas had a symmetrical shape in the X direction. Fig. 5.12(a) shows that the magnitude of electric field on surface B was small as indicated by the dotted oval, and Fig. 5.12(b) shows that the phase surface was smooth.

As shown in Fig. 5.13, the radiation patterns for slope angles of 21 and 26 degrees had a smooth pattern in their major lobe compared with the patterns shown in Fig. 5.7. Moreover, the antenna with a slope angle of 21 degrees provided an antenna gain of 15.7 dBi at an azimuth angle of 35 degrees, which meets the target gain. Thus, a slope angle β of 21 degrees was used.

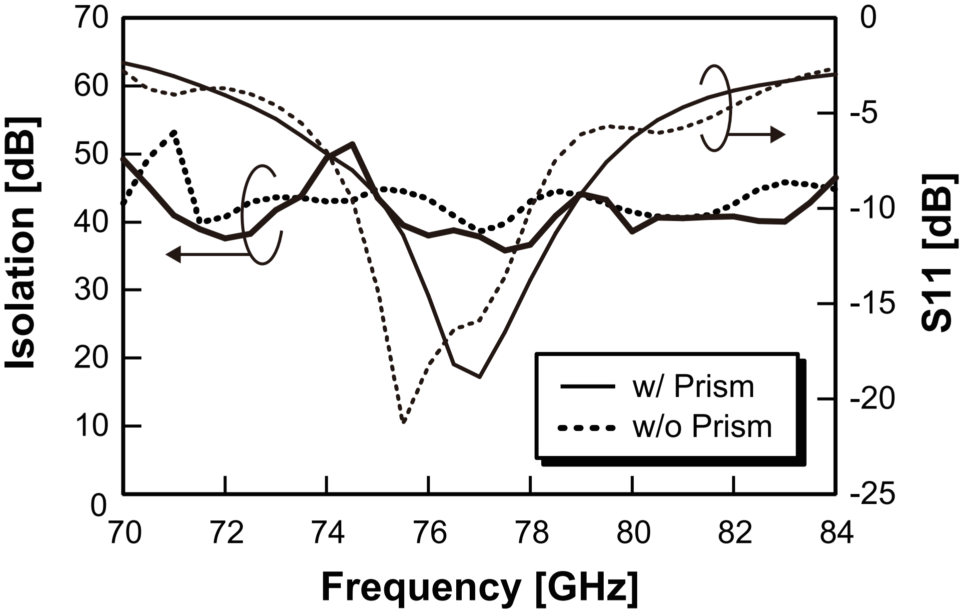

Fig. 5.14. Simulated isolation between two lens horn antennas and reflection coefficient S11 for antennas that share and do not share chevron-shaped prism.

5.4.3 Isolation between antennas with chevron-shaped prism

To investigate the side effects of arranging the lens horn antennas sharing a prism as described above, I simulated the isolation between two lens horn antennas with and without a chevron-shaped prism even though isolation between Tx antennas does not significantly affect radar performance. The two lens horn antennas that did not share a prism were arranged in the X direction, as illustrated in Fig. 5.6. The two antennas were the same size, and their horn, lens, and MSA were the same as those described in Chapter 3. As shown in Fig. 5.14, the isolations of the antennas that did and did not share a prism were greater than 38 and 39 dB from 76 to 77 GHz, where their reflection coefficients S11 were less than -15 dB, which means the effects of reflection were negligible. Reference planes of the characteristics were placed on the feed lines at the slots of the horns as indicated in Fig. 5.6(a). These results show that the degradation in antenna isolation due to applying a chevron-shaped prism is small.

The cause of providing comparable isolation can be understood by examining Fig. 5.12(b). The dashed lines with arrows indicate the path of the wave reflected back from output aperture A, which is reflected again by the horn of antenna B. The incident angle of the re-reflected wave on the input surface of the antenna B lens was about 70 degrees, which is much larger than the critical angle discussed in Section 5.4.1. Therefore, the re-reflected wave was not output from the input surface of the lens, so (ideally) the isolation was not degraded.

In short, the proposed lens horn antenna array with a chevron-shaped prism had almost the same antenna isolation as the lens horn antenna without a prism.

5.5 Configuration of Tx antenna suite for LRR- and MRR-modes

The configuration of the proposed Tx antenna suite consisting of an antenna array with two lens horn antennas that share a chevron-shaped prism (ANT-2 and ANT-3) and one lens horn antenna (ANT-1) for dual-range dual-FOV radar is illustrated in Fig. 5.15. ANT-1 is used to produce a radiation pattern directed at boresight for LRR-mode, and ANT-2 and ANT-3 are used to produce radiation patterns for MRR-mode, with directivity respectively to the left and right in azimuth, as illustrated in Fig. 5.4. The output-aperture size of the horn for LRR-mode ($L_o \times W_o$) was 33 × 18 mm and other parameters were the same as those for MRR-mode described in Section 5.4.1. Gaps between each output-aperture of the antenna were 1 mm. The required size of antenna substrate was 28.5 × 2 mm at a minimum as shown in Fig. 5.15(a), whose definition was same as that described in Section 4.1 and Fig. 4.4.

As shown in Fig. 5.16, the proposed antenna array had an antenna gain of 22 dBi at boresight and an azimuth HPBW of 20 degrees in LRR-mode at 76.5 GHz. The gain was larger than 15.7 dBi within azimuth angles of ±35 degrees at 76.5 GHz in MRR-mode. These simulated gains meet the target gains shown in Figs. 1.12 and 5.5.

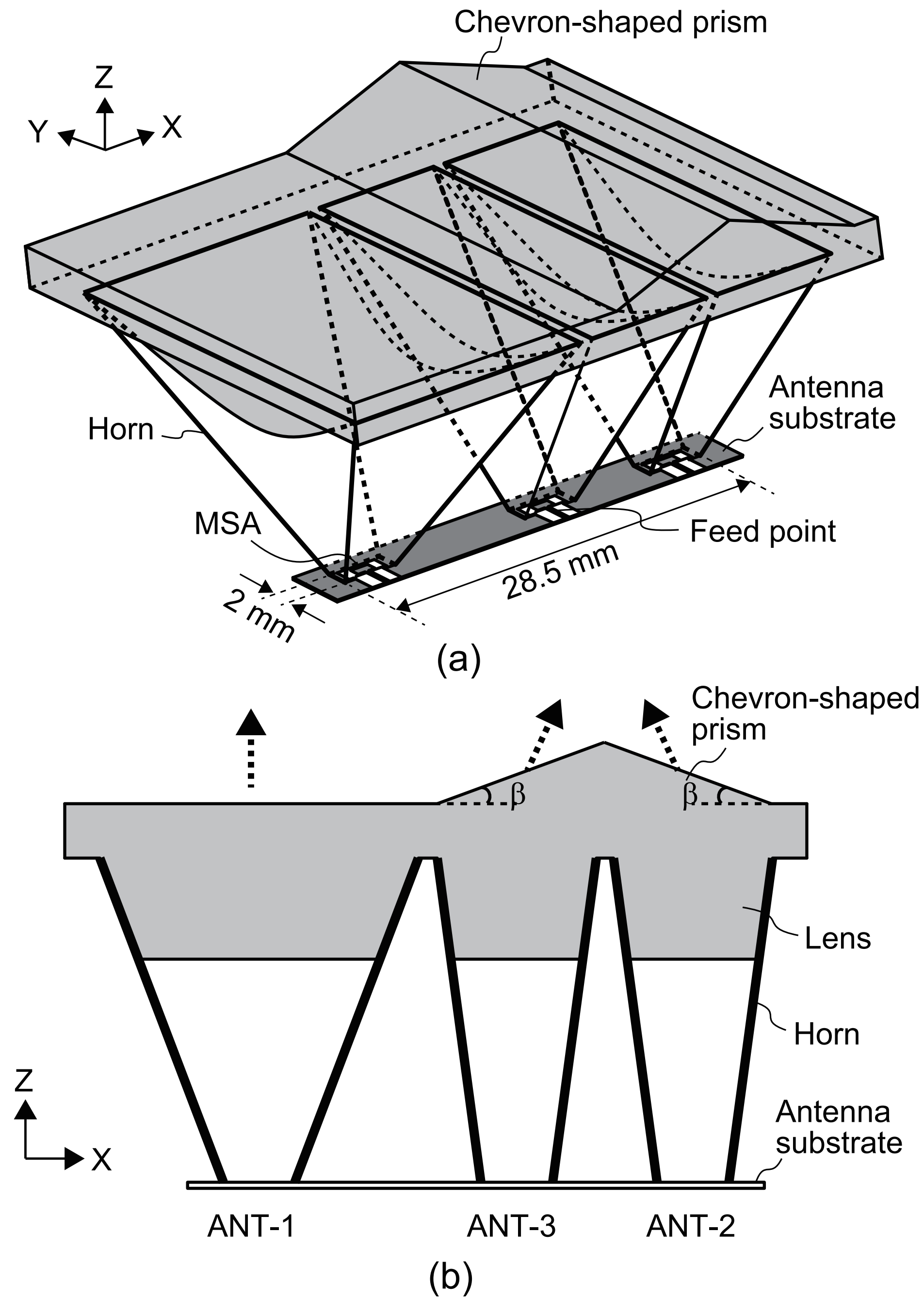

Fig. 5.15. Structure of array antenna with two lens horn antennas that share chevron-shaped prism and one lens horn antenna: (a) perspective view; (b) ZX-plane cross-sectional view.

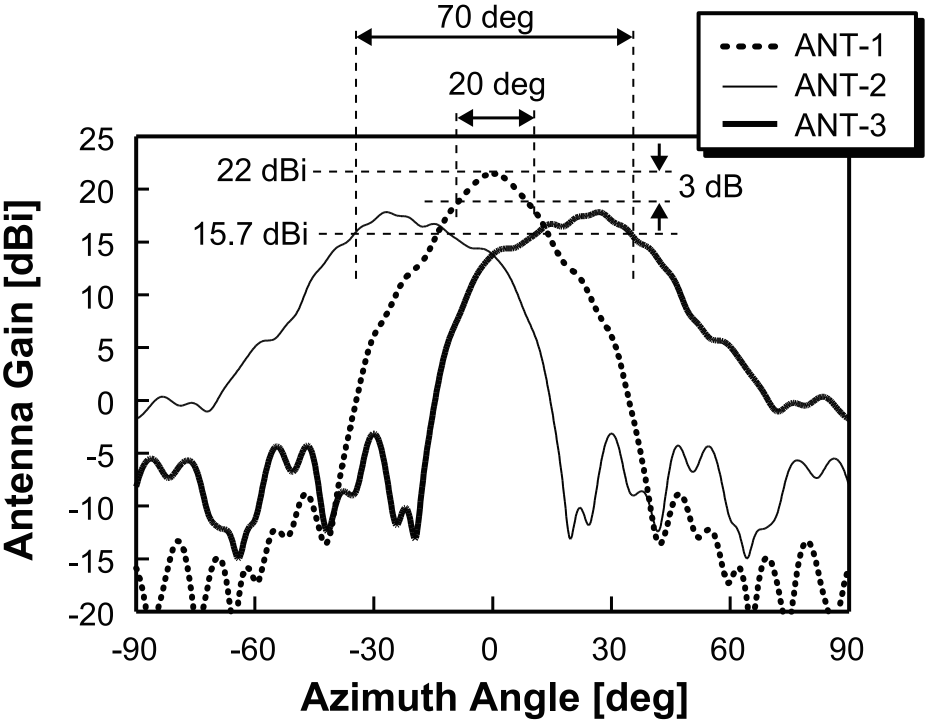

Fig. 5.16. Simulated total radiation pattern of proposed array antenna in azimuth at 76.5 GHz.

5.6 Fabricated antennas and measurement results

5.6.1 Fabricated antennas

I fabricated lens horn antennas that share a chevron-shaped prism for MRR-mode and a separate lens horn antenna for LRR-mode (Fig. 5.17). Each antenna for MRR-mode had an output-aperture size ($D_o \times W_o$) of 33 $\times$ 9 mm and a height (H) of 18 mm. The slope angle of the prism was 21 degrees, and the thickness of the lens base (H_{LB}) was 3 mm. The antenna for LRR-mode had an output-aperture size of 33 $\times$ 18 mm and a height of 18 mm. In the measurement setup, the antenna substrates were pasted onto base plates made of Al. The horns were fixed to the base plates with four mmϕ screws, which are commonly used to connect standard WR-10 waveguides.

The pyramidal horn and dielectric lens were made of Al and PPS. The antenna substrates were made of high-frequency circuit materials (Rogers RO3003).

5.6.2 Measurement results

As shown in Fig. 5.18(a), the measured radiation pattern for the major lobe of the antenna fabricated for MRR-mode was similar to the simulated pattern. The insertion loss of the feed line for measurement was de-embedded and the feed point was same as

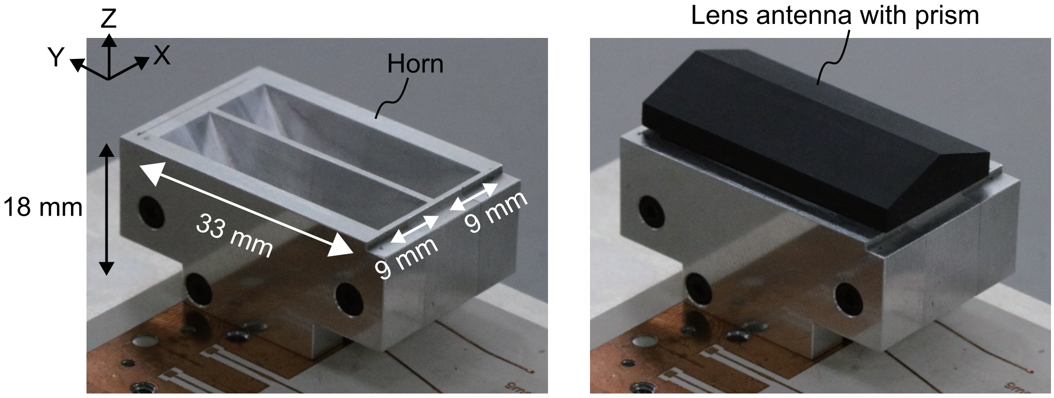

(a) Antennas without lens (b) Antennas with lens

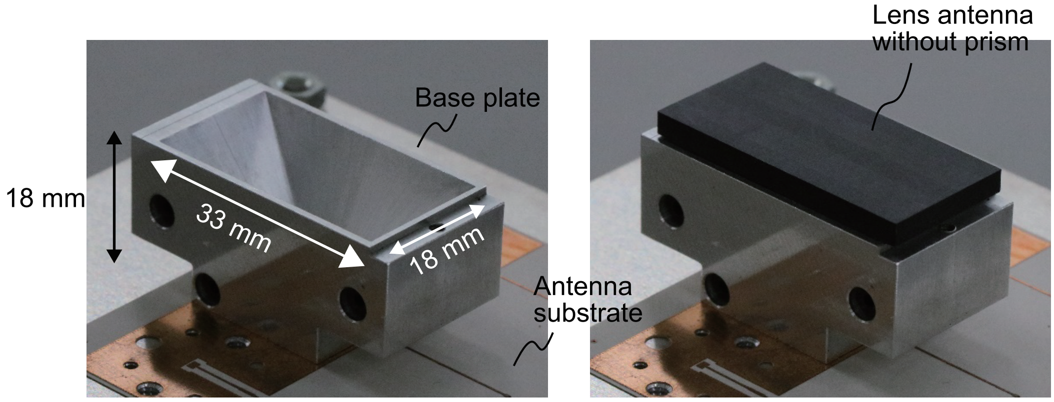

(c) Antenna without lens (d) Antenna with lens

Fig. 5.17. Photographs of fabricated antennas: (a) and (b) are perspective views of antennas without and with lens for MRR-mode; (c) and (d) are perspective views of antenna without and with lens for LRR-mode.

the simulation (Fig. 5.6(a)). The antenna had a gain of 15.5 dBi at an azimuth angle of 35 degrees. The measured S11 was also similar to the simulated one, as shown in Fig. 5.18(b), where a reference plane was placed at the end of a feed line for measurement with insertion loss of about 2 dB.

The S11 was less than -17 dB from 76 to 77 GHz, which is small enough for this antenna to be used for radar. The small periodical dips with few-GHz periods in the measured S11 were caused by an impedance mismatch between the microstrip line and contact pattern on the antenna substrate used for connecting a GSG (ground-signal-ground) probe [4.2] due to an error in etching the microstrip line and contact pattern.

As shown in Figs. 5.20(a) and (b), the measured radiation pattern for the major lobe of the antenna fabricated for LRR-mode was also similar to the simulated pattern in both azimuth and elevation. The insertion loss of the feed line for measurement was de-embedded. The antenna had a gain of 21.5 dBi at boresight. The azimuth and elevation HPBWs of the antenna were 22 and 6 degrees, respectively. The measured S11 was also similar to the simulated one, as shown in Fig. 5.20(c). A reference plane was placed at the end of a feed line for measurement with insertion loss of about 2 dB The S11 was less than -14 dB from 76 to 77 GHz, which is again small enough for this antenna to be used for radar. The small periodical dips in the measured S11 were due to the etching error explained above.

As shown in Fig. 5.21, the proposed antenna array with three Tx antennas had a measured gain of 21.5 dBi at boresight and an HPBW of 22 degrees for LRR-mode at 76.5 GHz. The antenna gain was larger than 15.5 dBi within azimuth angles of ± 35 degrees for MRR-mode. These measured Tx antenna gains meet the target gains shown in Fig. 5.5. The fabricated antenna array thus produces the beams required for dual-range dual-FOV radar shown in Fig. 1.12.

Table 5.1 lists comparison of proposed Tx antenna and previous design which can be applied to a mono-layer substrate. The proposed antenna provided an antenna gain reduction of -6 dB at ± 35 degrees in azimuth, which was comparable to the result in previous work reported by Jeong et. al [1.38], using an antenna substrate area of 57 mm^2 (28.5×2 mm) which was match smaller than an output-aperture area. Since the previous work uses different frequency band and specification of antenna gain, it is difficult to compare the required antenna substrate area at a minimum. I estimated the required antenna substrate area by using the reported results because the frequency band and specification of antenna gain reported in [2.13] was near those in this study, The antenna gain at boresight of the comb-line antenna is 22.5 dBi where the length of a subarray is 58.5 mm in the previous work [2.13], therefore, the length of the subarray becomes about 46.5 mm to provide the antenna gain of 21.5 dBi at bore-

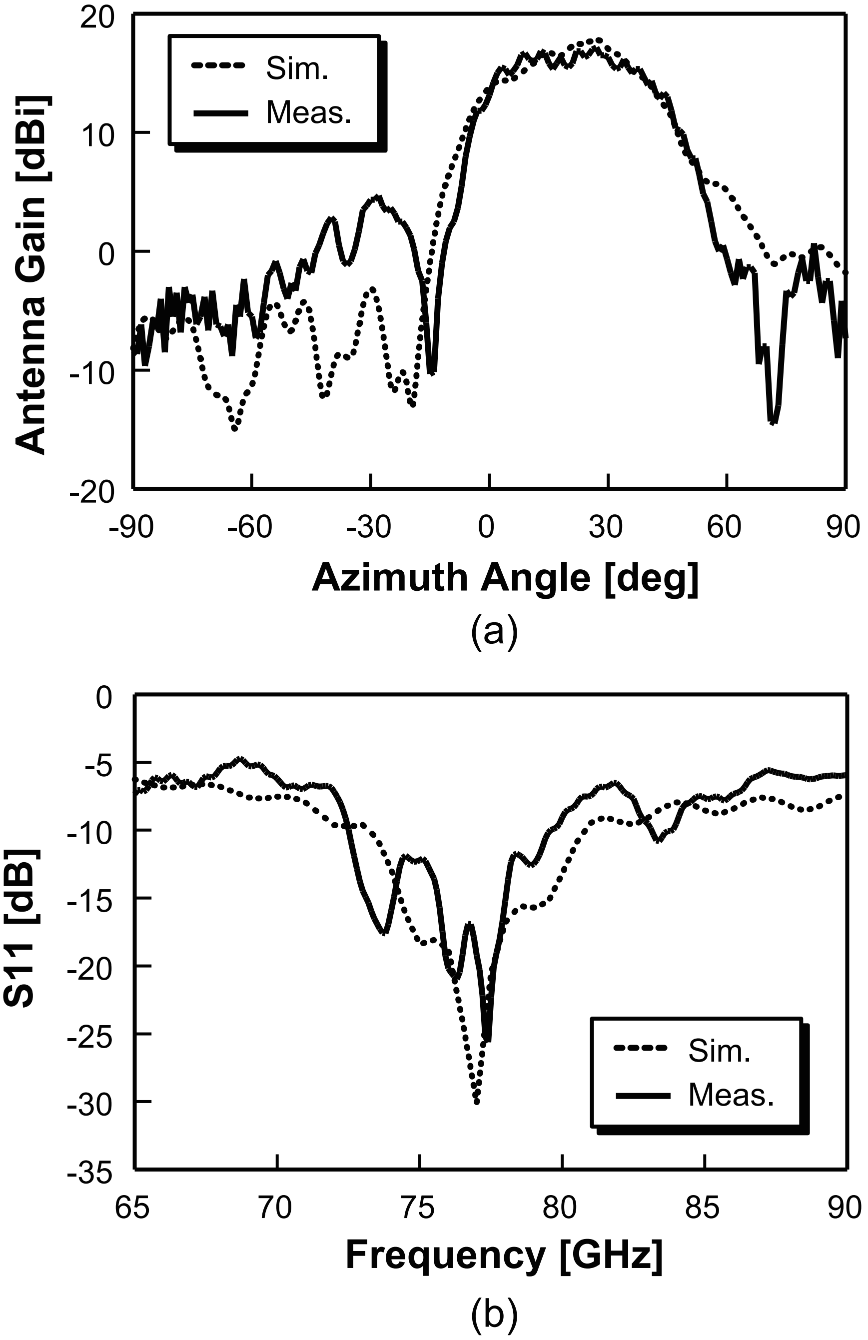

Fig. 5.18. (a) Simulated and measured radiation patterns (corresponding to ANT-3 in Fig. 5.15) in azimuth plane at 76.5 GHz and (b) reflection coefficient S11 of antenna fabricated for MRR-mode (Figs. 5.17(a) and (b)).

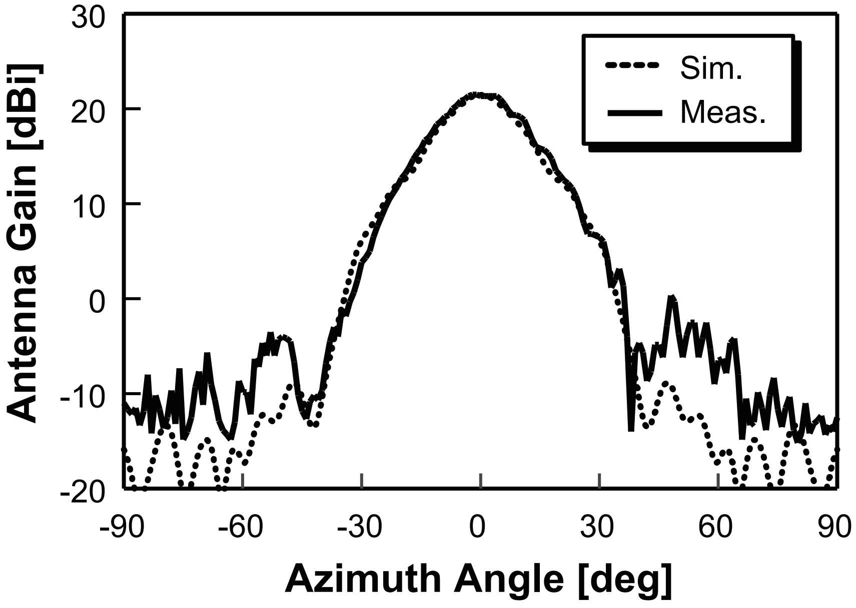

(a)

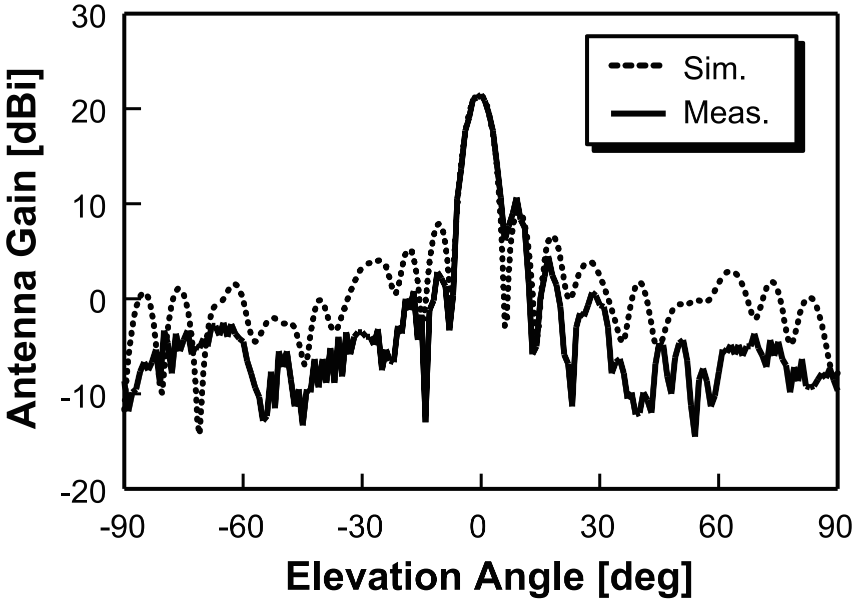

(b)

Fig. 5.19. (a) Simulated and measured radiation patterns in azimuth plane at 76.5 GHz and (b) simulated and measured radiation patterns in elevation plane of antenna fabricated for LRR-mode (Figs. 5.17(c) and (d)).

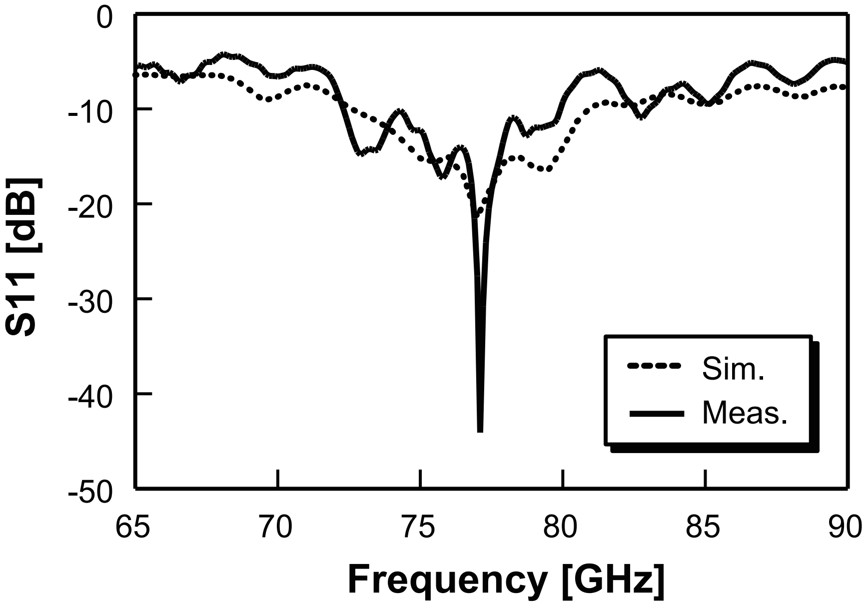

Fig. 5.20. Simulated and measured reflection coefficient S11 of antenna fabricated for LRR-mode (Figs. 5.17(c) and (d)).

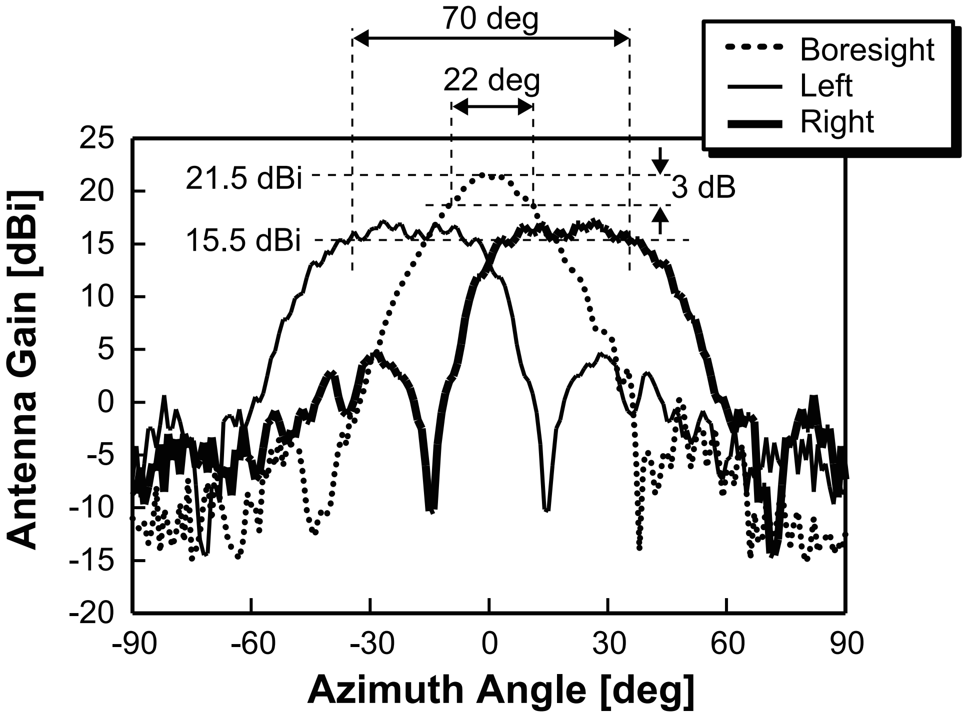

Fig. 5.21. Measured total radiation pattern in azimuth plane at 76.5 GHz of proposed antenna array with three Tx antennas.

Table 5.1. Comparison of proposed Tx antenna and previous design.

Item	This study	[1.38]	Estimated from [2.13] and [1.38]
Tx architecture	Switches 3 antennas	Switches 2 antennas	Switches 2 antennas
Antenna type	Lens horn antenna with single MSA	Series-fed antenna	Comb-line antenna
Frequency band	77 GHz	24 GHz	77 GHz
Antenna gain	21.5 dBi at boresight 15.5 dBi at ±35°	18 dBi at boresight 12 dBi at ±40°	21.5 dBi at boresight N.A. at ±35°
Antenna gain reduction	−6 dB at ±35°	−6 dB at ±40°	N.A.
Output-aperture area	1254 mm^2	N.A.	669 mm^2
Substrate area (in principle)	57 mm^2	N.A.	669 mm^2

sight. Two subarrays were used in the previous report [1.38], therefore, an antenna for MRR-mode should have one subarray whose antenna gain at boresight is about 18.5 dBi. The width of the antenna for MRR-mode becomes about 3.5 mm since the width of the two subarrays is about 7 mm. Then, total width of two antennas for LRR- and MRR-modes is estimated 14.4 mm by separating the two antennas by $1\lambda_0$ (3.9 mm). As a result, the required antenna substrate area of the two antennas with the comb-line antenna becomes about 669 mm^2 in the 77-GHz band, which is equivalent to an output-aperture area as described in Section 2.4.2. According to the above estimation, the proposed antenna attains smaller antenna substrate area (57 mm^2) than the previous works (669 mm^2).

5.7 Versatility of lens horn antenna with prism

A design frequency dependence of the widening of the beamwidth in MRR-mode by using the antennas with horn, lens, and MSA has been investigated as a versatility of the proposed technology in the previous sections. Similar to Sections 3.7 and 4.5, the frequency of 60, 90, and 110 GHz were chosen as examples.

In the investigation of versatility, the sizes of the horn, lens, thickness of antenna substrate were changed corresponding to the design frequency using the same method described in Section 3.7. The sizes of output-aperture ($W_o \times D_o$) for the design frequency of 60, 90, and 110 GHz were 23 × 42.1, 15.3 × 28.1, and 12.5 × 23 mm,

Table 5.2. Main parameters of proposed antenna for each design frequency.

Design frequency	60 GHz	76.5 GHz	90 GHz	110 GHz
Output-aperture size [mm]	23 × 42.1	18 × 33	15.3 × 28.1	12.5 × 23
Input-aperture size [mm]	5.1 × 2.55	4 × 2	3.4 × 1.7	2.8 × 1.4
Horn height [mm]	23	18	15.3	12.5
Lens focus distance [mm]	25.5	20	17	14

respectively. The arrangement of Tx antennas and prism shape were the same as shown in Fig. 5.11; however, a wave port was applied to the radiation source at the input-aperture of each horn instead of the MSA in order to simplify the discussion on the effect of the prism in this section. Table 5.2 lists the main parameters for the Rx antennas for each design frequency. Loss factors of materials for horn and lens were same as Chapter 3 (Table 3.1).

Simulated results of radiation pattern in azimuth for the antennas with two horns, two lenses, and chevron-shaped prism shared with the horns are shown in Fig. 5.22: (a) design frequency of 60 GHz, (b) 76.5 GHz, (c) 90 GHz, and (d) 110 GHz. In each graph, dash-dotted, dotted, solid, and dashed lines indicate the results where the slope angle of prism of 0, 16, 21, and 26 degrees, respectively. As shown in the figure, the beam center shifts as increasing the slope angle comparably. Fig. 5.23(a) shows the simulated results for dependence of the peak angle (corresponds to a beam-nose) of the radiation pattern in azimuth on the slope angle of the prism and an ideal beam tilt angle calculated by the equation (5.2). Thick solid, dotted, thin solid, and dash-dotted lines mean the results for the peak angle of the radiation pattern in azimuth whose design frequencies were 60, 76.5, 90, and 110 GHz, respectively, and thick dashed line indicates the ideal beam tilt angle. Although the results have some deviations, the tilt angles increase as increasing the slop angle of the prism and have comparable tendency. Fig. 5.23(b) shows simulated results for dependence of a normalized antenna gain at azimuth angle of 35 degrees where antenna gains at each slope angle were normalized by that at the slope angle of 0 degree. Thick solid, dotted, thin solid, and dash-dotted lines mean the results for the peak angle of the radiation pattern in azimuth whose design frequencies were 60, 76.5, 90, and 110 GHz, respectively. The results showed that the normalized gain of each design frequency had comparable performance.

According to the above results, the proposed antenna provided versatility on design frequency for widening beamwidth in MRR-mode.

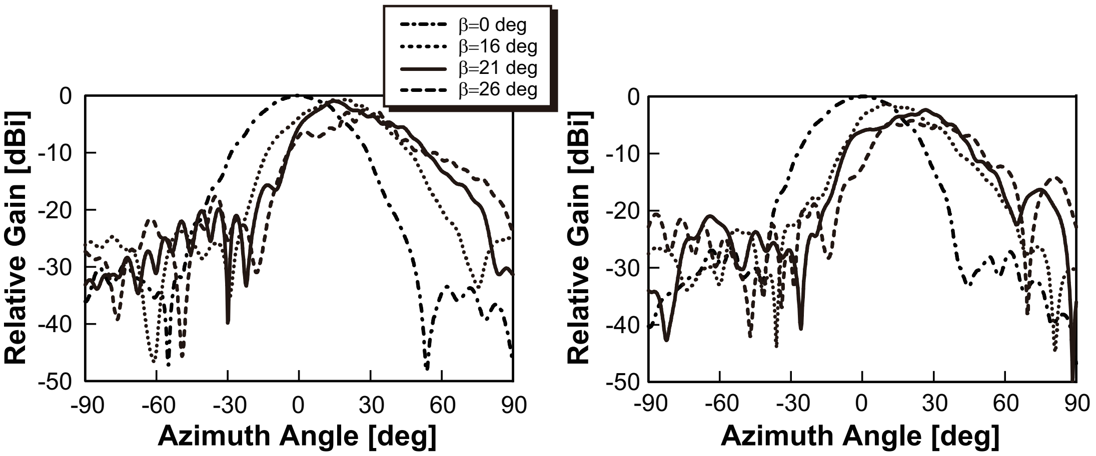

(a) 60 GHz (b) 76.5 GHz

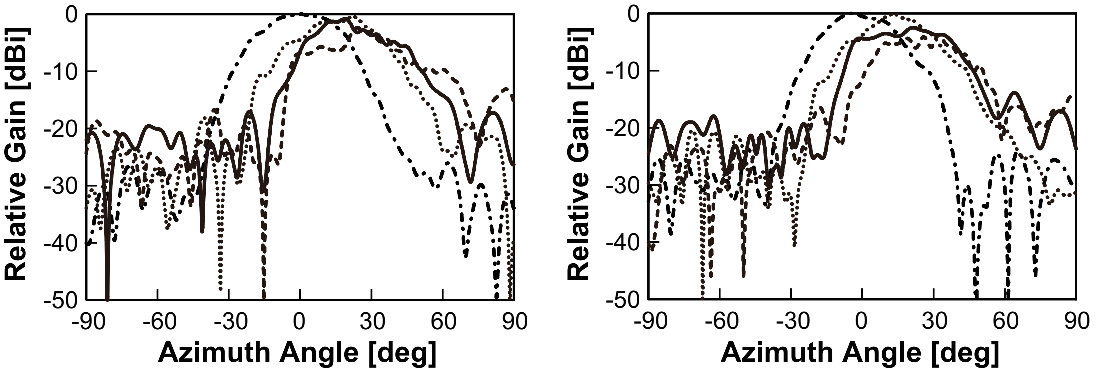

(c) 90 GHz (d) 110 GHz

Fig. 5.22. Simulation results for relative antenna gain of antenna with two horn, two lens, and chevron-shaped prism whose design frequencies were (a) 60 GHz, (b) 76.5 GHz, (c) 90 GHz, and (d) 110 GHz.

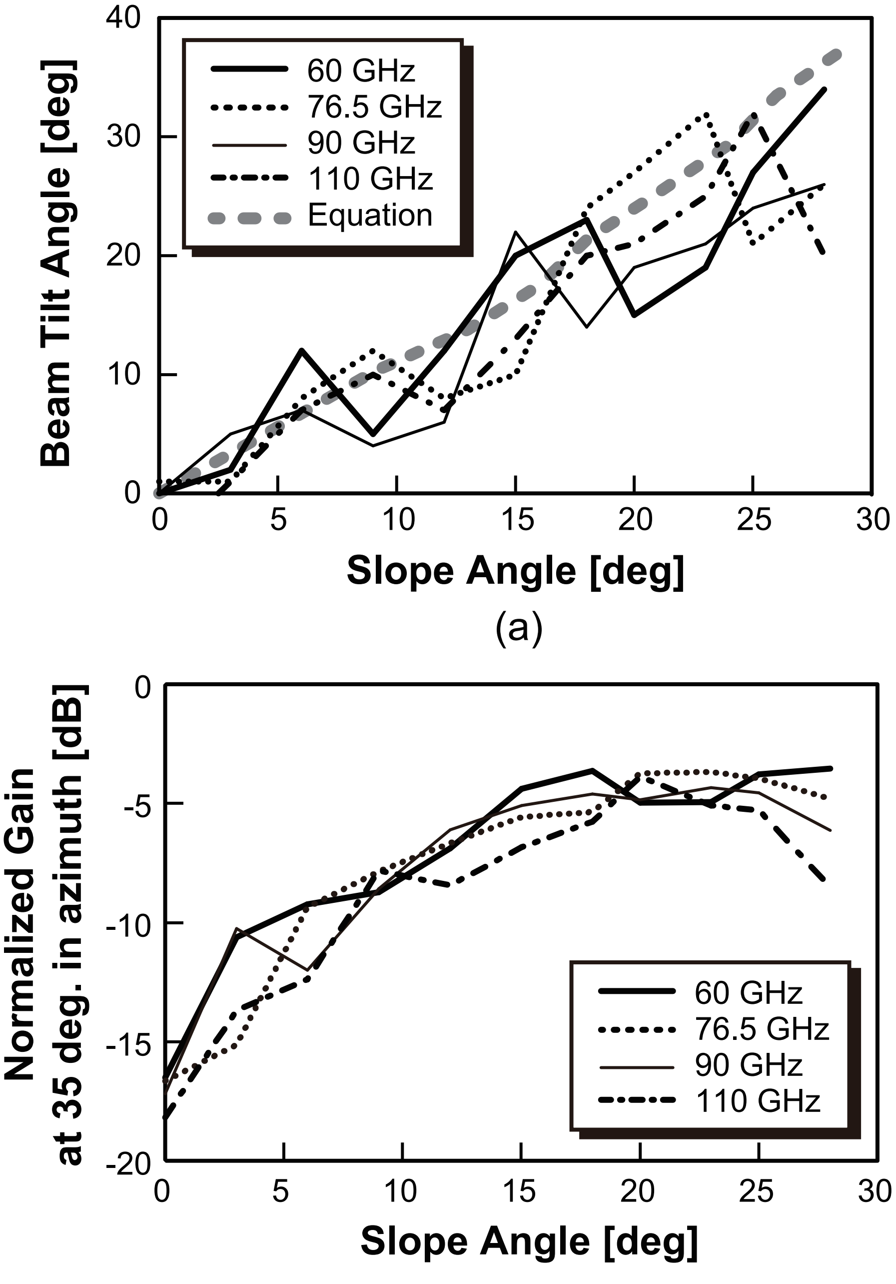

(a)

(b)

Fig. 5.23. Simulation results for dependence of normalized antenna gain of antenna with two horns, two lenses, and chevron-shaped prism on slope angle of prism.

5.8 Conclusion

A Tx antenna array comprising two lens horn antennas sharing a chevron-shaped prism and one lens horn antenna without such a prism was investigated for a dual-range dual FOV automotive radar using the 77-GHz band. Long-range detection requires a narrow FOV while middle-range detection requires a wide FOV. The lens horn antenna without a prism is used for long-range detection. To widen the FOV for middle-range detection, a novel antenna structure was previously developed two lens horn antennas share a prism at the output-aperture that directs the waves from one antenna to the right and those from the other antenna to the left. However, the radiation pattern of the major lobe becomes wavy as the tilt angle is increased due to a large amount of unwanted radiation from a side-wall of the prism. To solve this problem, a new antenna-array-with-prism structure was developed. The prism was given a chevron shape, and the portions of the prism output surface corresponding to the two antennas that share the prism are angled in opposite directions. This tilts their radiation patterns to the left and right, and reduces the unwanted radiation.

A fabricated Tx antenna array achieved a gain of 21.5 dBi and an HPBW of 22 degrees at boresight for long-range detection and one of more than 15.5 dBi within azimuth angles of ± 35 degrees for middle-range detection at 76.5 GHz. This antenna array for long-range and middle-range detections had the reflection coefficients S11 of less than -14 and -17 dB, respectively, from 76 to 77 GHz. These results demonstrate that the proposed antenna array is applicable to dual-range dual-FOV automotive radar. The required antenna substrate area was 57 mm^2 in principle, which was smaller than the estimated one (669 mm^2) that was obtained by combining two previous works on the Tx architecture and comb-line antenna.

Moreover, simulation results showed that the proposed antenna designed to apply it to frequencies of 60, 76.5, 90, and 110 GHz provided comparable normalized antenna gains at azimuth angle of 35 degrees. Therefore, the proposed antenna with two horns, two lenses, and a chevron-shaped prism had versatility on design frequency for widening beamwidth in the middle-range detection.

Chapter 6

Conclusion and Future Works

6.1 Conclusion

ADAS and AD systems are promising means of preventing traffic accidents, reducing the environmental load, and achieving a sustainable society. Various technologies for ADAS and AD have been actively investigated for achieving these objectives. ADAS and AD systems use various types of sensors to detect objects around the ego vehicle in various situations instead of the driver. Commonly used sensors include cameras and millimeter-wave radar, LiDARs, and sonars. Whereas millimeter-wave radars have poor object classification performance, they have robust sensitivity under conditions such as rain, snow, fog, and bright sunlight in which camera performance is degraded. Thus, radar sensing is needed to achieve robust sensing with camera-based ADAS and AD systems.

Millimeter-wave radars for automotive applications are commonly categorized on the basis of their detection range: LRR, MRR, and SRR. LRR is usually used to detect obstacles at distances over 200 m in front of the ego vehicle for applications such as pre-crash warning and adaptive cruise control. MRR is usually used to detect objects around the ego vehicle within about a 100-meter range, so MRR requires a wider FOV than LRR. SRR is used to detect objects around the ego vehicle to cover blind spots in the MRR coverage to provide a radar cocoon around the vehicle. Each type of radar is commonly produced separately; now, however, a new type of radar called “dual-range dual-FOV radar” that covers both the LRR and MRR detection areas is needed to obtain more redundant sensing in front of the ego vehicle.

The dual-range dual-FOV radar is typically installed behind the front bumper, the front grill, or an emblem on the front grill so as not to disturb the vehicle design. Therefore, a small housing especially with a small face area is required. In addition to the small face, a small depth is also required to install the dual-range dual-FOV radar to compact cars. Another consideration is the cost of materials and fabrication, which is an important issue in mass production.

To meet these requirements, it is important to achieve a high antenna gain, low feed-line loss, and high antenna isolation, while downsizing a front-end module composed of antennas and MMICs. Moreover, it is also important to provide a wide beamwidth in a middle-range detection by using the same antenna structure for a long-range detection.

In this dissertation, I proposed and evaluated novel structures for Tx antennas and Tx architecture for the dual-range dual-FOV radar, considering a small antenna substrate, high antenna gain, productivity and cost reduction. A lens horn antenna fed by a single MSA was proposed, which can be applied to a mono-layer substrate in order to solve the above issues on the automotive millimeter-wave radar. In particular, the proposed antennas provide a high antenna gain and wide beamwidth in azimuth by using smaller antenna substrate area than previous works. The substrate area is much smaller than an output-aperture area of the antennas. Moreover, the proposed antenna structure enables three-dimensional integration where MMICs are mounted at the shaded area of the horns so as to reduce the antenna substrate area. Furthermore, the antenna substrate area can be reduced by a high-density integration where Rx antennas can be arranged without gaps between output-apertures of them because the proposed antenna structure has a high antenna isolation. The detail technologies and fabrication results for the newly proposed antennas are summarized in the following three sections.

6.1.1 Proposal and verification of newly proposed lens horn antenna fed by single microstrip antenna

An antenna composed of a pyramidal horn and a dielectric lens with a small antenna substrate and high production tolerance for 77-GHz LRR has been investigated as a basic structure of antennas in this study. By employing a new horn-to-microstrip transition with a single MSA incorporated in the input aperture of the pyramidal horn, the antenna could be connected to MMICs by using a microstrip line. This structure enables integration of the antenna and MMICs on the same surface of an antenna substrate, which reduces material and production costs.

A fabricated antenna had an antenna gain of 23.5 dBi at 76.5 GHz, where the size of the antenna substrate was less than 20 $\times$ 20 mm. In principle, the required size of the antenna substrate can be reduced to 4 $\times$ 2 mm which is equivalent to the input-aperture size of the horn. The proposed antenna achieved a higher antenna gain by 1 dB using smaller antenna substrate area compared with a previous work where the antenna gain and antenna substrate area are 22.5 dBi and 408 mm^2. The antenna had HPBWs of 4.5 and 16 degrees in elevation and azimuth, respectively. The antenna also achieved a reflection bandwidth of about 4 GHz, where a reflection coefficient S11 was below -10 dB. Moreover, the horn-to-microstrip transition was designed to provide robustness against misalignment of the horn and the MSA due to mechanical deviation during mass production. Measurement results showed that the antenna gain was degraded by less than 0.2 dB and that the beam was tilted less than 0.6 and 0.7 degrees in elevation and azimuth, respectively, where the horn was misaligned to the MSA by 0.1 mm.

Moreover, simulation results showed that the proposed antenna designed to apply it to frequencies of 60, 90, and 110 GHz provided the comparable antenna gains of 23.7, 23.7, and 23.9 dBi for the design frequency of 60, 90, and 110 GHz, respectively. The simulation results for the HPBWs of those antennas were 5 and 16 degrees in elevation and azimuth, respectively, which are also comparable to those in the antenna whose design frequency was 76.5 GHz. The antennas had a relative matching frequency bandwidth of 4.1%, 4.3%, and 4.2% for the design frequency of 60, 90, and 110 GHz, respectively, which were comparable that for 76.5 GHz of 4.3%. These results demonstrated that the proposed antenna had versatility on design frequency for providing the high antenna gain and wide matching frequency bandwidth.

6.1.2 Downsizing of lens horn antenna fed by single microstrip antenna

Next, downsizing technique of the proposed lens horn antenna and structure of front-end module have been studied. Smaller antenna structures for LRR transmitters and receivers operating in the 77-GHz band for automotive application have been achieved by using antennas with a horn, lens, and MSA. The Tx antenna height was reduced half while keeping the antenna gain high and the antenna substrate small by developing an antenna structure composed of two differential lens horn antennas in which the diameter and focus distance of the lenses were half those in the previous design described in Section 6.1.1. The MSAs are directly connected to the differential outputs of an MMIC.

A Tx antenna fabricated using commercially available materials was 14 mm high and had an output-aperture of 18 × 44 mm. It achieved an antenna gain of 23.5 dBi, while reducing the height of the antenna half. The antenna had a flat beam with HPBWs in elevation and azimuth of 4.5 and 21 degrees, respectively. The required antenna substrate area was 96 mm^2 in principle. The proposed antenna achieved a higher antenna gain by 1 dB using smaller antenna substrate area compared with the previous work where the antenna gain and antenna substrate area are 22.5 dBi and 408 mm^2.

An Rx antenna array composed of four sets of lens horn antennas with an output-aperture of 9 × 22 mm and a two-by-two array configuration was fabricated for application in a newly proposed small front-end module with azimuth DOA estimation. The Rx antenna array had an antenna isolation of greater than 31 dB in the 77-GHz band, which is large enough for DOA estimation by frequency-modulated continuous wave radar receivers even though the four antennas are arranged without any gap between their output-apertures. Moreover, the proposed Tx and Rx antennas provided smaller antenna substrate than whole output-aperture of the antennas due to the high-density integration where Rx antennas were arranged without gap and the three-dimensional integration of antennas and MMIC where the MMIC was mounted below the shaded area of the horns.

Furthermore, simulation results showed that the proposed antenna designed to apply it to frequencies of 60, 76.5, 90, and 110 GHz provided an antenna isolation between adjacent Rx antennas arranged in X direction (corresponds to azimuth) of 46, 44, 42, and 45 dB at 60, 76.5, 90, and 110 GHz, respectively. Since the simulation results for the isolation between the Rx antennas with different design frequencies were comparable to that for the Rx antenna with the design frequency of 76.5 GHz, the proposed antenna had versatility on design frequencies for providing the high antenna isolation.

6.1.3 Widening FOV of antennas based on lens horn antenna fed by single microstrip antenna

Finally, a technology to widen beamwidth in the middle-range detection has been investigated. A Tx antenna array comprised of two lens horn antennas sharing a novel chevron-shaped prism and one lens horn antenna without such a prism has been investigated for 77-GHz-band automotive radar with dual-range sensing and a dual FOV. The lens horn antenna without the prism is directed at boresight to produce a radiation pattern with a narrow FOV for long-range detection. The portions of the prism output surface corresponding to the two antennas that share the prism are angled in opposite directions to tilt their radiation patterns to the left and right and thereby provide a wide FOV in azimuth for middle-range detection.

The prism created a smooth radiation pattern in the major lobe when the tilt angle was large enough to achieve an azimuth FOV of more than ±35 degrees. A fabricated transmitter antenna array achieved a gain of 21.5 dBi and an HPBW of 22 degrees at boresight for long-range detection and one of more than 15.5 dBi within azimuth angles of ±35 degrees for middle-range detection at 76.5 GHz. This antenna array for long- and middle-range detection had a reflection coefficients S11 of less than -14 and -17 dB, respectively, from 76 to 77 GHz. The antenna array thus produces the beams required for dual-range dual-FOV radar. These results demonstrated that the proposed antenna array was applicable to dual-range dual-FOV automotive radar. The required antenna substrate area was 57 mm^2 in principle, which was smaller than estimated one (669 mm^2) that was obtained by combining two previous works on a Tx architecture and antenna.

Moreover, simulation results showed that the proposed antenna designed to apply it to frequencies of 60, 76.5, 90, and 110 GHz provided comparable normalized antenna gains at azimuth angle of 35 degrees. Therefore, the proposed antenna with two horns, two lenses, and a chevron-shaped prism had versatility on design frequency for widening beamwidth in the middle-range detection.

6.2 Future works

New structures of antennas as an elemental technology for dual-range dual-FOV radars were proposed and evaluated in this study. Therefore, there are three main future works left.

(1) Investigation about Tx and Rx antenna suite for dual-range dual-FOV radar by combining the proposed technologies to confirm the effects on reduction of antenna substrate area

(2) Further study to improve performance of the proposed antennas

(3) Research to apply the proposed technologies to other applications.

In this section, the above three kinds of future works are detailed.

6.2.1 Evaluation of proposed antennas in front-end module for dual-range dual-FOV radars

The proposed antenna structure with a lens, horn, and single MSA can reduce the antenna substrate area because the antenna requires the equivalent area of the input-aperture of the horn in principle and enables three-dimensional integration of antennas and MMICs. To confirm the effects in a front-end module for a dual-range dual-FOV radar, the following items left:

- Design a front-end module with Tx and Rx antennas using the proposed antenna structure for a dual-range dual-FOV radar, and compare the antenna substrate areas of one with proposed antennas and others with the previous works as well as the face size of the radar, considering connectivity to MMICs.

- Investigate a new technique to connect the antenna substrate and horns which requires small substrate area or not require additional substrate area.

6.2.2 Improvement of antenna performance

6.2.2.1 Enhancement of antenna gain

The proposed antenna structures provided high antenna gain; however, the gain degraded due to a lens horn antenna and horn-to-microstrip transition by 0.9 and 1.5 dB, respectively, as described in Section 3.5. Therefore, there is room to enhance the antenna gain by introducing new technologies.

Regarding a lens horn antenna, technologies on antireflecting of the lens are candidates to improve the antenna gain such as those reported in the previous works [3.2, 3.3] if increasing of additional material and production costs can be suppressed in the future.

Reducing the width of slot created at the input-aperture of the horn by reducing the width of a feed line is another candidate technique to reduce the insertion loss of the horn-to-microstrip transition. This is because a portion of the radiated wave from the MSA which consists of the horn-to-microstrip transition leaks through the slot. In this study, the width of the feed line was designed about 280 μm to provide a characteristic impedance of 50Ω which was same as whole part of the feed line to reduce frequency deviation due to an etching error of metallic patterns in fabrication. The width of the feed line can be reduced to 100 μm as an example, which is decided considering the design rule of the substrate. Therefore, the width of the slot can be reduced by at least 180 μm. Moreover, adding an impedance matching circuit may enable further reduction of the slot width, where a coupling capacitance between the feed line and slot is not negligible.

6.2.2.2 Expansion of reflection bandwidth

The available frequency bandwidth of the 77-GHz band is limited to 1 GHz (from 76 to 77 GHz). On the other hand, the 79-GHz band has the bandwidth of 4 GHz (from 77 to 81 GHz) and both 77-GHz and 79-GHz band can be used simultaneously. As explained in Section 1.5.1, a higher range resolution can be obtained as expanding the modulation frequency bandwidth in FMCW radars. Therefore, technologies to support such wide frequency bandwidth up to 4 or 5 GHz.

To simplify the discussion to design frequency bandwidth, a bandwidth where a reflection coefficient S11 of an antenna is below -10 dB is used as a design bandwidth. Fig. 6.1 shows a way of thinking about relationship between the design bandwidth BW_D and specified bandwidth BW_S, where BW_S is 1 GHz in the 77-GHz band as an example. A frequency characteristics of the S11 shifts by f_{ERR+} or f_{ERR-} due to deviations in manufacturing such as etching errors of metallic patterns for MSAs and microstrip lines and a misalignment of horns and MSAs. Thus, the design bandwidth

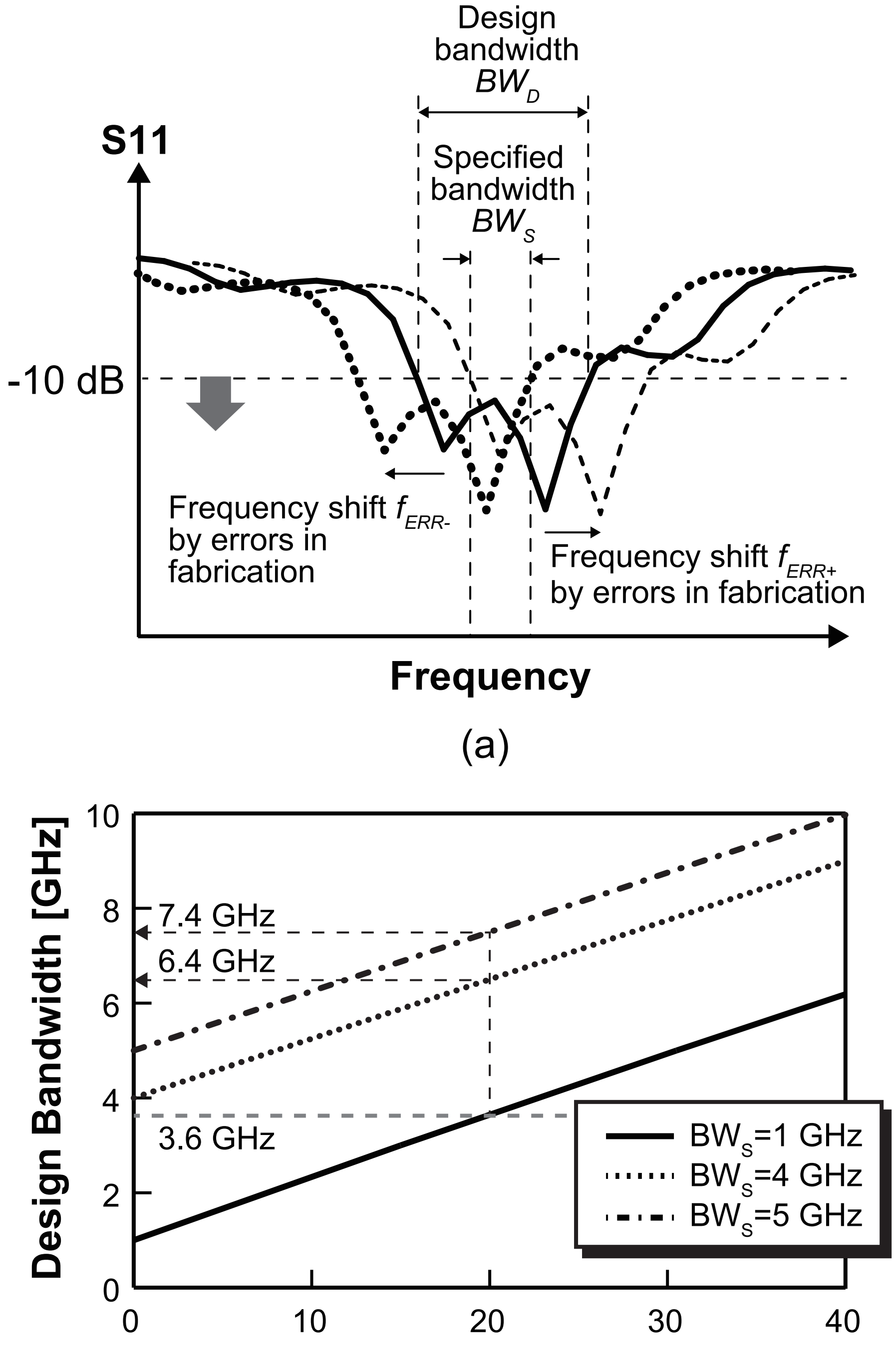

(a)

(b)

Fig. 6.1. (a) Determination process for design bandwidth and (b) dependence of required minimum design frequency on size error of metallic patterns for MSAs around 77-GHz band.

as a minimum is derived from the following equation:

$$BW_D \geq BW_S + f_{ERR-} + f_{ERR+} \tag{6.1}$$

The lens horn antenna has a small S11 of below -10 dB in the frequencies from 70 to 84 GHz as shown in Fig. 3.6 and the frequency shift of the S11 caused by a misalignment of the horn and MSA is small enough as shown in Fig. 3.11(a). In contrast, it is well known that the MSAs are sensitive to the error of their size due to etching errors in fabrication. Thus, a method to determine the design bandwidth focusing the frequency deviation caused by the etching errors for the MSAs is explained in this study.

A frequency shift of the MSA due to the error of its size is derived from the equation (3.5). Fig. 6.1(b) shows calculated results for a dependence of the design bandwidth on the size error of the MSA whose initial design frequency is 76.5 GHz. Solid, dotted, and dash-dotted lines indicate the results for the specified bandwidth of 1, 4, and 5 GHz, respectively. The design bandwidths are equal to the specified bandwidth if the size error is zero. According to the simulated result for a lens horn antenna described in Chapter 3, the antenna had the design bandwidth of 3.6 GHz as described in Section 3.4.1. Therefore, the size error of the MSA up to about 20 μm is acceptable in the design when the specified bandwidth of 1 GHz is applied. In other words, the design bandwidth is determined to 3.6 GHz when the maximum size error of about 20 μm is supposed. Accordingly, the design bandwidths become 6.4 and 7.4 GHz for the specified bandwidths of 4 and 5 GHz, respectively, as shown in Fig. 6.1(b). In the figure, the size errors where the pattern became thick were discussed. Since the results were almost the same when the pattern became thin, the results for were omitted in Fig. 6.1(b).

Generally, the bandwidth is discussed using a relative value normalized by the center frequency in order to compare the performance of technologies which use different frequency band. The design bandwidths shown in Fig. 6.1(b) correspond to 4.7%, 8.4%, and 9.7% for the specified bandwidths of 1, 4, and 5 GHz, respectively, when the supposed size error of MSAs is 20 μm.

To provide a wide bandwidth, technologies on MSAs have been reported, which had some slots in the MSAs or parasitic strips [6.1, 6.2] or patches for gap-coupling to the main patch radiators [6.3–6.5], where all structures could be realized using a mono-layer substrate. An MSA with two rectangular slots was proposed [6.2], which had a bandwidth of 2.26 GHz (27.48 to 29.74 GHz) by creating additional resonance frequencies near the initial frequency. The simulated result of the bandwidth was 1.46 GHz wider than the traditional MSAs; however, the slots required the width of 100 μm which corresponds to about 30 μm in the 77-GHz band. Therefore, the structure cannot be applied to the MSA using the 77-GHz band.

An MSA with multiple parasitic patches and shorting via was reported [6.5]. The antenna consisted of a main patch radiator with triangular shape which was surrounded by two parasitic patches with triangular shape and a parasitic patch with trapezoid shape. The fabricated antenna provided a matching bandwidth of 17.4% (from 5.5 to 6.55 GHz). However, the antenna structure required gaps between the main patch radiator and parasitic patches of 700 μm. The size of the gap corresponds to about 55 μm in the 77-GHz band, which is hard to be applied to mass production of automotive millimeter-wave radars at the time of writing.

The previous technologies require small gap between metallic patterns while providing a wide bandwidth, thereby, a new technology is required.

6.2.3 Other applications

FMCW millimeter-wave radars using the phase-shifted monopulse method as DOA estimation were focused in this study. However, MIMO radars will be a candidate for automotive radar in the next generation in order to provide higher safety capability to ADAS or AD systems. Bilik et al. reported a demonstration results for a MIMO radar in urban scenarios such as an environment with many highly-cluttered objects in a city street and other environment with many stationary objects in a rural street [6.6]. They presented the measured results on a high angular resolution of the fabricated MIMO radar as well as the advantage to use the MIMO radar to automotive applications.

Fig. 6.2 shows the principle of MIMO radars with respect to providing a virtual antenna array. Antennas of MIMO radars consist of N Tx antennas and M Rx antennas. Tx antennas transmit signals which are mutually orthogonal each other. Received signal by each Rx antenna are divided into signal elements which are originated by each Tx antenna by using a DBF algorithm. As a result, the MIMO radars perform as if they have $N \times M$ virtual array as Rx antennas. Thereby, the MIMO radars can provide higher angular resolution because of increasing the number of Rx antennas, since the angular resolution is derived from the following equation [6.7]:

$$\Delta\varphi = 1.22 \times \frac{\lambda_0}{NMd_R}, \tag{6.2}$$

where $\Delta\varphi$ and d_R are the angular resolution and separation distance of Rx array antenna.

The number of targets which can be identified as an individual object also increases as increasing the number of the Rx antennas. The maximum number K_{max} of identified targets in the MIMO radars is described in the following equation [6.8]:

$$K_{max} = \frac{NM-1}{2} \tag{6.3}$$

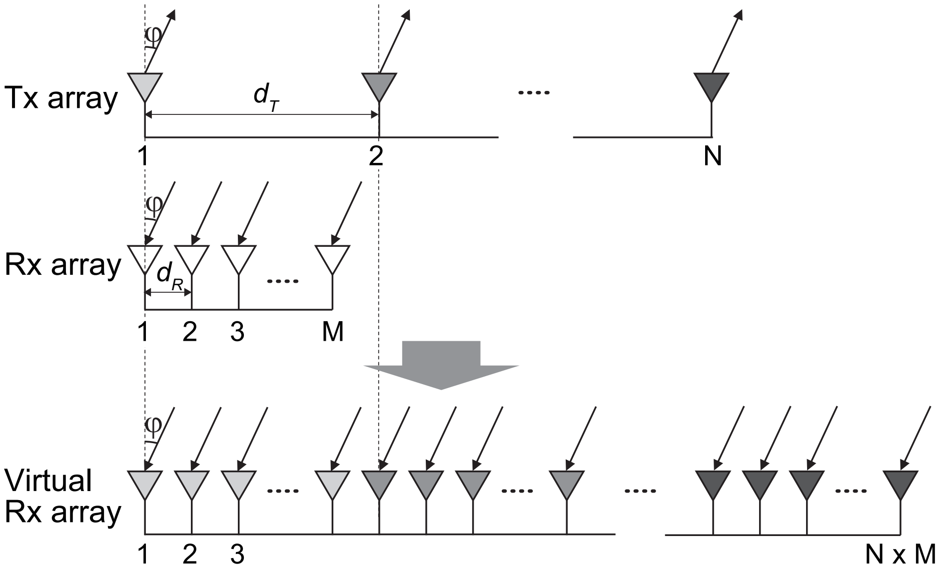

Fig. 6.2. Principle of MIMO to provide virtual Rx array.

Because of the improvement of angular resolution and the number of identified targets, the MIMO radar are expected to detect objects separately in order to improve safety function of ADAS or AD systems. It is also possible to apply the MIMO radar for localization of the ego vehicle or a free space detection to recognize the drivable area, which is commonly done by using LiDARs or cameras at the time of writing.

To provide such high performances of MIMO radars, the received signals inputted into each Rx channel of receivers should be uncorrelated each other, meaning a high isolation between Rx channels is required, in order to improve accuracy of dividing the received signals in each Rx channel. According to the measured results shown in Fig. 4.14, the proposed lens horn antennas had a high antenna isolation of greater than 31 dB even if there is no gap between adjacent antennas. Thereby, the antenna had an advantage to be applied to MIMO radars.

However, the separation distance of Rx antennas (d_R) is usually designed half wavelength to avoid grating lobes in the detection angle of ±90 degrees in azimuth or elevation. The maximum angular detection φ_{max} is derived from the following equation [1.31]:

$$\varphi_{max} = \pm \sin^{-1}\left(\frac{\lambda_0}{2d_R}\right) \tag{6.4}$$

The half wave-length is about 1.5 mm in the 77-GHz band. Since the proposed lens horn antennas required a separation distance between the center of the output-aperture of several mm, the maximum angular detection become narrow. Therefore, a new technology to suppress the grating lobes is required to apply the proposed lens horn antennas to the MIMO radars.

This study focused on the millimeter-wave radars for automotive applications; however, the MIMO technology is also applied in wireless communication systems. Technologies on a massive MIMO for 5G wireless communication systems have been presented [6.9, 6.10] to realize a multi-user MIMO system in order to mainly improve spectral efficiency and energy efficiency. The structure and requirements of antennas for the massive MIMO are similar to that for the MIMO radars. Thereby, the massive MIMO for the wireless communication systems is a candidate to apply the proposed lens horn antenna, taking advantage of the high antenna isolation and high antenna gain.

A velocity sensor for train operation systems is another candidate for an application of the proposed lens horn antennas. The train operation systems require a high accurate location of train to improve operational safety. A method to estimate train location by using the number of wheel rotation is a way; however, there are problems to obtain a highly accurate position: slip or slide of wheels, undetectable velocity of sensors (wheel rotation sensors cannot detect the rotation at very low velocity), and the diameter changing of wheel due to long-distance operation. To solve these problems to detect an accurate velocity of trains, a millimeter-wave velocity sensor has been investigated. Fukuda et al. reported a trial of the train location system using a millimeter-wave velocity sensor [6.11] whose size was 300 × 210 × 150 mm and weight was 40 kg. Since the proposed lens horn antenna provides small size and high antenna gain, it will contribute to reduce the size of the velocity sensor for the train operation systems.

References

[6.1] J.-Y Sze and K.-L Wong, “Slotted Rectangular Microstrip Antenna for Bandwidth Enhancement,” *IEEE Trans. Antennas Propag.*, vol. 48, no. 8, pp. 1149–1152, Aug. 2000.

[6.2] Z. Li, R. Jian, Y Chen, and T. Chen, “A Novel Design for Millimeter Wave Microstrip Antenna with Bandwidth Enhancement,” in *Proc. of 2018 IEEE Student Conference on Research and Development*, pp. 1–4, Nov. 2018.

[6.3] J. Ghosh and J. S. Roy, “Design of A Wideband Microstrip Antenna,” *J. of Electomagn. Waves and Appl.*, vol. 22, pp. 2379–2389, Jan. 2008.

[6.4] A. Kandwal and S. K. Khah, “A novel design of gap-coupled sectoral patch antenna,” *IEEE Antennas Wireless Propag. Lett.*, vol. 12, pp. 674–677, Dec. 2013.

[6.5] K.-D. X, H. Xu, Y Liu, J. Li, and Q.-H. Liu, “Microstrip Patch Antennas With Multiple Parasitic Patches and Shorting Vias for Bandwidth Enhancement,” *IEEE Access*, vol. 6, pp. 11624–11633, Mar. 2018.

[6.6] I. Bilik, O. Bialer, S. Villeval, H. Sharifi, K. Kona, M. Pan, D. Persechini, M. Musni, and K. Geary, “Automotive MIMO Radar for Urban Environments,” *IEEE Radar Conf.*, pp. 1–6, May 2016.

[6.7] C. Vasanelli, R. Batra, A. D. Serio, F. Boegelsack, and C. Waldschmidt, “Assessment of a Millimeter-Wave Antenna System for MIMO Radar Applications,” *IEEE Antennas and Wireless Propag. Lett.*, vol. 16, pp. 1261–1264, Nov. 2017.

[6.8] J. Li and P. Stoica, “MIMO Radar with Colocated Antennas,” *IEEE Signal Processing Magazine*, vol. 24, issu. 5, pp. 106–114, Sep. 2007.

[6.9] E. G. Larsson, O. Edfors, F. Tufvesson, and T. L. Marzetta, “Massive MIMO for Next Generation Wireless Systems,” *IEEE Communications Magazine*, vol. 52, issu. 2, pp. 186–195, Feb. 2014.

[6.10] E. G. Larsson and L. V. d. Perre, “Massive MIMO for 5G,” *IEEE 5G Tech. Focus*, vol. 1, no. 1, pp. 1–4, Mar. 2017.

[6.11] M. Fukuda, H. Sugahara, A. Gion, Y. Ono, T. Kitano, and T. Shirai, “Development of Train Location Detection Methods for Signalling,” *QR of RTRI*, vol. 55, no. 2, pp. 98–105, May 2014.

Acknowledgements

The author would like to thank Prof. Jiro Hirokawa, Department of Electrical and Electronic Engineering, Tokyo Institute of Technology, for his guidance in the doctoral program and for significant discussion and coaching with respect to writing this doctoral dissertation as well as journal papers previously reported. I would also like to thank Prof. Kei Sakaguchi, Assoc. Prof. Atsuhiro Nishikata, Assoc. Prof. Takahiro Aoyagi, and Assoc. Prof. Gia Khanh Tran, Department of Electrical and Electronic Engineering, Tokyo Institute of Technology, for their invaluable suggestions to the contents of this doctoral dissertation.

The author would like to thank Mr. Hideyuki Nagaishi, Hitachi, Ltd., Research & Development Group, for significant discussion and supports regarding design and measurement of the proposed antennas to proceed this study. I would also like to thank Dr. Hiroshi Shinoda and Mr. Hisanori Matsumoto, Hitachi, Ltd., Research & Development Group, for their invaluable input on antenna design. I would also like to thank Mr. Akira Kitayama, Hitachi, Ltd., Research & Development Group, for discussion on required specifications for radars and antennas. I would also like to thank Dr. Masaru Kokubo, Hitachi, Ltd., Research & Development Group, for significant advice for writing journal papers previously reported.

The proposed antennas in this study have been investigated under a production development scheme on automotive millimeter-wave radars with Hitachi Automotive Systems, Ltd. The author would like to thank Dr. Hiroshi Kuroda and Mr. Kazuaki Takano, Hitachi Automotive Systems, Ltd., for discussion on operation principle and requirements for radars such as techniques on DOA estimation. I would also like to thank Mr. Satoshi Sasaki, Hitachi Automotive Systems, Ltd., for discussion on required specifications for radars. I would also like to thank Mr. Toshihiro Hiraishi, Hitachi Automotive Systems, Ltd., for his support in fabricating the antennas. I would also like to thank Dr. Makoto Kudo and Dr. Shoji Muramatsu, Hitachi Automotive Systems, Ltd., for providing insights on the requirements and technology trends related to ADAS and AD systems.

The author would like to thank Dr. Hideaki Kurata, Hitachi, Ltd., Research & Development Group, for giving motivation and support to enter the doctoral program in the Department of Electrical and Electronic Engineering, Tokyo Institute of Technology. I would also like to thank Dr. Toshiharu Nogi, Mr. Tatsuhiko Monji, Mr. Takeshi Mitamura, Mr. Yoshito Amino, and Mr. Hideyasu Kudo, Hitachi Automotive Systems, Ltd., for providing environment to attend to the doctoral program while working. I would also like to thank Dr. Riichiro Takemura and Dr. Masanao Yamaoka, Hitachi, Ltd., Research & Development Group, for providing environment to attend to the doctoral program while working. I would also like to thank other all members who I worked with in Hitachi, Ltd., Research & Development Group and Hitachi Automotive Systems, Ltd., for their kind support and encouragement to take the doctor's degree.

Finally, the author would like to thank my family for kind support and encouragement to take the doctor's degree.

Publication List

Publications and presentations on this work

Journal papers (lead author)

[1] **A. Kuriyama**, H. Nagaishi, and H. Kuroda, “Horn and Lens Antenna with a Small Antenna Substrate and High Production Tolerance for 77-GHz Automotive Long-Range Radar,” *IEEJ Trans. Electrical and Electronic Engineering*, vol. 14, issu. 8, pp. 1244–1253, Aug. 2019.

[2] **A. Kuriyama**, H. Nagaishi, H. Kuroda, and A. Kitayama, “Horn and Lens Antenna with Low Height and Low Antenna Coupling for Compact Automotive 77-GHz Long-Range Radar,” *IEICE Trans. Electron.* vol. E103-C, no. 10, pp. 1–8, Oct. 2020.

[3] **A. Kuriyama**, H. Nagaishi, H. Kuroda, and A. Kitayama, “Horn and Lens Antenna Array with Chevron-Shaped Prism for 77-GHz Automotive Radar with Dual-Range Sensing and a Dual Field of View,” *IEEJ Trans. Electrical and Electronic Engineering*, vol. 15, issu. 3, pp. 451–459, Mar. 2020.

International conferences (lead author)

[1] **A. Kuriyama**, H. Nagaishi, H. Kuroda, and K. Takano, “A High Efficiency Antenna with Horn and Lens for 77 GHz Automotive Long Range Radar,” in *Proc. of the 13th European Radar Conf.*, pp. 378–381, Oct. 2016.

[2] **A. Kuriyama**, H. Nagaishi, H. Kuroda, A. Kitayama, and S. Sasaki, “High Efficiency and Small Antenna Technology for A Long Range Radar Using 77 GHz Band,” *IWPC The International Wireless Industry Consortium, Automotive Radar Workshop*, Feb. 2017.

[3] **A. Kuriyama**, H. Nagaishi, H. Kuroda, A. Kitayama, and S. Sasaki, “High Efficiency and Small Antenna for 77 GHz Long Range Radar,” in *Proc. of the Thailand-Japan MicroWave*, FR2-02, Jun. 2017. (non-published)

[4] **A. Kuriyama**, H. Nagaishi, H. Kuroda, A. Kitayama, and S. Sasaki, “High Efficiency and Small Antenna with Horn and Lens for 77 GHz Automotive Radar,” in *Proc. of the 18th Int. Symp. on Antenna Tech. and Applied Electromagnetics*, pp. 1–2, Aug. 2018.

International conferences (co-author)

[1] H. Nagaishi, **A. Kuriyama**, H. Kuroda, and A. Kitayama, “Horn and Prism Antenna for Dual Range and Dual FOV Automotive Radar using 77-GHz Band,” in *Proc. of the 18th Int. Symp. on Antenna Tech. and Applied Electromagnetics*, pp. 1–2, Aug. 2018.

[2] H. Nagaishi, **A. Kuriyama**, A. Kitayama, and H. Kuroda, “Horn and Prism Antenna for Dual Range and FOV 77-GHz Radar on Automotive Application,” *the 12th Global Symp. on Millimeter-Waves*, May 2019. (non-published)

Domestic conferences (lead author)

[1] **A. Kuriyama**, H. Nagaishi, H. Kuroda, and K. Takano, “A High Efficiency Antenna for 77 GHz Long Range Radar,” in *Proc. of the IEICE General Conf.*, B-1-125, Mar. 2016. (in Japanese)

Publications and presentations on other works

Journal papers (lead author)

[1] **A. Kuriyama**, S. Takaoka, K. Oto, K. Murase, S. Shimomura, S. Hiyamizu, M. Chkr, T. Jungwirth, and L. Smrčka, “Cyclotron resonance in double-layer two-dimensional electron system in tilted magnetic fields,” *Solid State Communications*, vol. 111, issu. 12, pp. 699–704, 1999.

[2] **A. Kuriyama**, S. Yuyama, M. Ohnishi, H. Matsumoto, T. Tanoue, I. Ohbu, and F. Morisawa, “Thermal Gain Variation Compensation Technique Using Thermistor on HPA Module for W-CDMA System,” *IEICE Trans. Electronics*, vol. E91.C, no. 12, pp. 1933–1940, 2008.

Journal papers (co-author)

[1] S. Takaoka, **A. Kuriyama**, K. Oto, K. Murase, S. Shimomura, S. Hiyamizu, M. Chkr, T. Jungwirth, and L. Smrčka, “Far-infrared magneto-absorption of double-layer two-dimensional electron system in tilted magnetic fields,” *Physica E Low-dimensional Systems & Nanostructures*, vol. 6, issu. 1–4, pp. 623–626, Feb. 2000.

[2] N. Nishiyama, Y. Soga, K. Nagaoka, T. Okada, J. T. Contreras, A. Wallash, and **A. Kuriyama**, “Analysis of Electrical Resonance of a Hard Disk Drives Suspension Interconnect and Invasion Into Read Signal Path,” *IEEE Trans. Magnetics*, vol. 50, no. 11, pp. 1–4, Nov. 2014.

International conferences (lead author)

[1] **A. Kuriyama**, S. Yuyama, M. Ohnishi, H. Matsumoto, T. Tanoue, and I. Ohbu, “Reduced gain variation against temperature with thermistor on HPA module for W-CDMA system,” in *Proc. of the Asia-Pacific Microw. Conf.*, Dec. 2006.

International conferences (co-author)

[1] S. Takaoka, **A. Kuriyama**, K. Oto, K. Murase, M. Chkr, T. Jungwirth, and L. Smrčka, “Influence of parallel magnetic field on cyclotron mass in double-layer two-dimensional electron system,” in *Proc. of the New Phenomena in Mesoscopic Structures*, Dec. 1998 (*Microelectronic Engineering*, vol. 47, issu. 1–4, pp. 293–295, Jun. 1999).

[2] N. Nishiyama, Y. Soga, K. Nagaoka, T. Okada, J. T. Contreras, A. Wallash, and **A. Kuriyama**, “Analysis of Electrical Resonance of a Hard Disk Drive’s suspension interconnect and Invasion into Read Signal Path,” *IEEE Int. Magnetics Conf. Dig.*, May 2014.

Domestic conferences (lead author)

[1] **A. Kuriyama**, S. Takaoka, K. Oto, K. Murase, S. Shimomura, S. Hiyamizu, and L. Smrčka, “A Dependence of Cyclotron Mass on Parallel Magnetic Fields in Double-Layer Two-Dimensional Electron System,” in *Proc. of the Autumn Meeting of the Physical Society of Japan*, 26a-YG-5, Sep. 1998. (in Japanese)

[2] **A. Kuriyama**, S. Takaoka, K. Oto, K. Murase, and L. Smrčka, “Cyclotron Effective Mass in Double-Layer Two-Dimensional Electron System in Tilted

Magnetic Fields,” in *Proc. of the Annual Meeting of the Physical Society of Japan*, 30p-ZE-8, Mar. 1999. (in Japanese)

[3] **A. Kuriyama**, T. Tanoue, O. Kagaya, K. Otsuka, Y. Shimada, and K. Yamamoto, “A Dependence of Thermal Resistance on Heatsink Structure in Resin Substrate for RF Modules,” in *Proc. of the IEICE General Conf.*, C-2-78, Mar. 2002. (in Japanese)

[4] **A. Kuriyama** and T. Tanoue, “Reduction of Matching Network Loss in Power Amplifier Modules by using Resin Substrate,” in *Proc. of the IEICE Society Conf. Dig.*, C-2-21, Sep. 2002. (in Japanese)

[5] **A. Kuriyama**, S. Yuyama, M. Ohnishi, H. Matsumoto, T. Tanoue, and I. Ohbu, “Reduced Gain Variation against Temperature with NTC Thermistor on HPA Module for W-CDMA System,” in *Proc. of the IEICE Microw. Conf.*, Jan. 2007. (in Japanese)

[6] **A. Kuriyama**, S. Yuyama, M. Ohnishi, H. Matsumoto, T. Tanoue, and I. Ohbu, “Improvement of Thermal Gain Variation of HPA Module for W-CDMA Using Thermistor,” in *Proc. of the IEICE General Conf.*, C-2-30, Mar. 2007. (in Japanese)

Domestic conferences (co-author)

[1] A, Kitayama, H. Nagaishi, **A. Kuriyama**, H. Kuroda, and S. Sasaki, “Vehicle Ditection with 77 GHz Radar Using Horn and Lens Antenna,” in *Proc. of the IEICE Society Conf.*, C-2-82, Sep. 2019. (in Japanese)

[2] A, Kitayama, H. Nagaishi, **A. Kuriyama**, and H. Kuroda, “Improvement of Angular Estimation Accuracy with 77 GHz Radar Using Horn and Lens Antenna,” in *Proc. of the IEICE General Conf.*, C-2-60, Mar. 2020. (in Japanese)